DESIGN AND FABRICATION OF A NEXT GENERATION REGENERATIVE NEURAL INTERFACE

by

JAMES CHURM

A thesis submitted to
The University of Birmingham
for the degree of
DOCTOR OF PHILOSOPHY

School of Engineering
College of Engineering and Physical Sciences
The University of Birmingham
September 2017

Abstract

Neural interfaces are used to enable the bi-directional communication between electronic and neural signals. A Spiral Peripheral Neural Interface (SPNI) is an electrode array that has been previously presented as a regenerative neural interface capable of receiving information from, and transmitting information to nerves. The SPNI has previously been proven in concept but two key issues preventing further development were observed: electrical isolation between channels of the device and biocompatibility. When stimulating nerves in the device, the electrodes are insufficiently isolated from one another and stimulations in one channel can trigger neural activity in other parts of the SPNI. Along with this, neural interfaces as a generality, suffer from chronic viability problems, due to the biological rejection of the foreign body response. These issues were addressed in this thesis by the addition of a PDMS silicone membrane into the structure of the SPNI.

Incorporating a membrane into the device raised certain issues regarding the internal mechanical structure of the SPNI, in this thesis these issues were addressed. In neural interface technology, it is usual to design conductors in the neutral plane of the devices, however this thesis presents evidence that this is unnecessary when the conductor is thin and laminated. The lamination of a conductor with polymers prevents stress concentration from causing the conductor to break and thus increases its practical ultimate tensile strength to levels that can be utilised in asymmetrical microfabrication design.

The electrical performance of devices with PDMS sheets included was investigated. It has been shown that the PDMS dramatically increases the intra-electrode impedance as well as reducing the signal measured on adjacent electrodes when a particular channel is stimulated.

The biocompatibility of the SPNI may also be improved by the addition of the PDMS membrane as it has been shown that scar reducing drugs can be released from this layer.

Drug release systems have previously been shown to dramatically increase the chronic viability of implants.

This thesis addresses the main issues previously presented in the SPNI and brings the device up to a new standard which can once again be tested for its viability *in vivo*.

ACKNOWLEDGMENTS

I would like to express my gratitude to my supervisor, Dr Edward Tarte, for facilitating my study into a diverse and interesting field and for the advice and support given over the course of the Ph.D. I would also like to thank Dr Richard Barrett for his mentorship along with practical support and guidance that has guided me through the realms of scientific endeavor. Dr Tarte and Dr Barrett, through our many conversations this thesis was made possible, thank you for all of the training, I hope I will put it to good use.

I would also like to thank my fellow Ph.D. students James Crowcombe and Serena Quan for their discussions, the Department of Electrical, Electronic and Systems Engineering for it's financial support, Mary Winkles for her pursuit of scholarships for my benefit and Donna Johnson for her excellent technical support, advice and assistance.

Finally I would like to thank my friends and family who have endured my absence, distance and grumpiness. I would like to thank them for their continued support and value every conversation, this Ph.D. would not have been possible without you.

CONTENTS

LIST OF FIGURES

LIST OF TABLES

Abbreviations

AP Action Potential

ATP Adenosine Tri-Phosphate

BCI Brain Computer Interface

Benedicts solution A solution of calcium carbinate, sodium chloride and potasium chloride used to simulate physiological fluids.

CAD Computer Aided Design

CNS Central Nervous System

DUT Device Under Test

ECG Electrocardiography

ECoG Electrocorticography

EIS Electrochemical Impedance Spectroscopy

ELISA Enzyme-Linked Immunosorbent Assay

EMG Electromyography

FFT Fast Fourier Transform

FINE Flat Interface Nerve Electrode

IHP Inner HelmHoltz Plane

in vivo Taking place in a living organism

IPA Isopropyl Alcohol

IV Current-Voltage

MIBK Methyl Isobutylketone

NGF Neural Growth Factor

OHP Outer Helmholtz Plane

PBS Phosphate Buffered Solution

PCB Printed Circuit Board

PDMS Polydimethylsiloxane

PMMA Poly(methyl methacrylate)

PNS Peripheral Nervous System

PSPI and PI Photosensitive Polyimide

PVD Physical Vapour Deposition

RC Resistor-Capacitor

RO Reverse Osmosis

RTV Room-Temperature-Vulcanization

SEM Scanning Electron Microscopy

SIL Single In Line

SNR Signal to Noise Ratio

SPNI Spiral Peripheral Neural Interface

TMR Targeted Muscle Reinnervation

UV Ultra Violet

UVO Ultra Violet O-zone

Physical Constants

R The universal gas constant, $8.31\mathrm{JK}^{-1}\mathrm{mol}^{-1}$

F Faraday constant, 96,500 Cmol^{-1}

V_t Thermal voltage, 25mV at room temperature

ϵ_0 Permittivity of free space, 8.55×10^{-12} F/m

CHAPTER 1

NEUROPROSTHETICS

This introductory chapter will explain the motivations behind the research into neural interfaces as an enabling technology for state-of-the-art powered prosthetic devices. It will then go on to discuss various types of neural interface that are currently the subject of much research. Finally it will introduce the electrode array that is the subject of this thesis, along with the contributions and overview of the thesis.

1.1 Motivations

There are an estimated ten million amputees worldwide [1], 2 million currently living in the United States costing around \$8.3 billion per year in associated costs [2], with limb loss either resulting from diabetes, car accidents, industrial accidents, congenital disorders or war. In order to improve the quality of life for amputees, several prosthetic solutions have been developed over the last century. The classic treatment for an amputee is a passive or body powered prosthetic limb, seen in figure 1.1. These solutions offer the patient a basic level of functionality in place of the lost limb, allowing them to walk or hold things in place. Despite improved life quality, amputees still struggle to complete everyday tasks.

Powered prosthetics have been in development for nearly one hundred years [3]. Since the advent of electrically controlled prostheses there has been the promise of offering

Figure 1.1: Taken from the Ottobock website [5], shows a body powered prosthetic.

amputees a much greater degree of functional restoration than previous body-powered alternatives. However, even with very sophisticated prostheses such as the Touch Bionics' iLimb [4] or the Otto-Bock Michelangelo [5] (seen in figure 1.2) the amputee acceptance rate is around thirty percent [6], leaving the remaining seventy percent either rejecting the technology or opting not to use its advanced functionality.

The rejection of this technology is due to a number of important factors, most of which are a result not of the functionality of the bionic arm, but of the interface between man

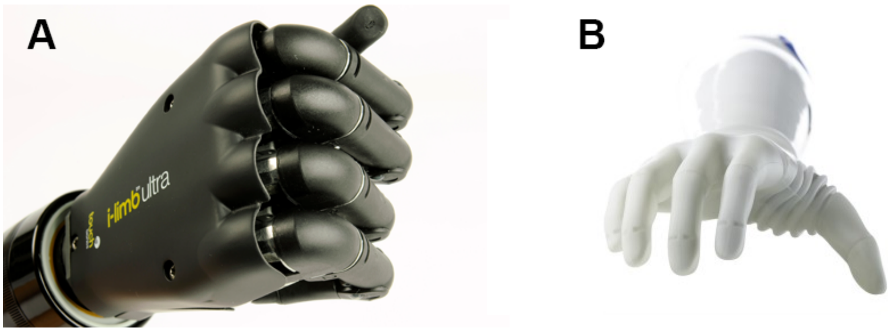

Figure 1.2: Taken from Touch Bionics, the iLimb (left) [4] and Ottobock, the Michaelangelo (right) [5] websites, showing some of the state of the art powered prosthetic hands.

and machine. The bionic arms mentioned above coupled with advanced cybernetic technologies mean that state-of-the-art bionic limbs, arms in particular are close to rivaling the functionality of the human hand in terms of strength, dexterity and maneuverability [7]. The interface between the human body and the arm however is based around fifty year old technology which has yet to be refined to an acceptable clinical level.

The standard interface for the control of advanced prostheses is a set of myoelectric sensors. These are small metal electrodes that are glued to the body with conductive adhesive which can pick up the electrical excitation of muscles below the surface of the skin to which they are attached. This signal can then be amplified, digitised and send to the software which can interpret the signals.

These electrodes record EMG (or Electromyography) where muscle movement causes the signals. Other surface recording techniques include ECG (or Electrocardiography) and EEG (or Electroencephalography) which record signals produced by the heart or brain respectively. All of these techniques involve the use of basic electrodes being placed in appropriate places on the surface of the skin, figure 1.3.

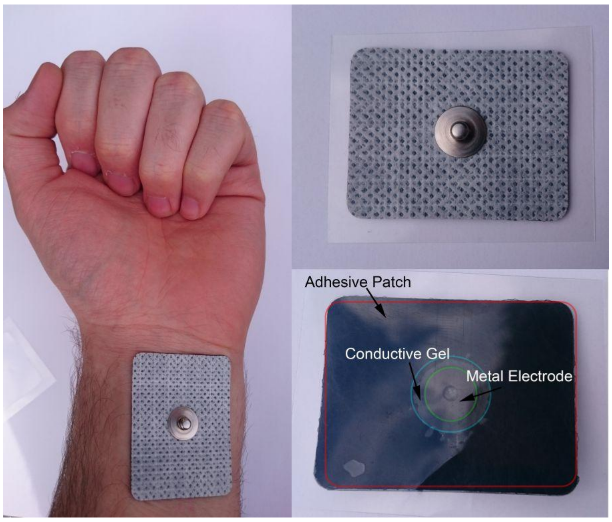

Figure 1.3: An example of the kind of electrodes used in EMG and ECG systems.

There are however several fundamental problems with the use of myoelectric sensors. The first and most prominent of which is that they rely on the contraction of functional muscle to control the prostheses. By their nature, amputees have lost the muscles that controlled the original movement of the lost limb. Therefore other muscles, which are not usually used for the coded movement, need to be recruited. For example an upper limb amputee may have sensors to control a prosthetic arm mounted on their pectoral muscles, when the patient consciously contracts their pectoral muscles, the prosthetic system reads this as an input and processes accordingly.

This recruitment of muscles non-native to the limb they are coding for presents certain problems. The pectoral muscles only has a few conscious movements when in comparison to an entire arm system, due to this the range of achievable movement in the prosthetic arm is significantly reduced when compared to a native arm. Typically the user has to cycle through different settings that control desired movements, such as different configurations of clasps and grips, and then uses another muscle to control whether the hand should be opening or closing on the chosen movement. This is a mentally laborious, time consuming and an unnatural process which requires a lot of cognitive effort. This laborious interface is in stark contrast to the natural ease one would command a natural hand to do the same action. The lack of natural usability is the main reason suggested as to why the rejection of the technology is so high [6].

Myoelectric sensors also have to be applied and reapplied daily. To prevent adverse bodily reactions to long term contact with the electrodes (such as inflammation around the interface site), they also have to be slightly repositioned. This can affect the computer's ability to predict the users intent and can lead to either persistent retraining of the system or irritation of the user. Even with the best cybernetics, myoelectric sensors perform well only in specific conditions [8], if the user stretches for a book, or sweats too much, or twists unexpectedly, the computer may no longer read the muscle actions as the signals could change enough to push them outside predictable bounds.

The final problem with modern powered prostheses is that they produce no haptic feedback. If not looking at the artificial arm the user has no spacial awareness with regard to the limb. They also do not know how hard they are squeezing an item or if some obstacle is preventing the desired movement taking place.

There have been tremendous leaps forward in recent years getting over some of these issues using techniques such as Targeted Muscle Reinnervation (TMR). TMR is a surgical technique where the surviving nerves that serviced the missing limb are located and redirected to functional muscle elsewhere so that myoelectric techniques can be rendered more effective. In an amputated arm, the nerves that controlled the arm will still be present and are usually fully functional above the amputation point. These nerves can be surgically rerouted to muscles in the chest which will then contract in response to thought patterns originally mapped to the missing hand, outlined in figure 1.4. This process causes the muscles to respond in strong, but unnatural ways. With myoelectric electrodes on the surface of the chest muscle it is possible for the prosthetic's computer to interpret many movements without ambiguity, as individually remapped nerves are causing specific muscle flexions.

TMR dramatically improves the functionality of myoelectric interfaces, but still has issues. Many electrodes are required to detect the multiple muscle movements, this number is prohibitive as the patient would need to regularly remove and replace the electrodes in very similar positions to enable the computer to retain it's signal map. Another issue with TMR is signal leakage because of the large muscles recruited [9], it is possible for a signal from a larger muscle to be read and interpreted as a signal from smaller muscles, leading to intention interpretation difficulties. Finally, although sensation restoration has been demonstrated in TMR patients the closed-loop of haptic feedback has not yet been proposed [10].

Closing the loop has been an active research field for many years and is desperately needed if a functional solution to the prosthetic problem is to be adequately addressed. Solutions to the feedback problems have been proposed in the form of neural interfaces, a different way of harvesting user intent by acquiring signals directly from the nerves, instead of muscles.

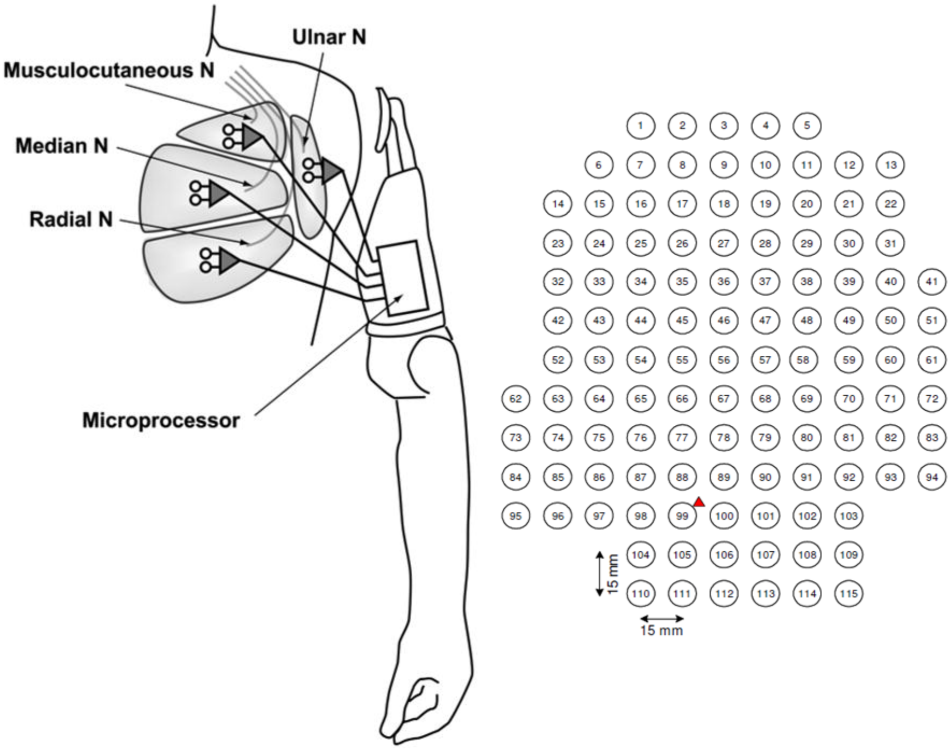

Figure 1.4: a) a schematic of how TMR takes viable nerve stumps and reroutes them to functional muscle elsewhere in the chest, b) an example of a TMR electrode array containing 115 electrodes, it may be possible to bring this down to around 22 electrodes, but this is still cumbersome for long term use.

1.2 The Neural Interface

With myoelectric electrodes the muscle acts as a biological amplifier. When the signal from the nerve reaches the muscle, it contracts. This contraction releases a large electrical signal that is strong enough to be detected across the skin. Individual nerves however do not usually emit a strong enough signal to be detectable across the skin (with the exception of the skull and EEG signals).

Gathering signals from nerves rather than muscles is highly desirable due to the fact that individual nerves code more one to one with an intended movement, so if the nerves signals can be accessed, there will be no ambiguity to what action was desired. Along with this electrical access to the nerves would make it possible to stimulate them, sending information back to the brain, which opens up the possibility of creating natural feeling sensation from an artificial limb. Gaining the essential haptic feedback. This one-to-one

Table 1.1: A selection of different kinds of electrode proposed over the last 30 years and their relative selectivities, invasiveness and complexities.

Implant type	Selectivity	Invasiveness	Complexity	References
Myoelectric	Very Low	Very Low	Very Low	[12–14]
Book and Cuff Electrodes	Moderate	Moderate	Moderate	[15–18]
Interfascular	Moderate	Moderate	Low	[19, 20]
Penetrating	High	High	Moderate	[21, 22]
Sieve and Regenerative	Very High	Very High	Moderate to high	[23–27]

link between intent and action along with the promise of sensation restoration makes the neural interface the desired technology. Details of neural actions and stimulations will be provided in the next chapter.

Neural interfaces are small devices that interact directly with the nerve and are generally categorised into several different types, each with its own selectivity vs invasivity, figure 1.5 and table 1.1 show how the different electrode types differ .

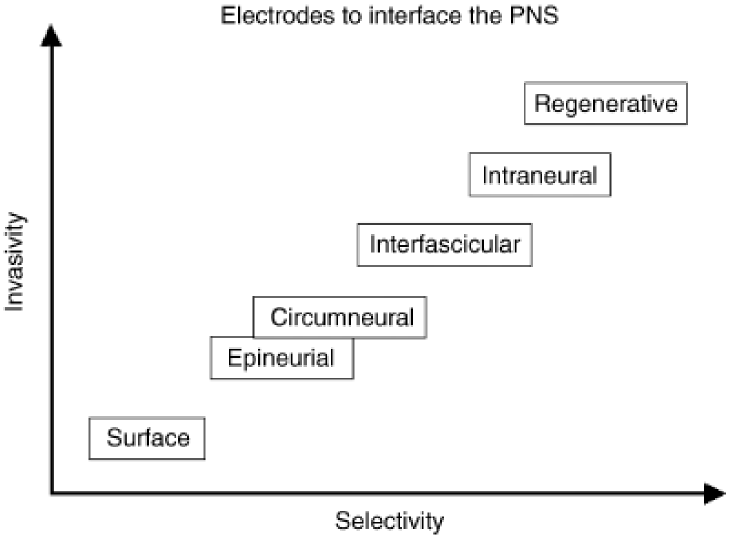

Figure 1.5: Taken from [11] showing the different kinds of neural interface and how they sit on the selectivity vs invasiveness chart.

Extraneural electrodes (including Epineural and Circumneural) are implanted devices which wrap around a bundle of neurons or a nerve and are sutured to the epineurium (more detailed anatomy of the nerve will be seen in the next chapter). These include book electrodes (figure 1.6A and B) which close around a nerve bundle and cuff electrodes (figure 1.6C) which are implanted to surround a section of nerve (a refinement of which is the FINE electrode [15]). These devices ideally do not disturb the nerves, only the surrounding tissue and hence are the next least invasive next to muscle based technologies. With the increased invasiveness comes a massive increase in the ability to tell whether a nerve bundle under inspection has activity or not. The downside being that it is difficult to identify which specific nerves within a bundle are firing which leads to ambiguous decoding of these signals.

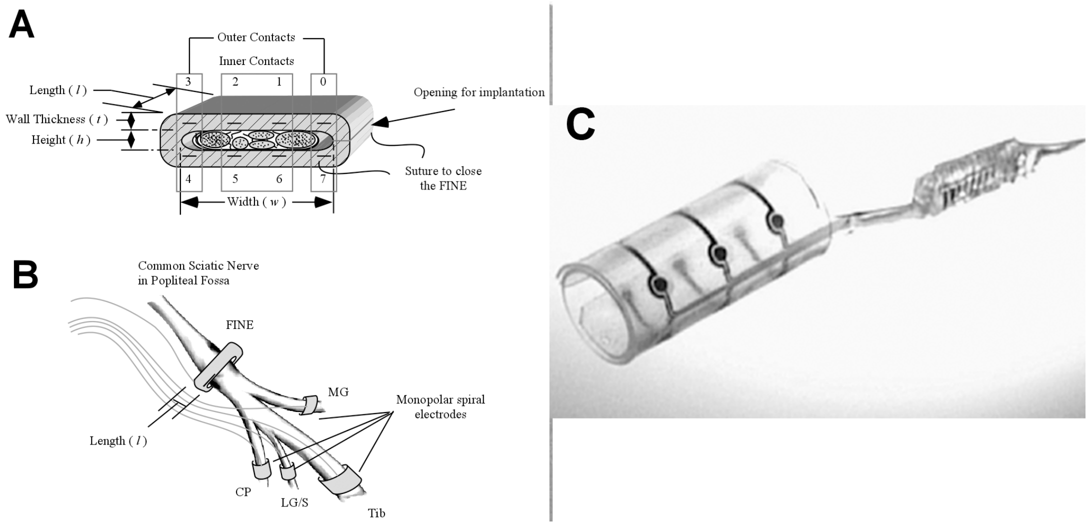

Figure 1.6: a) showing a book electrode that closes around a nerve and b) how they are applied to neural branches taken from [15], c) a cuff electrode which is fitted around a nerve to take signals from its surface, taken from [28].

Interfascicular electrodes get even closer to individual axons by actually inserting electrical contacts into the nerve but without penetrating the nerve fascicles giving even greater sensitivity, figure 1.7. This is followed by an even more invasive approach of penetrating intraneural electrodes. These electrodes are inserted directly into a peripheral nerve to gain even greater clarity of signal. These two devices however share issues, in that to get adequate resolution too many inserted devices are required to get a clear picture of overall neural activity within the bundle.

Finally, there are regenerative electrodes which are by far the most invasive but also enable the greatest selectivity. Regenerative devices require the entire nerve to be severed,

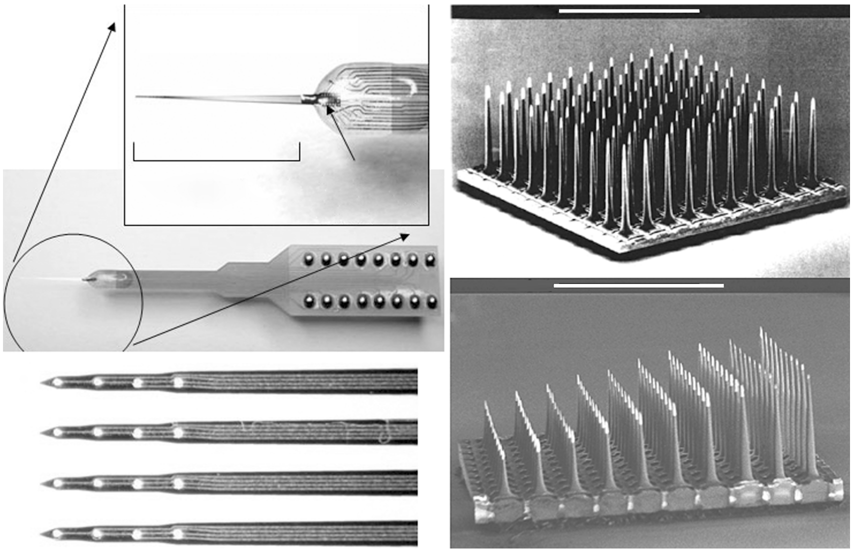

Figure 1.7: A range of penetrating electrodes taken from [11] that have been developed at Mitchegen. These devices penetrate the nerve and have electrodes at their tips.

figure 1.8. The severed stump is then sutured to the opening of the device, and due to neuro-regenerative properties, the individual nerves begin to regenerate and hence grow into and populate the device. As the nerves have grown into the device the individual axons can be encouraged to grow very close to electrode sites, enabling individual axons or axon groups to be easily discerned from each other when firing.

The Spiral Peripheral Nerve Interface (SPNI) is a regenerative electrode array that is the main study of this thesis.

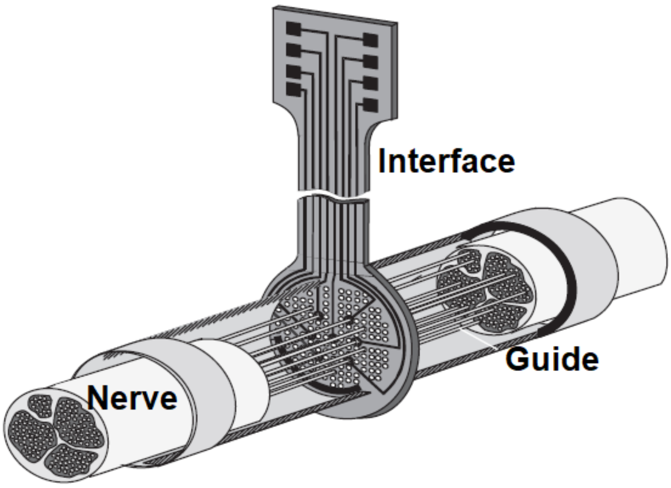

Figure 1.8: A regenerative sieve electrode, often etched from silicon, these devices are mated to a nerve so that individual axons grow through the electrode rings. Taken from [11]

1.3 The SPNI

The Spiral Peripheral Nerve Interface (SPNI) is a novel regenerative neural interface that overcomes some fundamental issues present in other types of device. The theory of which will be covered further in the next chapter.

To enable batch production, the SPNI is microfabricated as a flat sheet and is wound into a spiral structure. This spiral provides three dimensional channels which enclose the regenerating axons, both guiding them toward small electrodes embedded in the floor of the channel and increasing the extra-cellular resistance around the axon, improving the signal-to-noise ratio.

The SPNI has been shown to record and stimulate nerves *in vivo* providing a potential platform as a neural interface that can both record user intent directly, providing a more natural user interface and which could provide sensation from a prosthesis to the brain. Providing a bi-directional communication link between electronic systems and nervous systems.

1.4 Technical Issues with the SPNI

The SPNI, although tested successfully *in vivo* [25], has been shown to have some technical problems that will need resolving before it is a viable neural interface ready for clinical trials. One problem is that when implanted and stimulating, the current from the active electrode was leaking into surrounding channels and was not only triggering the desired neurons, but also those in nearby channels. This means that if the sensations were being interpreted by the brain, it would not be able to know where a particular sensation came from.

The second problem is to do with the biocompatibility of the device. Along with other devices of this nature the body can reject the implant over the long term, rendering it useless as a chronic implantable solution [25].

1.5 Contributions to Thesis

The hypothesis of this Ph.D. is that the current leakage problems of the SPNI can be solved by exploring alternative designs of the device, and that the method of redesign will open up avenues to enable the device to overcome the limitations associated with biocompatibility.

Prior to this Ph.D. the published works on the SPNI have included a device that was rolled so that the struts of the channels were pointing inwards. The sealing of these channels was incomplete due to the non-perfect alignment of the top of the channels with the adjacent substrate layer. In an attempt to resolve this issue, it was proposed that, if the SPNI were to be rolled in the opposite direction, with the struts of the channels pointing outward, that a thin insulating layer could be added to the SPNI. The layer would then be pulled taut across the channel openings to ensure a good seal, due to the modified rolling configuration. This would limit the ionic flow between channels, hence reducing the signal cross-talk observed in previous studies.

The idea of rolling in the opposite direction goes against one of the core structural concepts of the SPNIs design, in that the gold layer which is used as a conductor is located in the stress neural plane of the device so that it does not break. During the work conducted for this thesis it was shown that the gold being placed in the stress neutral region is not a requirement for the design of such devices due to the lamination effect afforded by the two layers of polyimide in between which the gold resides.

After the durability of the gold within polyimide was proven, the SPNI was then sealed with a thin film of silicone with a view to insulating individual channels. The effectiveness of this layers ability to insulate was then observed using a signal leakage measurement method.

Finally, silicones are used in other types of implant and can be doped with various drugs to encourage host adoption of the devices. This property of silicone was tested in the domain of neural interfaces to see if a programmable release rate of active drug could be used to improve the choric viability of the SPNI.

1.6 Overview of Thesis

The thesis will in chapter two go on to cover the theoretical considerations required in the following parts of the thesis. It will start by covering neurophysiology and the method by which nerves communicate (the action potential), followed by a review of relevant literature and a discussion about the design of the SPNI.

In chapter three the text will move on to discuss the methods of fabrication used for the SPNI. It will discuss microfabrication methods employed during its development.

Chapter four will then discuss the redesign of the SPNI and how the internal stresses within the device are not prohibitive to the new design. A bending methodology will be described and it will be shown that the structural design of neural interfaces is less sensitive than initially thought.

Chapter five will discuses theoretical considerations of electrodes and will model the electrode interface. The model and the measurement methods will then be validated with a CNS interface which is made of larger more ideal electrodes than those found in the SPNI.

Chapter six will go on to utilise the results found in chapter four and include a thin film of PDMS in the SPNI structure; used to insulate the device. It will be shown how this insulation of the channels should reduce the interchannel cross talk as measured in previous SPNI experiments.

Chapter seven will outline the methods by which the insulating film can be used as a drug delivery mechanism, aimed at increasing chronic viability of neural interfaces.

Chapter eight will put the results in appropriate context, will conclude the findings of the thesis and will offer proposals for future work required to further progress the field.

CHAPTER 2

NEURAL ENGINEERING - A BACKGROUND

This chapter will begin with outlining the anatomy of the nerve and how nerves are used as communication conduits in the body. Following this will be a review of the relevant literature surrounding the SPNI and this project. Much of the information about the biology of the nervous systems presented here is available in standard textbooks on the subject and has been compiled for this chapter from [29] & [30], unless otherwise stated.

2.1 Neurophysiology

The nervous system allows packets of information to be routed around the human body. It is the system that allows animals the ability to sense and interact with their environment. The nervous system is very broadly separated into two functional units. The Central Nervous System (CNS) which is composed of the brain and spinal cord and the Peripheral Nervous System (PNS) which consists of all neural matter outside of the CNS including all motor and sensory nerves. Information being passed around the nervous system can either be toward the CNS (afferent) or towards the PNS (efferent). This discussion will mainly focus on the PNS, as the SPNI is designed for use on large peripheral nerves.

The nervous system contains many different types of cells and cell variants, the two most important to this discussion are the neuron and the Schwann cells.

The basic information transmitting unit of the nervous system is the neuron. The neurons anatomy consists of the parts, as shown in figure 2.1. Firstly the cell body or soma which contains all of the organelles required for the running of the cell. This is where all of the proteins for growth hormones, neurotransmitters etc. are produced on instructions from the nucleus of the cell, also located in the soma.

The axon is used to pass outgoing signals to other cells. The region where the base of the axon meets the soma is the axon hillock. It is from this region where action potentials are initially generated. These signals are then sent away from the cell, down the axon. Figure 2.2 shows how axons are arranged in a nerve.

Finally there are dendrites, that have a similar role to axons, but rather than sending information away from the soma, dendrites direct information toward it. Axons can be as long as a meter or more, whereas dendrites are significantly smaller. An axon from one cell will interface with a dendrite of another target cell. However, an axon and dendrite of separate cells cannot directly continue the propagation of an action potential. Where the one cell ends and the other begins is an interface region; the synapse. Synaptic propagation uses neurotransmitters to exchange information and is therefore distinct from the general propagation of an action potential down an axon or dendrite.

2.2 How Signals Propagate - The Action Potential

The action potential (AP) is the method by which information can be transmitted through a neuron and its axon. It is a self sustaining electrical excitation that traverses the cell, from its trigger point to all other parts of that cell. In this way information can be transmitted from one side of the cell to the other, where via a synaptic junction, the information can be passed on to an adjoining cell.

To understand the action potential, we must take a look at ionic movements across a neuron's cell membrane.

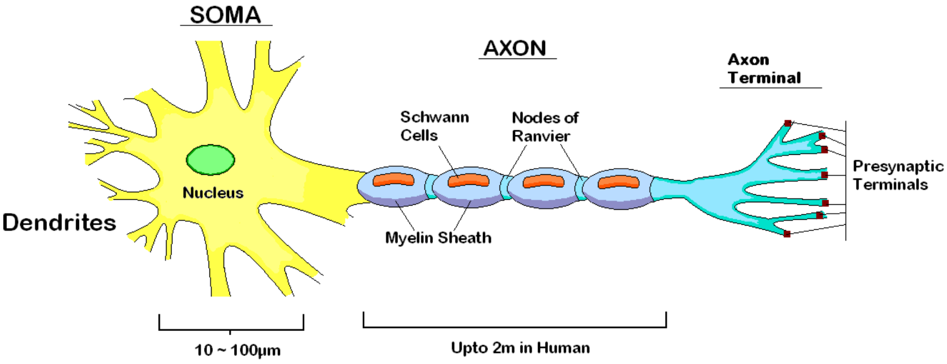

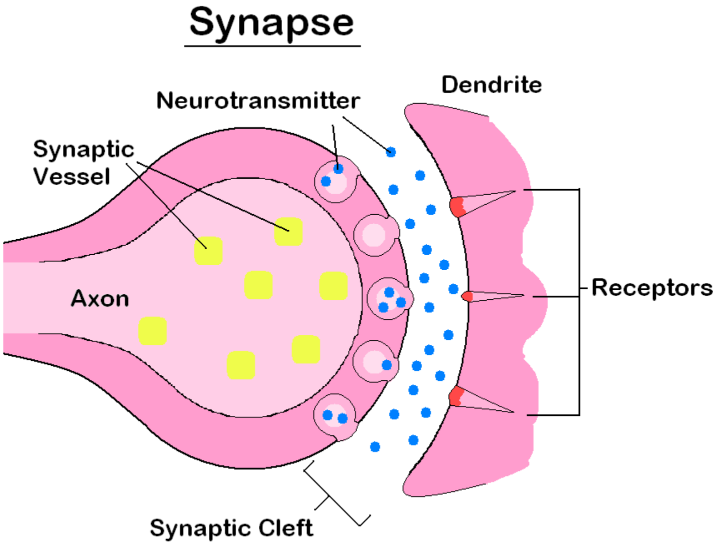

Figure 2.1: Taken from [31]. Top: depicts a neuron, signals would usually propoagate from left to right. Schwann cells cover the axon. Bottom: shows a synapse, the method by which adjoining neurons exchange information.

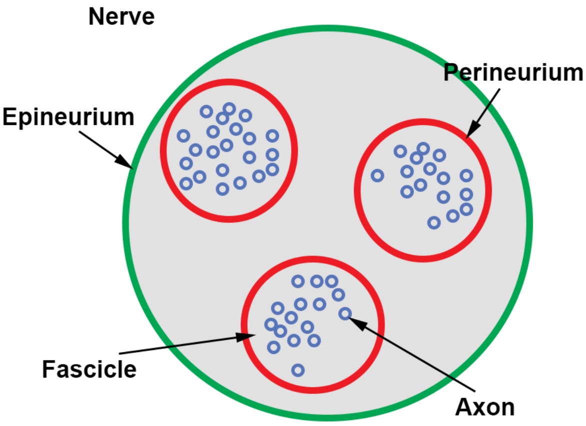

Figure 2.2: Schematic of a nerve containing three fascicles which in turn contain several individual axons. The different neural interfaces couple with different parts of the nerve.

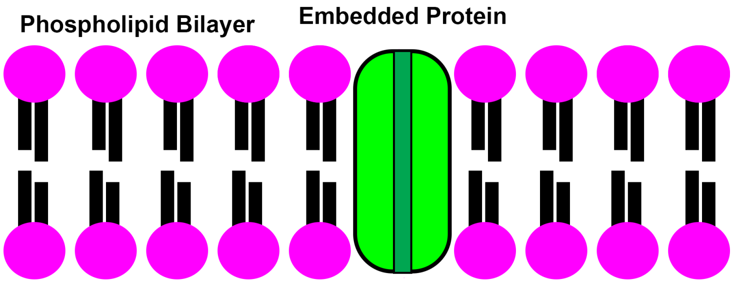

Figure 2.3: Cell walls are made up of a phospholipid bilayer, made up of a hydrophilic head and a hydrophobic tail. Embedded within the cells walls of neurons are proteins which enable their electrical functionality.

2.2.1 Ionic Movement

Neural action potentials are made up of self sustaining ionic flux across a cell membrane. The cell membrane of any cell is largely constructed of a phospholipid bilayer which maintains the cells integrity by preventing cell components and nutrients from leaving, and unwanted molecules from entering. Small particles, such as ions, however can traverse this boundary, with the help of active channels embedded within the cell wall (figure 2.3). Inside of the cell, if considering potassium for example, there is usually a higher concentration of ions than outside of the cell. Ions will therefore move along the concentration gradient and migrate out of the cell and as ions are charged particles, and a potential difference is maintained across the membrane. This is the membrane potential.

If we take K^+ as an example. As more K^+ move across the cell membrane by the concentration gradient, more positive charge leaves the cell. As like charges repel, the build up of positive charge in the extracellular space repels more positive ions from leaving the cell. The concentration gradient and potential gradient therefore oppose each other and as a result an equilibrium concentration is established. The potential difference across the cell under this equilibrium condition is the equilibrium potential.

This equilibrium potential can be calculated for each ionic species via use of the Nernst equation, equation 2.1.

$$E_x = \frac{RT}{zF} \ln \frac{[x]_o}{[x]_i} \tag{2.1}$$

Where E_x is the equilibrium potential, R is the universal gas constant (8.31 J K^{-1} mol^{-1}), T is the temperature in Kelvin, z is the charge of the ionic species, F is the Faraday constant; the electric charge per mole of electrons (96,500 C mol^{-1}), $[x]_o$ is the extracellular concentration of the ionic species X and $[x]_i$ in the intracellular concentration of that ion.

For K^+ the equilibrium potential is -95 mV.

The cell contains more than a single type of ion, and it is the culmination of the behavior of the entire ion set that dictates the resting membrane potential of the cell as a whole. The permeability of the cell membrane to each ionic species however is not the same, thus in order to calculate the potential difference across the membrane of a cell, the Goldman equation is used, equation 2.2.

$$V = 61 \log \frac{P_k[K^+]_o + P_{Na}[Na^+]_o + P_{Cl}[Cl^-]_o}{P_k[K^+]_i + P_{Na}[Na^+]_i + P_{Cl}[Cl^-]_i} \tag{2.2}$$

Where V is the voltage maintained across the membrane, P_x is the permeability of the membrane to ion X, $[X^y]_o$ is the concentration of ion x with charge y in the extracellular space, and $[X^y]_i$ is the same for the inside of the cell.

Thus the voltage contribution by each ionic species is a function of how permeable the membrane is to that species.

2.2.2 Cell Wall Proteins

The permeability to individual ion species is dictated by the cell membrane structure.

Embedded within the cell membrane are ion pump proteins that maintain these ionic concentrations. The most notable of which is the Na^+/K^+ ATPase which uses the energy provided by ATP molecules to take three Na^+ out of the intracellular space in exchange for two K^+ into the cell. Thus maintaining ionic and potential gradients.

There are also channel proteins in the cell membrane, that act as selective junctions through which specific ions can flow. How permeable these proteins make the cell membrane to a particular ion can be dictated by different factors depending on the individual protein under consideration. These include thermally gated channels that increases ion permeability with temperature, mechanically regulated channels that deform under mechanical stress to allow more ions to flow, ligand-gated receptors that allow more ions though when exposed to particular biochemical messages, or the classic example - the voltage-gated channel that increases ion permeability when a voltage is applied across the membrane. All of these proteins can be used to trigger an action potential but it is the voltage-gated channels that allow AP propagation down the length of the cell.

The voltage-gated ion channels are regulated by the voltage across the membrane, when the membrane voltage exceeds a certain threshold potential (usually between -55 and -50 mV) the channels open, allowing for the movement of a specific ion through them. By this mechanism an action potential can be triggered and propagated.

2.2.3 The Action Potential

An external stimulus acts on the cell that causes the membrane to depolarise and reach a threshold potential, this could be caused by any of the triggers mentioned in the previous section. Once the threshold potential has been reached, Na^+ gates open, increasing the membranes permeability to Na^+. Due to the concentration gradient, Na^+ flood into the cell, dramatically increasing the membrane potential. As the membrane potential continues to increase the electrochemical driving force acting on Na^+ decreases as the equilibrium potential is reached. At this point K^+ channels open, caused by the voltage change, allowing K^+ to leave the cell which brings the membrane voltage back down as ions leave the cell. There is an undershoot where K^+ permeability is higher than the resting condition. K^+ channels close and the resting potential is regained. This process can be seen in figure 2.4.

After each AP there is a refractory period which occurs in the undershoot phase. This is a phase where another action potential cannot be triggered by an external stimulus due to the extra potential barrier. After each AP the cell membrane expends energy to restore ion homeostasis via active transport of ions across the cell membrane by pump proteins.

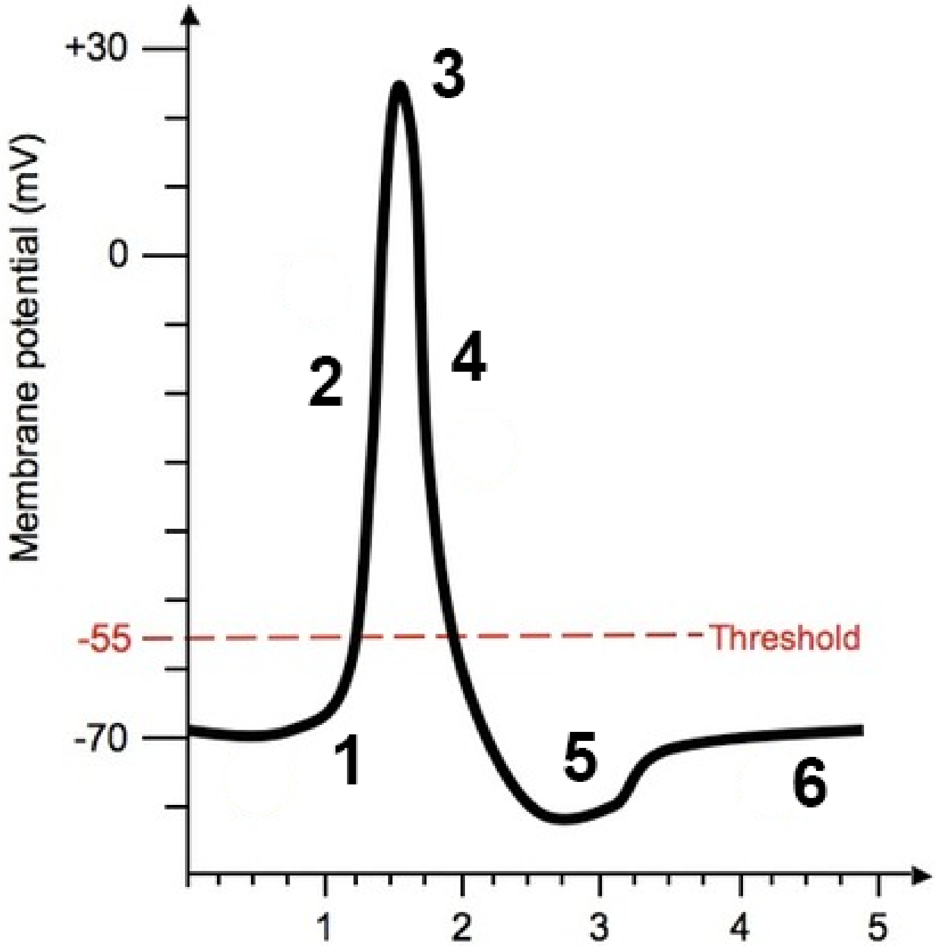

Figure 2.4: The action potential of a neuron 1) External factors increase the membrane potential and sodium channels open to allow sodium ions to flow into the cell. 2) If the stimulus is larger than the threshold positive feedback takes hold and more sodium ions influx. 3) The electrochemical driving force behind the sodium decreases. The sodium channels close and potassium channels open allowing potassium ions out of the cell. 4) The exiting potassium ions decrease the membrane potential. 5) Potassium conductance is temporarily higher than at the resting condition and causes an undershoot 6) The potassium gates close and resting potential is restored.

2.2.4 Myelination and Extracellular Impedance

Myelinating Schwann cells are extremely important to the functionality of the nervous system. These cells are a particular type of glial cell. Glial cells surround axons performing vital functions that aid in the functionality of the neurons. Other types of glia can perform functions such as nutrient or waste transport or have immune functions; myelinating Schwann cells in the PNS have a very particular function. These cells provide a myelin sheath around the axons they surround.

Schwann cells wrap around individual axons, providing support and electrical insulation to the axon, as seen in figure 2.5. The myelin insulation these cells provide, prevents a continuous action potential running along the surface of the axon, as action potentials require a voltage difference across the cell membrane, which the Schwann cell's insulation prevents. This instead leads to another mechanism of conduction dubbed saltatory conduction.

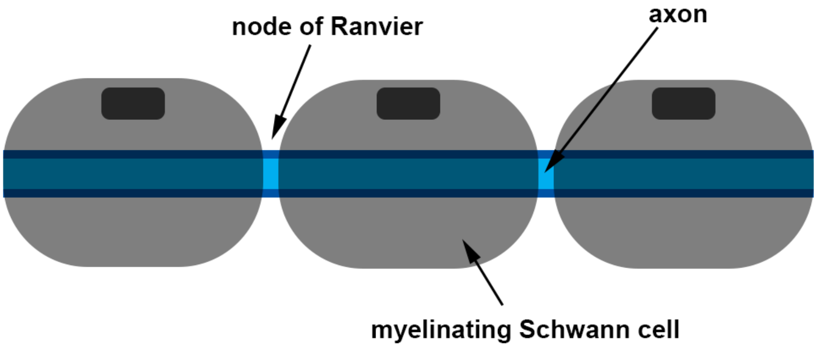

Figure 2.5: Schwann cells encapsulate the axon, between adjacent Schwann cells there is a gap; the node of Ranvier. In this region the proteins accumulate. The action potential jumps from node to node in saltatory conduction.

2.2.5 Saltatory Conduction

In saltatory conduction, ionic channels through the axon membrane accumulate at regions where Schwann cells meet. At this point there is no protection from the Schwann cells and a voltage can be maintained across the axons cell membrane. These points of Schwann cell intersection are nodes of Ranvier, named after their discoverer (figure 2.5).

If we consider an axon with several nodes of Ranvier down its length; at the first node, when an action potential meets it, the node is polarized, becoming negatively charged with respect to the rest of the axon. Due to this a passive current runs down the length of the cell to the next node, which then causes an action potential to form at the node, introducing an active current that can then passively travel down to the next node. This process continues down the entire length of the neuron with the voltage ‘jumping’ from node to node. This process massively increases the conduction velocity of signals down a nerve and enables nerves to be longer when they are coated in Schwann cells. This is a natural example of how action potentials can be modified using biological means. The Schwanns cells increase the extracellular resistance of the axon and thus make signals propagate more strongly.

2.2.6 Neuronal Stimulation

Due to the nature of action potential generation and saltatory conduction, it was shown by Hodgkin and Huxley [32, 33] that it is possible to stimulate neural tissue by providing an external voltage source. This voltage depolarises the neuron, causing the threshold voltage to be exceeded, which leads to the propagation of an action potential.

This stimulation can be applied by a probe or electrode that is in very close proximity to the cell. In myelinated axons, the success of a stimulation relies on the proximity of that electrode to a node of Ranvier, due to their insulating effects. A node of Ranvier can be between 1 and 2 μm long, whereas the internode spacing can be up to 1.5 mm, meaning that electrodes are often too small to have a high probability of successfully interfacing with a node of Ranvier.

2.3 Neural Interfaces for Implantation

Neural interfaces are biological-electronic transducers that couple nervous systems to electronic circuitry [25]. There are many different methods of achieving this interface as explored in the previous chapter. There is also a trade off between selectivity and invasiveness that must be considered when designing neural interfaces. However, state-of-the-art prosthetics require high selectivity and will increase this high demand for detail as the stimulation of sensation is incorporated into the devices. This requirement for high selectivity eliminates many of the electrodes that have previously been used for neurophysiological research, as they either cannot support dense enough electrode numbers (in the case of shank electrodes) or are limited by their lack of proximity to individual axons (in the case of extraneural electrodes).

2.3.1 Cuff Electrodes

Cuff electrodes are insulating sleeves that surround a nerve fascicle and carry electrodes on their inner surface, facing the nerve [34]. They have been useful in applications where the whole nerve was required to remain intact, but lack the spacial resolution required to drive sophisticated prosthetics [25].

The method of enclosing the nerve in an insulating sheath increases the extracellular resistance for current leaving the nerve fascicle, this results in a higher voltage recording when compared to other neural surface electrodes. The lack of selectivity however, rules this kind of device out of being able to drive advanced prosthesis as with current and foreseen signal processing technology it is impossible to extract the required information detail from the surface of a nerve fascicle containing many neurons, as several axons located closely together give identical signal profiles.

2.3.2 Regenerative Neural Interfaces

Regenerative interfaces rely on the phenomenon whereby nerves regenerate when severed. When a nerve is severed, growth cones protrude from the proximal nerve stump, the Schwann cells guide this growth as close to the original path as possible. At the same time Wallerian degeneration takes effect on the distal stump and the detached axon recedes as the new growth attempts to replace it. This process is complex in nature but can happen at an incredible rate, with rates as high as 0.8 mm per day in humans.

Regenerative neural interfaces encourage individual axons to regenerate into electrode sites, rather than the electrodes sitting outside of the nerve fascicle. Micro-machined silicon sieve electrodes are common, whereby microscale holes are etched onto the surface of a silicon wafer with a subset of the holes metalized so that action potentials can be captured from the regenerated axons [35]. These devices have been shown to be capable of supporting the regeneration of nerves and enabling both recording and stimulation of axons in multiple types of nerve [36, 37].

The geometry of these devices is critical to their function, as neurons regenerate better through devices that provide around a 100 μm aperture through which the neurons grow [38]. Sieve electrodes have been fabricated out of several different types of material [37] including ceramic, Teflon, epoxy, paraylene and silicon [27, 37–39].

These devices preform well but offer a low signal to noise ratio. They also preform poorly in terms of biocompatibility as the tethering of connectors coupled with high Young's moduli of materials used result in relative movement between electrode and body which increases the ferocity of the foreign body reaction [39].

2.3.3 The Spiral Peripheral Nerve Interface

The SPNI is an example of a regenerative neural interface that encourages individual axons to split from their parent fascicle and grow down the individual channels. Devices that encourage the axons to grow down insulating channels show dramatic improvements in the signal to noise ratio [40–43]. This is due to the fact that enclosing the axon increases the extracellular resistance, and current leaving at the nodes of Ranvier rather than spreading into the extracellular space, is forced to run parallel to the nerve through the channel (figure 2.6). This has two major effects, it increases the measured voltage at any electrodes embedded within the channel and also stops the proximity to a node of Ranvier from dictating how successful electrode placement will be, as voltage is more evenly spread throughout the channel.

The SPNI design allows for a high degree of selectivity. In a large enough device, more channels encourage finer grouping of individual axons which may give enough selectivity to drive complex targets such as advanced prosthetics or implanted stimulators in denerved limbs [25].

Increasing the extracellular resistance is not only beneficial to the recording of neural signals, but also to their stimulation. For the same reasons as stated above, in terms of current flow and proximity to nodes of Ranvier, insulating channels offer a large efficiency boost when stimulating nerves, reducing the charge injection required for AP trigger from 1-8.5 nC [44–46] down to 0.05 nC [41]. Reducing the charge injection requirement by up to 99.4%! Whilst delivering the same spacial selectivity advantages.

It has also been shown that *in vivo* axons can regenerate through the SPNI with 100 μm diameter channels to reconnect to peripheral targets, giving the ability to record from and stimulate acquired axons [25]. 70% of the channels were shown to have successful reinnervation. Not only do nerves grow down the device, but it has been shown, using a non-destructive micro-CT scan, that blood vessels can also grow down the channels and may provide biological support to recruited axons [47].

In one study six Lewis rats were implanted with the SPNI and were allowed to reinner-

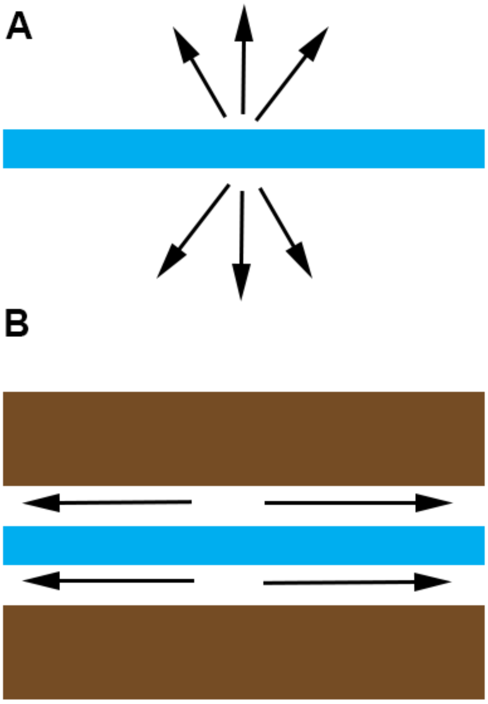

Figure 2.6: a) In a uninsulated axon, current leaks into the extracellular space, b) if enclosed the current is forced down the channel, increasing the extracellular resistance and therefore increasing the voltage within the channel.

vate for three months [25]. With the rodents under anesthetic, the devices were exposed and stimulation of the hind limbs of the animals produced large and clear signals from the SPNI, along with this stimulations of 45% of functioning electrodes resulted in muscle activity. Hence, proving that not only had proximal axons reinnervated distal remains, but that stimulation of the electrodes was a viable method of exciting action potentials within the nerves.

The stimulus currents required to elicit muscle reactions were low when compared to previous technologies, but were still several times higher than similar cast silicone devices that were presented in the same piece of research. The explanation for this is that the cast silicone had fixed channels, whereas the SPNI was rolled and it is thought that imperfect sealing between layers of the roll were allowing current to leak out of the channels into the surrounding device.

This issue also reduced the selectivity of the device, in some cases enough current from a stimulated channel leaked into neighboring channels to stimulate their nerves also. 31

out of the 104 distinct motor unit reactions observed could be triggered by more than one electrode.

Although the SPNI has been shown to be a successful neural-electronic transducer it proved difficult to measure action potentials from limb stimulations that were not electrically stimulated and time-locked. Natural stimulations such as manipulation of the rodent digits were difficult to identify and significant improvements in the SNR will be required before reliable detection of these spontaneous signals will be possible.

Improved channel sealing processes will be required during the fabrication processes of the SPNI to solve these issues [25].

2.4 Previous Design of the SPNI

The SPNI was designed to provide 100 μm channels down which axons could grow, the concept for which can be seen in figure 2.7. 70% of channels with 100 μm width support regenerated axons [25, 42]. This is in contrast to 70 μm and 55 μm channels only supporting 50% and 30% channel population respectively.

The SPNI has 180 such channels, 20 of which have electrodes embedded within the center of the channel. Gold was chosen as the electrode material due to its high conductivity and low toxicity along with polyimide as the material for the SPNI substrate and channel walls, again for its low toxicity and ease of fabrication.

The gold conductor was intended to be placed close to the stress neutral region of the device, as outlined by [48], to prevent the mechanical stresses from rolling the SPNI breaking the gold. The stress neutral plane was shown to require 20 μm of polyimide to be deposited before the gold layer, and further encapsulation by 5 μm of PI before applying the channel layer. This model however was incorrect, and does produce significant strain on the gold layer, this will be explored further in later chapters.

The aim with this design was to present a robust, reliable peripheral nerve interface that could provide sufficient resolution to drive complex prosthetics.

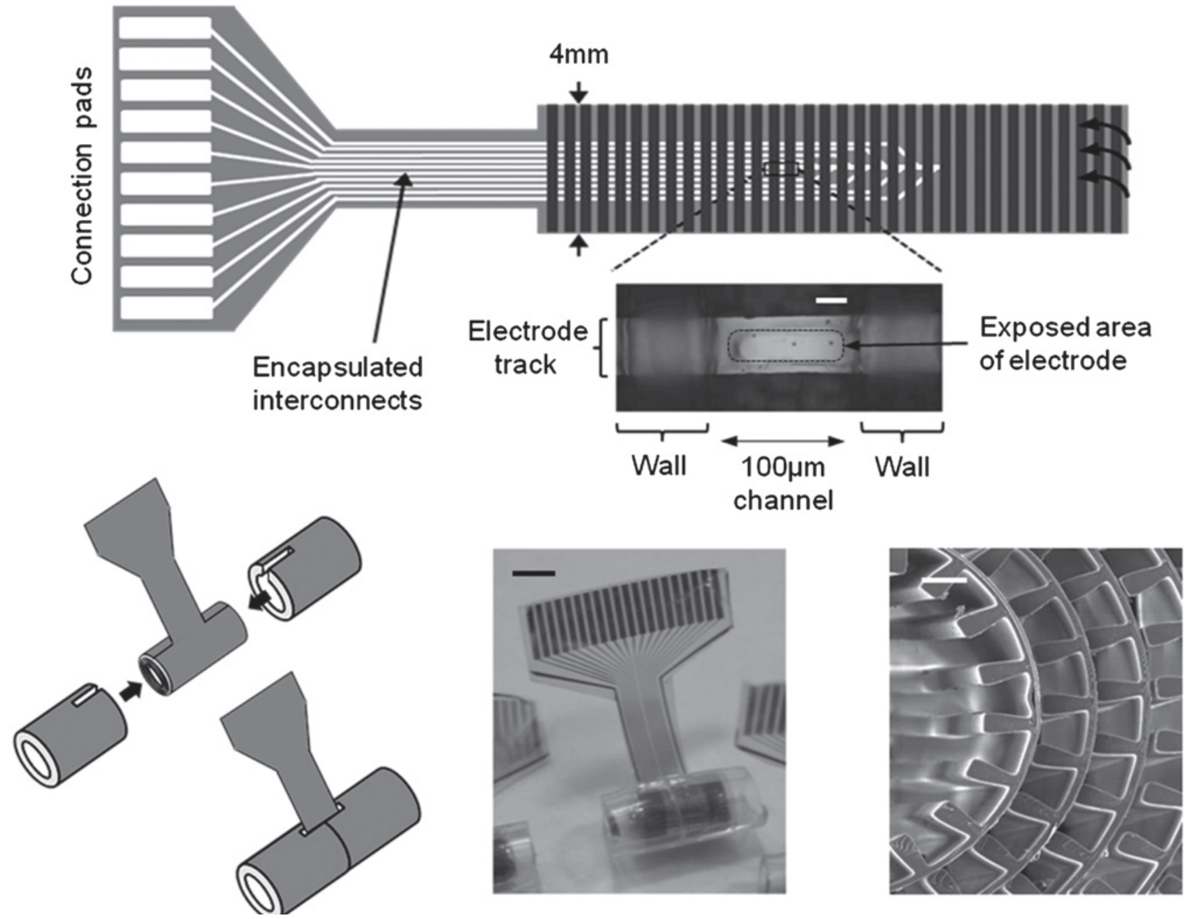

Figure 2.7: Taken from [25], showing the initial design concepts of the SPNI. The flat geometry of the top image is constructed using microfabrication techniques and rolled into a spiral which is held in place by a silicone sheath.

2.4.1 SPNI Key Advantages and Limitations

The main advantages of the SPNI are its potential selectivity resulting from the branching of individual groups of axons being isolated by the insulating channels along with the dramatic increases in SNR that this kind of design promises to offer. Other silicone devices capable of these feats have also been presented, but these devices are cast out of silicone and require surgical skill to assemble. The SPNI provides a viable route for mass producible regenerative neural interfaces with sufficient resolution and biological amplification to be useful for the applications previously described.

However, before the SPNI is to be introduced into further clinical studies, several issues with its design need to be remedied. The most urgent of which is the current leakage causing reduced stimulation resolution, arising from the imperfect sealing of the helical SPNI layers. The other outstanding issue that would improve the SPNIs performance is its biocompatibility, if it were possible to modulate the foreign body response to the SPNI and the formation of scar tissue, the long term SNR would be maintained, and it may also be possible to reduce the caliber of the channel dimensions to create a higher density device [25].

This chapter has outlined the neurophysiology and technology that pertains to current neural interfaces. The next chapter will go on to outline the methods by which the SPNI is produced.

CHAPTER 3

METHODS OF FABRICATION

The previous section demonstrated how microfabricated neural interfaces can interface with nerves via micro-electrodes. This section will describe methods by which the SPNI electrode array is fabricated and tested. Starting with a brief overview of the SPNI fabrication process, going on to describe the technologies used in the fabrication. The text goes on to provide detailed methods and ends with electrical measurement methods commonly used with electrode devices.

3.1 SPNI Overview

To enable batch production, the SPNI is a three dimensional spiral constructed with two dimensional films of polymer and metal. A silicon wafer with oxide layer is used as a carrier and layers of the device are built up using standard microfabrication techniques in a class 10,000 (ISO 7) clean room to prevent dust contamination between the layers. The general structure of the SPNI can be seen in figure 3.1 and the overarching fabrication process can be seen in figure 3.2.

The entire structure is built on a standard single sided silicon wafer and is built up in layers. The polymer substrate is photosensitive Polyimide (PSPI or PI) due to its ease of use and past proven biocompatibility. However PSPI, unlike non-photosensitive polyimide, sticks irreversibly to silicon dioxide, but it does offer a chemistry that is suitable

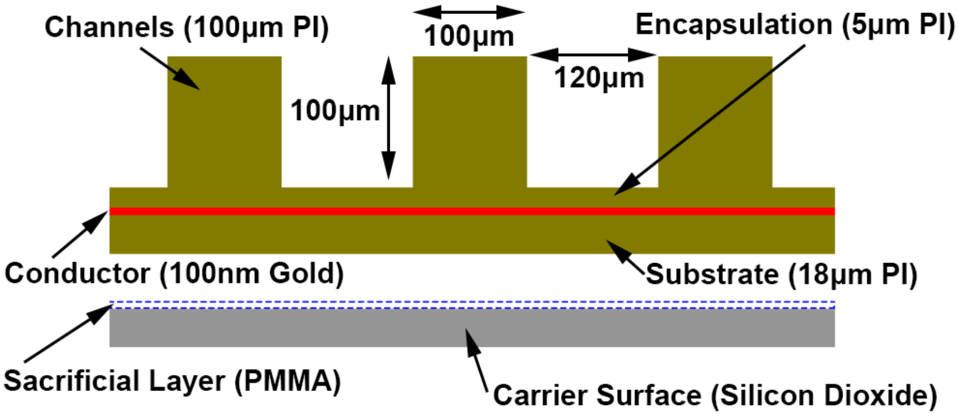

Figure 3.1: The standard SPNI structure.

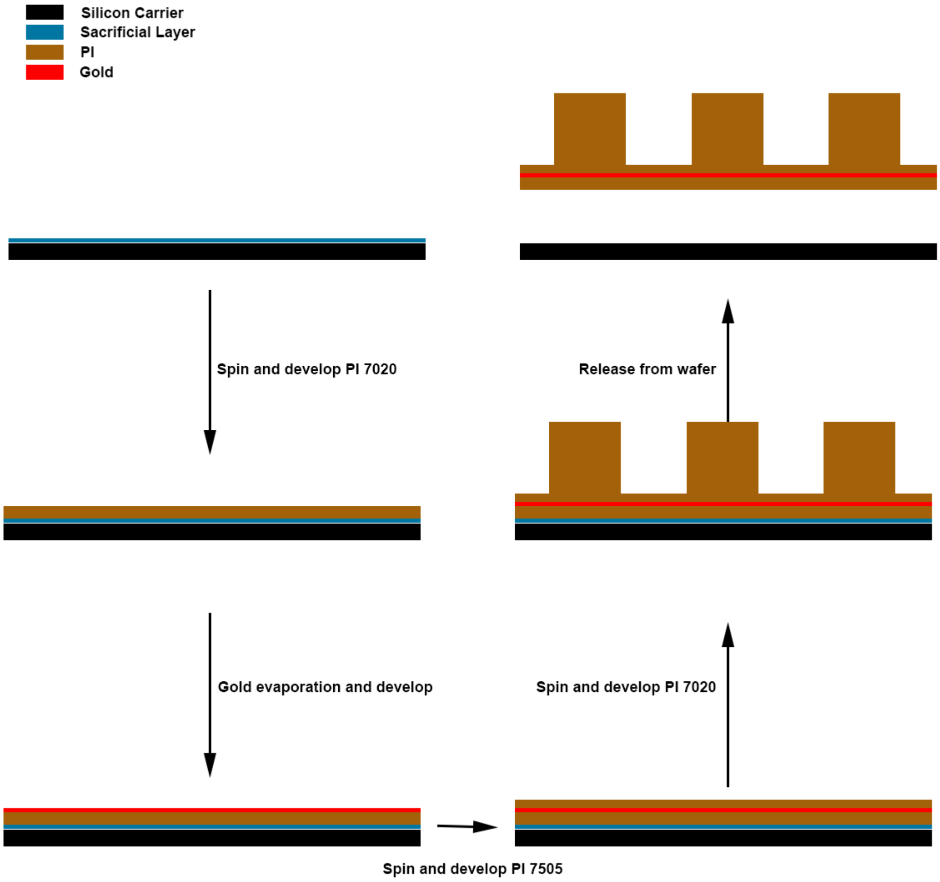

Figure 3.2: The overall process of the SPNI fabrication process. Starting from the top left, a sacrificial layer is added to a silicon wafer, a thick layer of polyimide is then added and developed, followed by a thin film of gold, which is then developed, after this a thin layer of PI is added and developed, with the channel layers being defined on top of this. Finally the sacrificial layer is dissolved and the SPNI is released from the wafer.

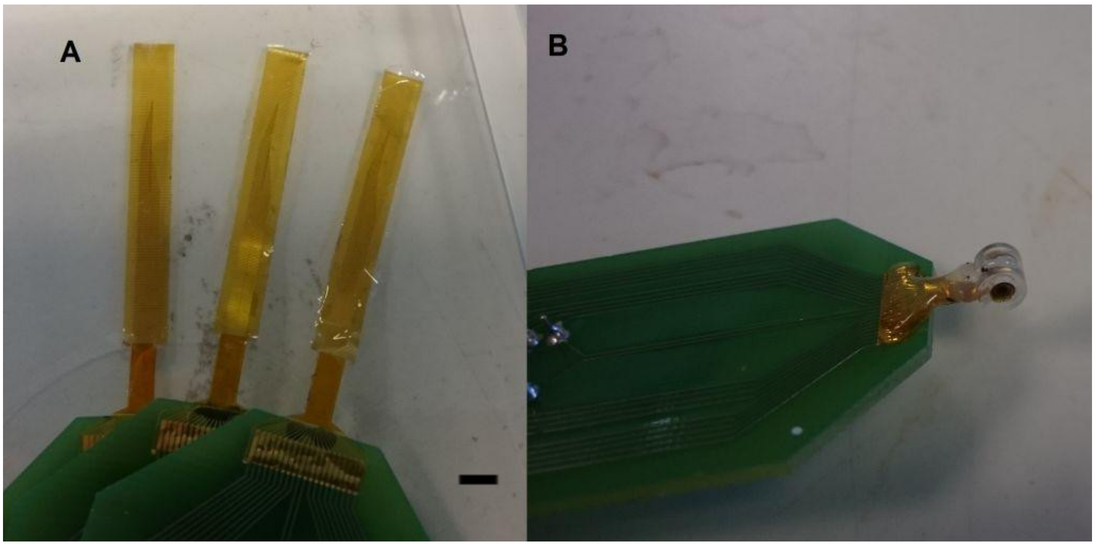

Figure 3.3: A completed and released SPNI, on the left flat, on the right rolled. Scale bar is 4 mm.

for photo-patterning. Because of this adhesion problem a sacrificial layer is spun onto the surface of the carrier first. After this the 18 μm substrate layer of PI can be spun and developed followed by a 100 nm evaporation deposition of gold to act as the electrical conductor for the electrodes.

The gold is covered with a photoresist which is also developed, the gold can then be etched and cleaned. A 5 μm layer of encapsulation PSPI is then spun and electrode sites developed and exposed. The channel layer is then added by spinning 100 μm of PI and then developing into the channels. The device is cleaned again then given a hard bake to fully cure the polyimide. Following this the devices are released from the carrier, by dissolution of the sacrificial layer, and harvested. They are ball-bonded to a PCB and tested for integrity.

A 20 μm polydimethylsiloxane (PDMS) film is then spun on a separate wafer, released, cut to size and placed over the SPNI, sealing it. The device is then rolled and held in place with a silicone sheath. Giving a final device which can be seen in figure 3.3.

The processes used in SPNI fabrication have been previously outlined in [31] and [25].

3.2 Microfabrication Techniques

To follow is a brief description of each of the technologies used to fabricate the SPNI. After this there will be a detailed methodology for the SPNI fabrication.

3.2.1 The Cleanroom

Microfabrication processes are generally carried out in cleanrooms. These provide an environment with a consistently circulating purified airflow so that airborne contaminates are removed, preventing them from interfering with the microscopic structure of fabricated devices. The environment is also thermally stable, at 20 $\circ$C, with fixed humidity of 40%. This is to prevent lithographic processes from instabilities caused by environmental fluctuations. Personnel in clean rooms ware protective full body clothing which is lint free, preventing cloth, hair or skin partials from contaminating the room or the samples. Air flow is designed to minimize local fluctuations and to prevent microclimates from forming within the cleanroom. The light in the cleanroom is also filtered so that photosensitive materials are not inadvertently exposed during processing. Every item undergoes decontamination processes before entering to maintain the cleanrooms integrity. This includes piped in water which undergoes RO filtration and sterilization before entering. The cleanroom at the University of Birmingham, Department of Electronic, Electrical and Systems Engineering was used for all device fabrication.

Table 3.1: Physical properties of silicon. Values taken from [49].

Physical Property	Value
Density	2.33 g/cm^3
Young's Modulus	190GPa
Yield Strength	7 GaPa
Intrinsic Resistivity	2.3×10^5 Ωm
Coefficient of Thermal Expansion	$2.6 \times 10^{-}6$ °C^{-1}
Melting Point	1421 °C

3.2.2 The Silicon Carrier

All fabrication processes discussed herein used a 100 mm diameter (100) silicon wafer with a 250 nm oxidized surface as the carrier to all other layers. Silicon wafers offer several advantageous properties when used in microfabrication. Silicon is chemically stable, providing good resistance to many lithographic chemical processes. It has good thermal stability, very high strength and high melting point to compliment its extremely flat surface profile which allows for interference free fabrication of subsequent layers. Some of the more useful properties for microfabrication of silicon are shown in Table 3.1.

3.2.3 The Spinning of Thin Films

Spin coating is a process whereby a material to be deposited is dissolved in a solvent and then placed in its liquid form on the center of a wafer. The wafer is then spun at high speeds, usually of the order of 1000 rpm. The centrifugal force acting on the resist, caused by this spinning, forces the liquid to spread out in a thin layer over the surface of the wafer. Following this the wafer is baked to drive away the solvent, which leaves a thin film of the desired material covering the wafer surface.

The speed and duration of the spinning along with the viscosity of dissolved material determine the thickness of the overall film before baking. The thickness generally decreases as the inverse square root of the spin speed.

In the experiments discussed in this thesis spin coating is used for all photoresist, polyimide, poly(methyl methacrylate) (PMMA) and PDMS layers. Spin profiles for each will be presented later in this chapter and all spin-coated materials were applied using an automatic spin-coater (WS-650MZ-23NPP, Laurell).

3.2.4 Photolithography

Photolithography is the process of defining flat geometries using light and its effect on different materials. This is made possible by the fact that some polymers change their chemical properties when treated with UV light.

Generally in photolithography a photosensitive polymer (or photoresist) is spin coated onto a carrier wafer to form a thin uniform layer. The sample then under goes a soft bake which drives off most of the solvent from the polymer. The wafer is then placed into a mask aligner (Parallel Light Mask Aligner PLA-501F, Canon) which holds a mask of the geometries to be realised on the resist surface. In this thesis all photolithography is 1x lithography, i.e. the pattern transferred onto the wafer is the same size as the pattern on the mask with no scaling which can be common in some applications.

The mask details all geometries that are to be transferred onto the photoresist. This can be done in one of two ways depending on the type of photoresist used. A positive photoresist when exposed to light will become soluble in the developer. Hence when designing a mask for a positive photoresist, it must be ensured that desired features are not exposed to light. Conversely a negative resist will polymerise when exposed to light, making it less soluble in the developer. Thus required geometries are deliberately exposed to light, and unwanted material is masked, so that it will dissolve away. This process is summarised in figure 3.4.

If there are already geometries on the wafer that is about to be exposed, then alignment of the mask and the wafer is required so that features of the different layers will align. This is done by placing the wafer and mask in a mask aligner which allows for micro-manipulation of the relative orientations of the wafer and mask. Small alignment marks are often used for this purpose, so that the wafer can be globally aligned whilst only observing a small local region.

Once alignment is complete the exposure takes place within the mask aligner. A shutter leading to a high intensity UV (i-line) bulb is opened, allowing columnated UV light to shine through the mask so that it casts shadow onto the wafer. This process

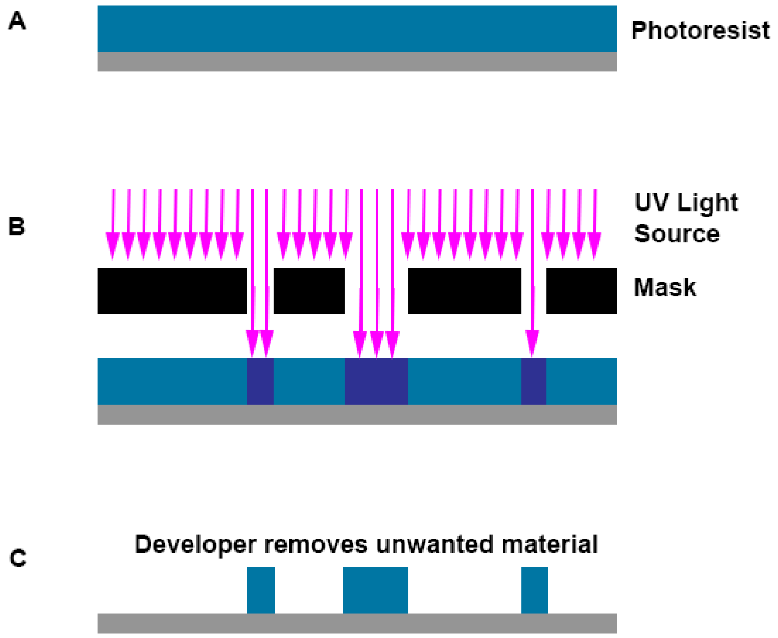

Figure 3.4: General photolithography: A. A photoresist is spun, B. UV light is shone through a mask which causes chemical changed in the resist. C. developer is used to remove undesired features.

only takes a few seconds but in this time, the changes in the chemical structure of the photoresist takes place.

Depending on the photoresist used the sample can then be baked in a post-exposure bake. The purpose of this step is to allow the chemical reaction to fully mature before development.

The photoresist is then developed in a solvent which washes away the susceptible, unwanted parts of the polymer (i.e. exposed regions for a positive resist and non-exposed regions for a negative resist).

With polyimide development this is a two step process whereby a developer reacts with the non-exposed polyimide and a rinse agent then dissolves this.

Finally the structure undergoes a hard bake to drive out any remaining solvent. For the SPNI this step is undertaken at the end of the overall fabrication process after several layers of photolithography.

3.2.5 Physical Vapor Deposition

In microfabrication metalization of previous layers is often required. In this work two methods of physical vapor deposition were used to deposit different metals onto the structure of the SPNI. The first is sputtering and the second is evaporation. In the SPNI a chrome layer is sputtered onto the patterned PI substrate immediately followed by a gold (Testbourn, 99.99% pure) evaporation. The chrome acting as an adhesion promoter for the gold.

Sputtering is a physical vapor deposition technique whereby argon atoms are exposed to an extremely high electric field. The argon atoms are ionised and are attracted with considerable energy toward a negatively charged target. This target is made out of the material to be deposited on the wafer. In the case of the SPNI, this target is made of chrome. As the argon ions bombard the surface of the chrome, chrome atoms are released from the bulk material where they are sent across the sputtering chamber. The chrome atoms then hit into the wafer giving up their remaining energy and forming a coating on the wafer.

Evaporation of gold is the second PVD technique used with the SPNI, demonstrated in figure 3.5. Both sputtering and evaporation take place in a vacuum chamber. In evaporation a metal is heated to its melting point, and due to high vapor pressure of the metal and the low pressure of the chamber, the metal atoms leave the surface of the molten metal to coat the wafer, on which the vapor condenses.

This gold layer is what provides the conductive electrodes within the SPNI.

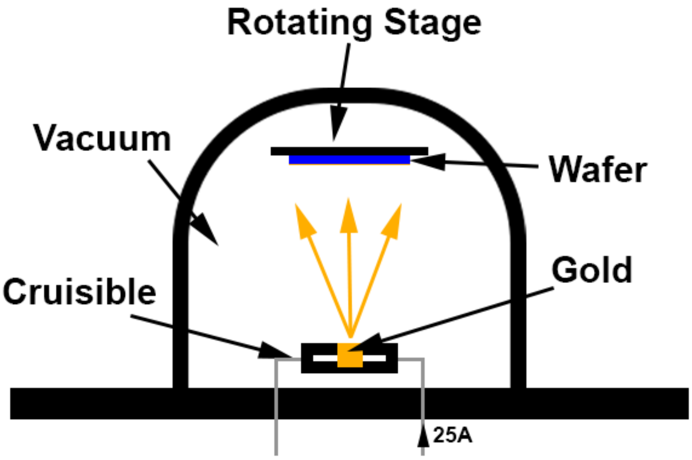

Figure 3.5: Evaporative deposition: a crucible filled with a metal is heated in a vacuum, this causes the metal to evaporate and condense on a target wafer.

3.2.6 Dry Cleaning

The SPNIs are cleaned twice during fabrication; once after metalization and once before final baking. Cleaning is a two step process whereby the wafer is exposed to an oxygen plasma using a Diener FEMTO-A at 70W for 10 minutes, followed by Ultra-Violet O-zone (UVO) treatment using a Jelight, UVO-Cleaner Model: 42 for 20 minutes. It is may be possible to complete the cleaning in one step with a lower power, longer duration plasma treatment, but a dual step process was used for the work presented in this thesis.

The oxygen plasma is an energetic process which etches away contaminates from the surface of the SPNI, particularly descumming the electrodes. Despite this some stable organic molecules present in the metals photoresist can survive this treatment. Due to this the second step, UVO treatment, is used.

In UVO treatments an ozone gas is generated and passed over the wafer, this is energised by a high intensity ultra-violet light. This provides a highly reactive molecule which attacks stable bonds of organic contaminates, desaturating these bonds so that when the wafer is further washed in an organic solvent such as acetone, these contaminates will be dissolved.

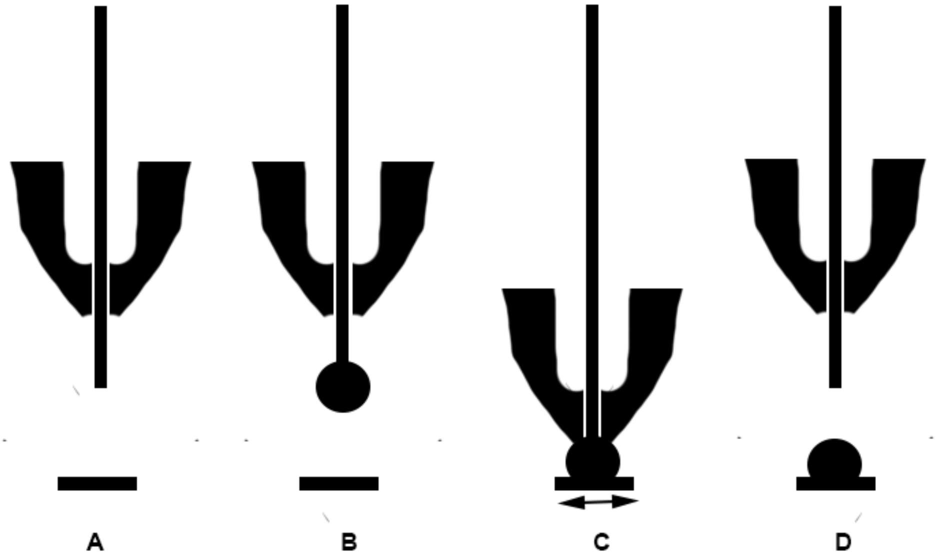

Figure 3.6: Making a ball ball bond involves A. taking a piece of gold wire in a bonding tool, B. a spark is passed across the wire to melt the end of the wire to create a small ball, C. the ball is brought down onto the bonding target and oscillated into the surface with pressure. D. the wire is detached and the ball bond is then acting as a micro-rivet.

3.2.7 Ball Bonding and Micro-rivets

Ball bonding is often used to connect microelectronics to more macroscopic connectors. A small ball of gold suspended on the end of a gold wire is created by arcing a high voltage across the tip of the gold wire. This ball is then pressed against the bonding surface and vibrated at ultrasonic frequencies under force. The wire can then be routed to the next bonding surface and crushed into it, forming a wedge bond, finalising the connection.

A similar technology is used in the SPNI, however, the ball bonds are treated as micro-rivets. Ball bonding is depicted in figure 3.6 and was shown to work with the SPNI by [50]. The trail of the ball bond is cut off so that there is no second connection. Instead the ball is connected onto a gold surface through the connections of the SPNI, forming a mechanical and electronic interface between the SPNI and its PCB connection.

3.3 Fabricating the SPNI

The overall process of the SPNI fabrication can be seen in figure 3.2. For itemised methods for each section, please refer to Appendix A.

3.3.1 Sacrificial Layer

During this research two methods of release were used, one using a polymer sacrificial layer of PMMA and the other using an aluminium sacrificial layer. The two methods are outlined below and their functionalities are compared. A sacrificial layer is required due to the use of photosensitive polyimide. Whereas traditional polyimide can be peeled from a silicon dioxide sublayer, the photosensitive variant adheres irreversibly to a silicon carrier. Due to this a sacrificial layer is used so that all subsequent layers of the SPNI can be placed on top and then at the end of the fabrication process, this layer can be removed, thus releasing all layers subsequently deposited.

Poly(methyl methacrylate)

PMMA is a transparent polymer which is used in many applications varying from shatter resistant glass to inks and paints. PMMA-A9 has a melting point of 160 ° and dissolves readily in strong organic solvents. It is PMMA's susceptibility to organic solvents along with it's resins appropriate viscosity that makes it a prime candidate for use in microfabrication both in casting and sacrificial applications [50].

To begin the process a clean silicon wafer is selected. To ensure that there is no contamination of the wafer it is first cleaned. This is done by spinning it at 1000 rpm and a wash bottle is used to spray the carrier with acetone for a few seconds. Following this another wash bottle is used to rinse with isopropanol to rinse away any excess acetone. The isopropanol is applied before the application of acetone is ceased, to ensure that the acetone does not dry onto the wafer surface. Isopropanol is a cleaner solvent than acetone and does not cause condensation to form on the wafer due to cooling effects. This process

Table 3.2: Spin profile of the PMMA sacrificial layer.

Step	Time (seconds)	rpm
1	2	400
2	2	1100
3	12	850

removes any organic compounds or dust which may have contaminated the wafer during storage. The excess solvent is then driven off the wafer in a flash bake at 120 °C for 5 minutes and left to cool to room temperature for a further five minutes.

The PMMA (PMMA-A9, MicroChem) is spun at settings seen in Table 3.2 to produce a film on the carrier. The spinning is carried out in an automatic spinner (Laurell, WS-650MZ-23NPP). The wafer is then placed on a hotplate at 85 °C for 2 minutes, rising to 130 °C for 10 minutes and finally 180 °C for a further 10 minutes. The sample is then left to cool to room temperature.

The heat ramp is present to ensure that the entire wafer heats up at a similar rate.

From this point onward the structure of the SPNI can be started by spinning a polyimide layer. After the initial device fabrication is complete it will be time to release the devices from the wafer. In order to do this the wafer is submerged in methyl isobutyl ketone (MIBK) for 19 hours. This gently dissolves the PMMA layer allowing the devices to separate from the carrier intact. If a harsher solvent, such as acetone, is used the devices tare as they separate. The timing of this step can be critical in that if left too long the MIBK can begin to permeate the SPNIs, causing them to wrinkle and curl. But if harvesting is attempted too soon, pealing them off the carrier can also cause damage. The optimum time for release is between 19 and 24 hours depending on the individual samples. The ideal conditions are when gently agitating the petri dish the devices float away from the surface of the carrier.

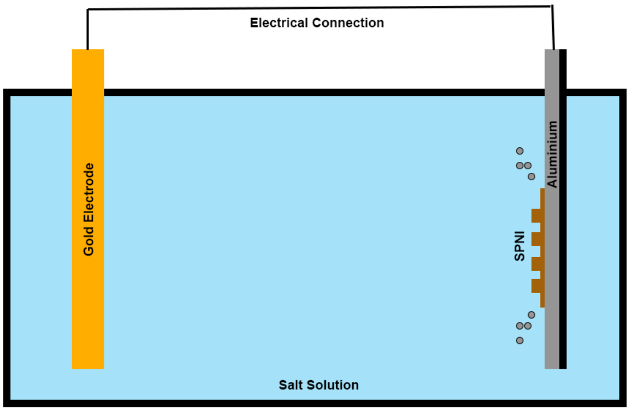

Figure 3.7: Galvanic dissolution setup.

Aluminium and Electrolytic Dissolution

A thin film of aluminium is evaporated onto a fresh silicon wafer. This is done using a similar method as for gold below.

Upon completion of the SPNIs at time of release the entire wafer is submerged in 500ml of 2M sodium chloride salt solution (i.e. a 4 mol dm^{-3} solution) at 20 °C. A large gold counter electrode (evaporated onto the same size of wafer as the samples) is also submerged and positioned so that there is no direct electrical contact in the solution with the sample wafer. Both samples protrude above the waterline so that crocodile clips can be attached and were separated by a few centimeters. One clip is attached to the bare gold counter electrode and the other on an exposed section of the aluminium on the sample wafer. The crocodile clips are electrically connected together, as seen in figure 3.7.

The two metals (gold and aluminium) have different potentials and so a current flows from one to the other. This causes the plates to polarise in solution. Ions from the aluminium are released into solution, causing the aluminium layer to dissolve over a few days [51].

The SPNIs are then gathered and soaked in hot water to remove any excess salt. This method produces none of the shrinkage seen in PMMA derived samples and does not have such a tight time imperative.

Preferred Sacrificial Methods

The devices used in the main body of this thesis were all prepared using the aluminium sacrificial layer. The aluminium method yielded a much higher success rate for releasing SPNI samples. They were higher quality, with fewer defects and many more were viable from each wafer. For the first three batches the harvest of aluminium based devices yielded 100% as apposed to a 60% success rate with PMMA based devices.

Along with the increased failure rate of the PMMA process, it also has the downside of causing the SPNIs to shrink during the final bake. During the final bake, temperatures exceed the glass transition temperature of the PMMA, causing the sacrificial layer to become a viscous liquid that allows the PI to shrink during baking.

The shrinkage of the SPNIs was measured after release for both PMMA and aluminium sacrificial layers. The PMMA resulted in an average shrinkage of 4.2% across the device ($n = 9$, $\sigma = 0.02$) and the aluminium sacrificial layer provided only 0.5% shrinkage ($n = 5$, $\sigma = 0.03$).

The shrinkage observed using the PMMA negatively affected device assembly, as key dimensions (such as those used to bond the SPNI to the interface PCB) were shrunk enough to prevent proper alignment between channels. Therefore the aluminium method was preferred due to its greater yield and lack of shrinkage.

Table 3.3: Spinning profile settings for thick layer of PI.

Step	Time (seconds)	rpm
1	10	500
2	20	3000
3	10	700

3.3.2 Polyimide Substrate

The first layer for the substrate of the device, and the encapsulation layer to embed and isolate the gold interconnects, are layers made of polyimide. The substrate layer is a 18 μm layer spun at 3000 rpm for 20 seconds consisting of the thicker of the two polyimides used (Durimide 7020, Fuji Film), the full spin profile see Table 3.3. A soft bake is then preformed using a slow 3 °C per minute temperature ramp starting at 20 °C to 90 °C where it is held and baked for 8 minutes. The sample is allowed to cool for 20 minutes before moving onto photopatterning.

The wafer is then exposed to a 365 nm wavelength (i-line) ultraviolet light through a negative mask for a light integral of 16 seconds, the masks used for each layer can be seen in figure 3.8. A bake for 3 minutes at 90 °C is preformed followed by a 10 minute cooling period.

The sample is then developed by submerging in HTRD2 (Fuji Film) and RER600 (Fuji Film), supplemented by using wash bottles of the substances to apply directly to intricate areas of the device. This disolved PI in the exposed regions to leave the outline and base of the devices intact.

Exactly the same process applies when adding the encapsulation layer on top of the developed gold pattern. The exception being that Durmide 7505 from FujiFilm is used to make a 5 μm film by spinning for 30 seconds at 3800 rpm. Durimide 7505 is thinner in consistency than Durimide 7020 and therefore can be used to spin thinner films. All other elements of the process are identical.

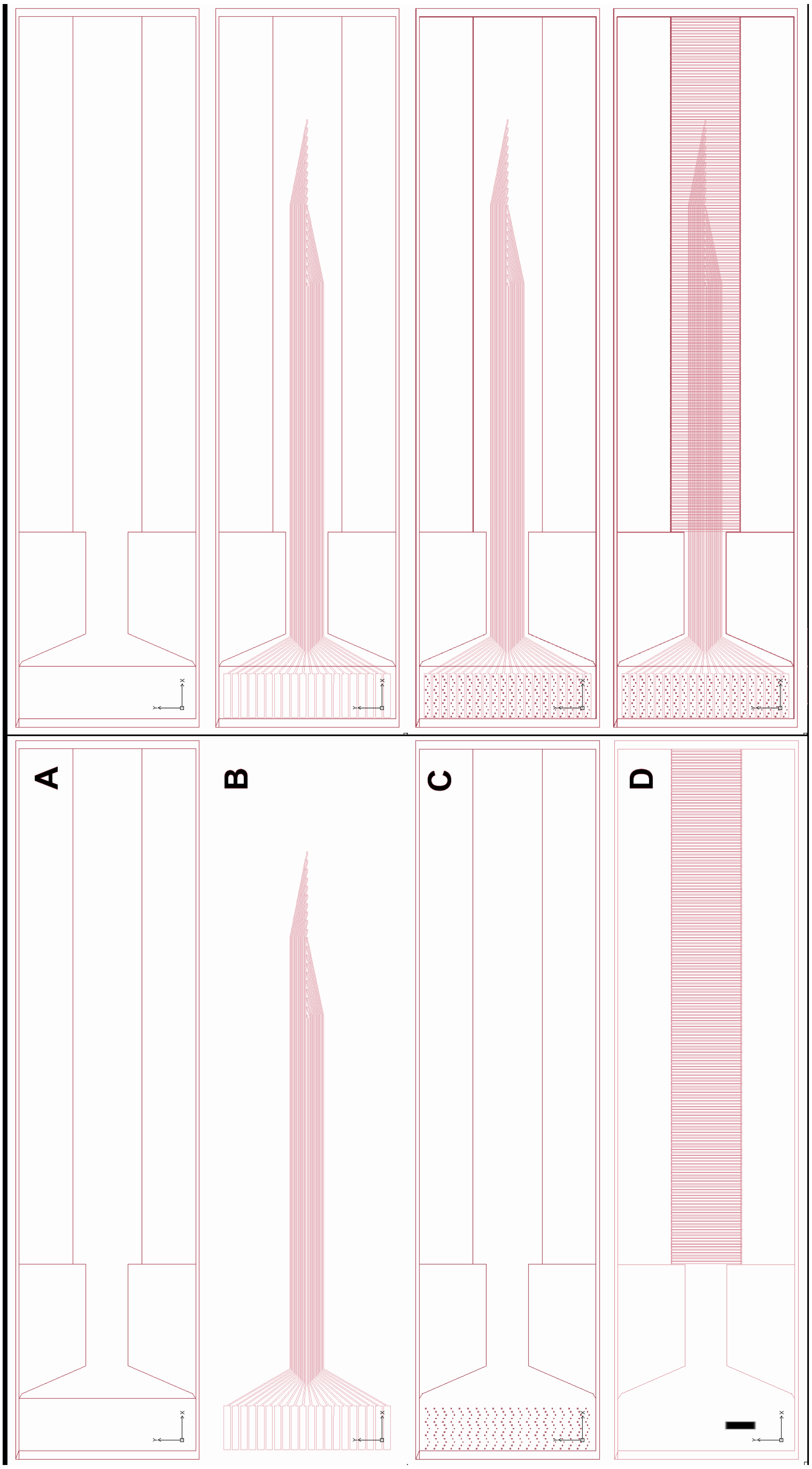

Figure 3.8: Examples of the masks used for the different layers of a single device, on the left shows the individual layer with on the right showing the addition of subsequent layers. A. is the substrate PI layer, B. the metalization mask, C. the encapsulation layer, defining the electrode sites, the device shape and connection regions, D. shows the channel layer. Scale bar is 1.8 mm.

Table 3.4: Spinning profile settings for SPR220 photoresist

Step	Time (seconds)	rpm
1	10	750
2	18	2800
3	1	500

3.3.3 Metalization

In between the substrate and encapsulation layers a gold, electrode layer is added. This process is achieved by thermal evaporation of gold on to the surface of the developed PI.

The wafer with the substrate layer already developed is placed in a vacuum chamber (308R Coating System, Cresington) and pumped down to 1×10^{-6} bar. Once the chamber is at pressure, the surface of the sample is cleaned with a weak oxygen plasma for 30 seconds (40 μm current draw). Before the sample is coated the crucible holding the gold is outgassed allowing the chamber pressure to be pumped even lower. This is done by gradually increasing the source by approximately 1V per minute until the gold melts, the crucible is then allowed to cool with a ramp down of 1V per minute to avoid cracking of the crucible. The chamber is then left to pump down to a stable pressure.

To improve the adhesion of the gold to the PI surface a 15 nm thick layer of chrome is sputtered directly on the PI. This is done using a sputter source (308R 100W Sputte Supply, Cressington) drawing 80 mA for 30 seconds.

The small crucible filled with gold is then heated by passing a 25 A current through the crucible for 3 minutes (using a 308R Evaporation Supply LT1500, Cresington). Ramp up and ramp down protocols were also enforced to prevent excessive cracking of the crucible. This resulted in a 100 nm thick gold layer covering the entire surface of the sample as measured by a thickness monitor (mtm 10, Cresington).

In order to define the electrodes and their feed lines the sample once again under goes photolithography. The surface is spin coated with SPR-220-7 (MicroChem), a positive resist, and exposed through a mask for 35 seconds followed by a 25 second resting period, this 35/25 second exposure/rest is then repeated a further three times. This is done to ensure the light penetrated the 8 μm thick resist but did not have any adverse reactions to surrounding regions. The programmed spin profile can be seen in Table 3.4.

After the exposure the sample is set aside for 5 minutes for any reactions caused by the UV exposure to complete. To develop the resist it is submerged in a petri dish filled with MF-26A (Shipley). The dish is continuously agitated for 2 minutes and then rinsed with more MF-26A. This process is completed two or three more times, until no pink streaks could be seen running off the sample when lifted from the dish. After another rinse in MF-26A, the sample is placed in a small amount of fresh MF-26A (which is clear and colourless) and soaked for a further minute. This step is preformed to ensure the complete development of the resist, if the resist is not completely removed after the minute in the solvent, it would take on a pink hue, and the sample would need to be developed again.

The resist now only covered parts of the wafer where metal is desired to remain. To remove the exposed and unwanted gold and chrome a wet etch for each is required. The gold is removed by a 40 second etch in gold etch solution (Chestech), the sample is then washed in RO water to prevent the gold and chrome etchants interacting. The sample is then submerged in chrome etchant (Aldrich) for 15 seconds and again submerged in water to clean off any excess chemicals and dried with nitrogen.

The remainder of the resist is then removed using acetone which is sequentially rinsed off with IPA and dried with nitrogen. The resist (SPR-220-7) is a complex organic compound and may leave residues even after washing with acetone. Due to this the sample is then cleaned in a 70 W oxygen plasma at 3 bar to remove any surface grime and treated with UV O-zone to react with any remaining organic residues, making them soluble in acetone which is used for a quick rinse and washed off with IPA. This process left the devices with defined gold electrodes and their feed lines on top of the base PI substrate.

3.3.4 Encapsulation and Channel Definition

Encapsulation of the gold layer is required, so that all the gold lines are always isolated from each other [31]. This is done by applying the process as with the previous PI layer, however this time the PI is only 5 μm thick, with a spin profile as in Table 3.5. The photolithography exposed small windows at the end of each gold line, cutting into the PI to create the gold electrode tips. The rest of the gold remained encapsulated.

The channel layer is spun next which requires a thick 100 μm layer to be spun, the spin profile for which is shown in Table 3.6. PI (7020) is span at 330 rpm for 30 seconds to achieve this thickness [31]. This is then baked at a slow ramp of 0.5 °C per minute up to 90 °C where it is held for 30 minutes. Throughout the baking process the sample is closely observed to detect any signs of bubble formation. If any initial signs of bubble formation was observed the heat ramp was paused and kept at its current temperature for 5-10 minutes. Around 60% of the samples that made it this far failed during this soft bake.

When the bake is complete and the sample had cooled for 20 minutes, photolithography took place on the sample. The thickness is at the tolerance for the Cannon's ability to load so manual loading sometimes had to be employed which lead to slight alignment issues.

The sample is exposed for 35 seconds and developed in HTR-D2 and RER200 as before, however this process takes a lot longer as the amount of material to remove is significantly more. When using a PMMA sacrificial layer it is possible that the time required to develop the channels is greater than the time required to dissolve the sacrificial layer which triggers a premature release. When using an aluminium sacrificial layer there is no danger of this. Frequent washes with the two developers is also required to ensure that sufficient material from the groves in the channels is removed.

The sample undergoes a hard bake to remove all remaining solvent from the SPNIs and fixing them into their final configuration. A dual step bake is used to give the convection oven enough time to achieve an oxygen free environment, this is achieved by baking in a

Table 3.5: The spin profile of the thin PI layer.

Step	Time (seconds)	rpm
1	5	500
2	30	3800
3	1	300

Table 3.6: The spin profile of the PI channel layer.

Step	Time (seconds)	rpm
1	60	200
2	60	330

nitrogen atmosphere. This is necessary as the PI burns if in an oxygen atmosphere above 200 °C. Due to this the oven is programmed on a ramp of 3.5 °C per minute up to 200 °C where it rested for 30 minutes and then increased at 3.5 °C per minute to 300 °C where it rested for an hour before cooling down at about 1 °C per minute.

By the end of this process the SPNI is functionally complete with substrate, gold, encapsulation and channels layers all in place and fully developed.

3.3.5 Release and Final Assembly

The next stage is to release the samples and to assemble them into devices that can be tested using conventional electronic systems.

The eight devices per wafer are released either by soaking in MIBK over 19 hours or by placing in a 2M salt solution with gold counter electrode depending whether the sacrificial material is PMMA or aluminium as described in a Section 3.3.1. After this the devices were throughly inspected, classified by quality and labeled. Ideally the next steps would be rolling followed by mounting and ball bonding. However, during this experiment a baseline measurement was required of a non-rolled device, so mounting and bonding was conducted first.

Interface PCBs were made so that the SPNIs could be bonded directly to them, the layout and specifications can be seen in figure 3.9 and Table 3.7. The gold coating is added to make ball bonding to the surface as easy as possible.

The individual SPNIs were aligned over a PCB under a microscope and fixed in place with a small amount of acrylic based adhesive and left to dry. Once dry the sample complex is placed on the ball bonder and ball joints added between exposed regions of the device as shown in figure 3.10. The bonds rivet the SPNI in place by bonding through the holes in the SPNI onto the surface of the PCB contacts. Because there is a compression of the SPNI over exposed gold regions this makes a very good electrical contact.

After the SPNIs have been bonded to their PCBs they are ready for initial testing. After test data had been gathered, rolling was required. Rolling of the SPNI is the final stage in which the 2D structure gains its 3D characteristic spiral shape. A custom made roller is used for this process whereby the device is held between rotating tweezers and gently coiled. Once the main body of the SPNI has been coiled up to the neck of the device, a holding sheath of silicone tubing was added around the device to prevent it uncurling. Silicone can be smeared around the tubing joint to keep it in place if necessary.

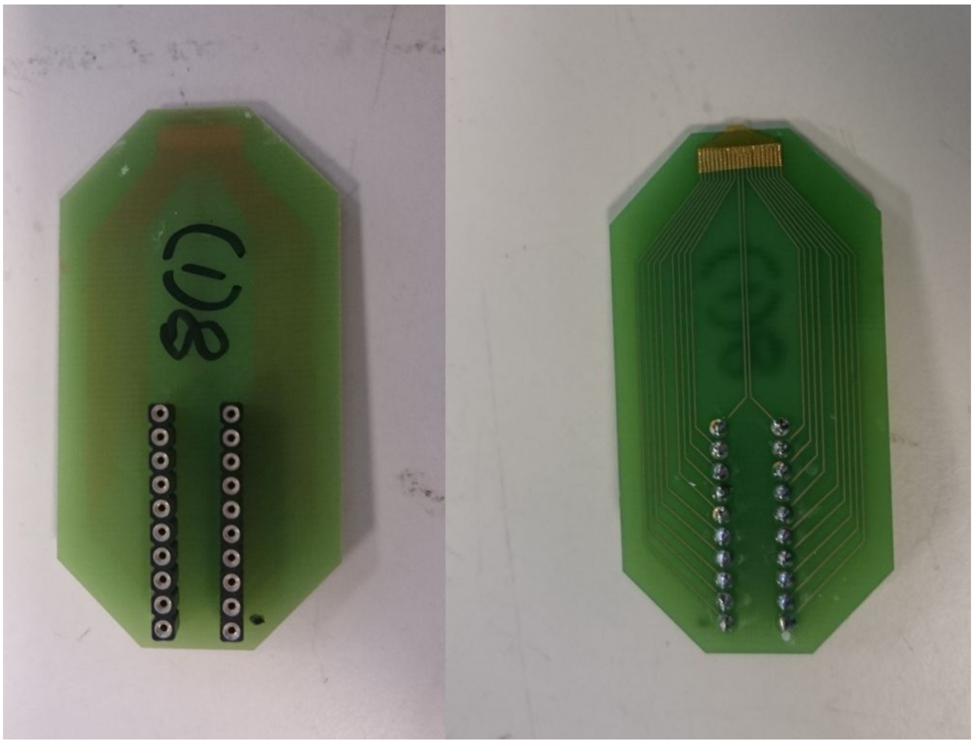

Figure 3.9: Custom ordered interface PCBs, the SPNI is directly bonded to the exposed contacts at the top of the right image. The impedance analyser test pins could then be inserted into the SIL connectors.

Table 3.7: Technical specifications of custom PCB for interfacing the SPNI.

Board thickness:	1.6 mm
Material type:	FR4
Copper weight:	1 oz
Surface finish:	Nickel/Gold

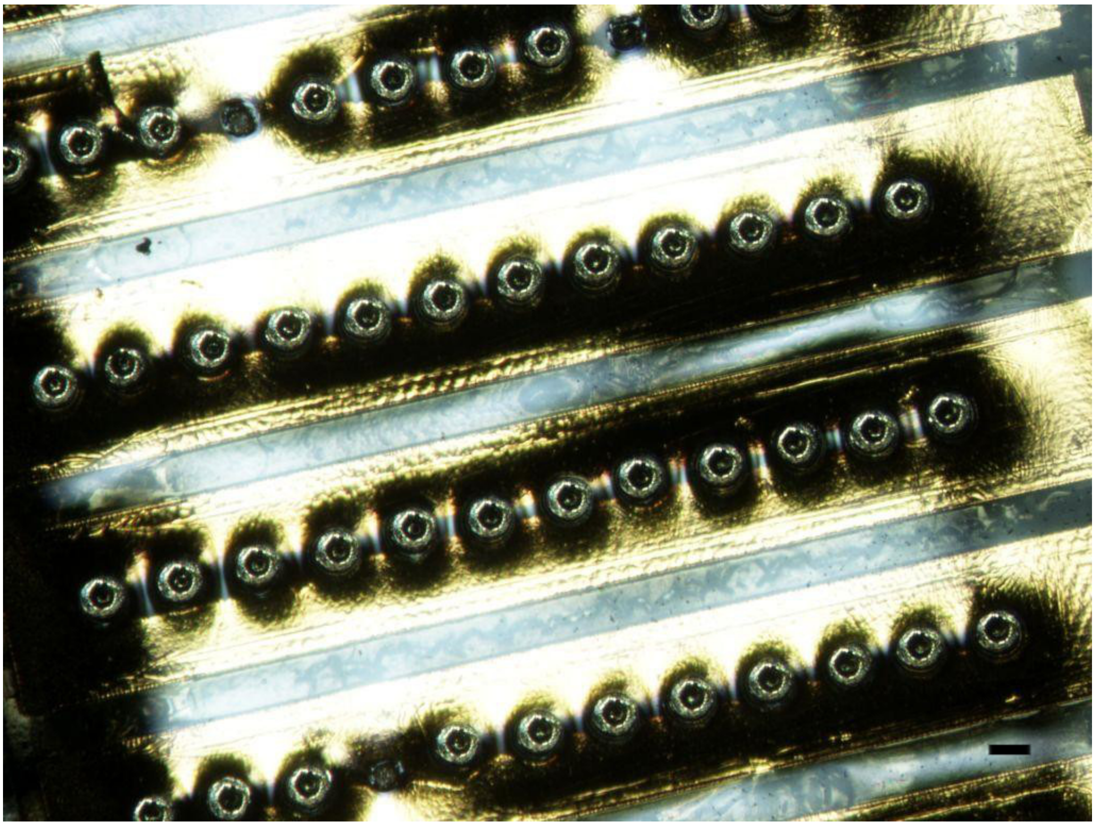

Figure 3.10: Rows of ball bonds acting as micro-rivets holding the SPNI to the PCB and making good electrical contact between the two. Scale bar is 60 μm.

3.3.6 Sealing

This completes the basic SPNI and it is ready for testing. If the device were to be sealed, this would be done immediately before rolling, the process for this is outlined further in chapter 6.

Briefly: sealing is achieved using a 10:1 two part PDMS silicone to cross-linker mixture that is spun at 500 rpm for 30 seconds and 1000 rpm for 1 minute on top of a PMMA layer. The wafer is then soft baked or left on the bench top until cured. The 20 μm thick PDMS sheet is released from the PMMA by submersion in IPA which lifts the PDMS from the PMMA surface. The PMMA layer on the wafer can then be used for subsequent PDMS layers.

In order to physically manipulate the PDMS, it is floated on IPA and maneuvered into position over the SPNI, the IPA will then evaporate, mating it to the top of the SPNI channels. The PDMS film is then cut to size over the SPNI.

3.4 Impedance Spectroscopy

In order to record neural activity, ionic currents have to be transduced into electronic signals. Therefore in order to characterise an electrodes ability to do this, electrochemical impedance spectroscopy (EIS) can be used. EIS measures the electrical impedance and phase angle of an electrode when exited by a sinusoidal waveform. In this work a sinusoidal excitation of 5 mV was applied across 40 Hz to 1 MHz [31] [52].

Impedance spectroscopy can give much information about the performance of an electrode, although biological signals generally fall below 10 kHz, higher frequency information can give the capacitive properties of an electrode. Use of impedance spectroscopy is common in neural interface testing and can be used for quality control as well as experimental research.

The tests preformed in this work were two terminal measurements using a network analyzer (HP 9424, Hewlett Packard), driven by custom software (LabView). The device

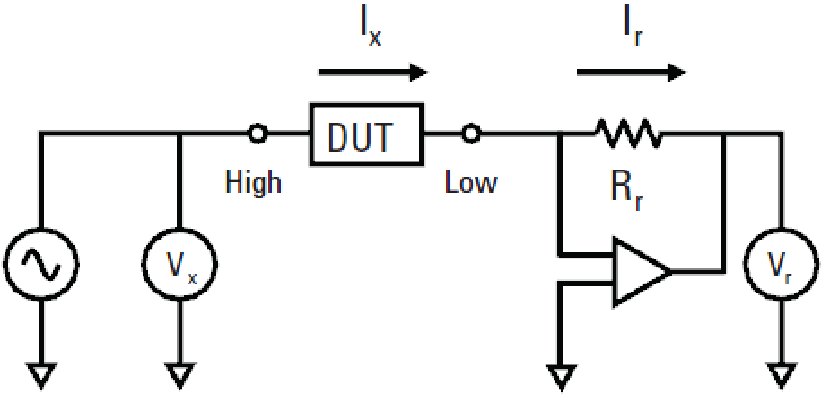

Figure 3.11: A depiction of an auto-balanced bridge, the DUT shares current with R_r which is clamped by an amplifier, thus allowing for an impedance measurement from two voltage measurements. This allows for highly accurate impedance measurements, however, error can increase when measuring very large impedances.

under test (DUT) and a platinum counter electrode which has very low impedance were submerged in Benedict's solution, which is made up to simulate fluids in the human body.

The impedance analyser uses an auto-balancing bridge method to acquire impedance measurements, the principle of which can be seen in figure 3.11. In this method the test current flows though both the DUT and a range resistor. An IV converter amplifier clamps the LOW voltage to a zero potential and gives an output voltage that is proportional to the current that it has to provide to maintain the voltage clamp. This can then be combined with the input voltage measurement to calculate the impedance, as in equation 3.1.

$$Z_x = \frac{V_x}{I_x} = R_r \frac{V_x}{V_r} \tag{3.1}$$

Where R_r is set and known.

This chapter has outlined the methods by which the SPNI is fabricated along with methods of testing. The next section will go on to describe the mechanical structure of the SPNI and how understanding of this has been tested and developed.

CHAPTER 4

STRESSES IN A THIN FILM LAMINATE

In the previous section the methods by which the SPNI is fabricated are outlined. In this section a redesign of the device is discussed so that an insulation layer can be included in order to prevent inter-channel cross-talk. This redesign raises issues relating to the internal stresses of the device, particularly pertaining to the gold layer.

Previous studies have described this structure and the stress requirements of the gold layer [31, 48]. These theories are explored and tested with bending experiments designed to test if the gold is as susceptible to internal stresses as has previously been thought.

4.1 Redesigning the SPNI

The main issue preventing the SPNI from moving forward to further trials is the inter-channel current leakage previously described in chapter 2. In order to prevent this leakage a thin film of PDMS is included within the structure of the SPNI to seal the channels, increasing the inter-channel resistance and reducing inter-channel cross-talk. Further explanations and experiments on this can be seen later in chapter 6.

The initial design of the SPNI entailed rolling the device so that the channels are all pointing inward, toward the center of the spiral, as can be seen in figure 4.1. However, a PDMS layer needs to be included on top of the channels, if it is to be an effective insulator. In this configuration it is feared that as the SPNI is rolled, the PDMS layer would deform

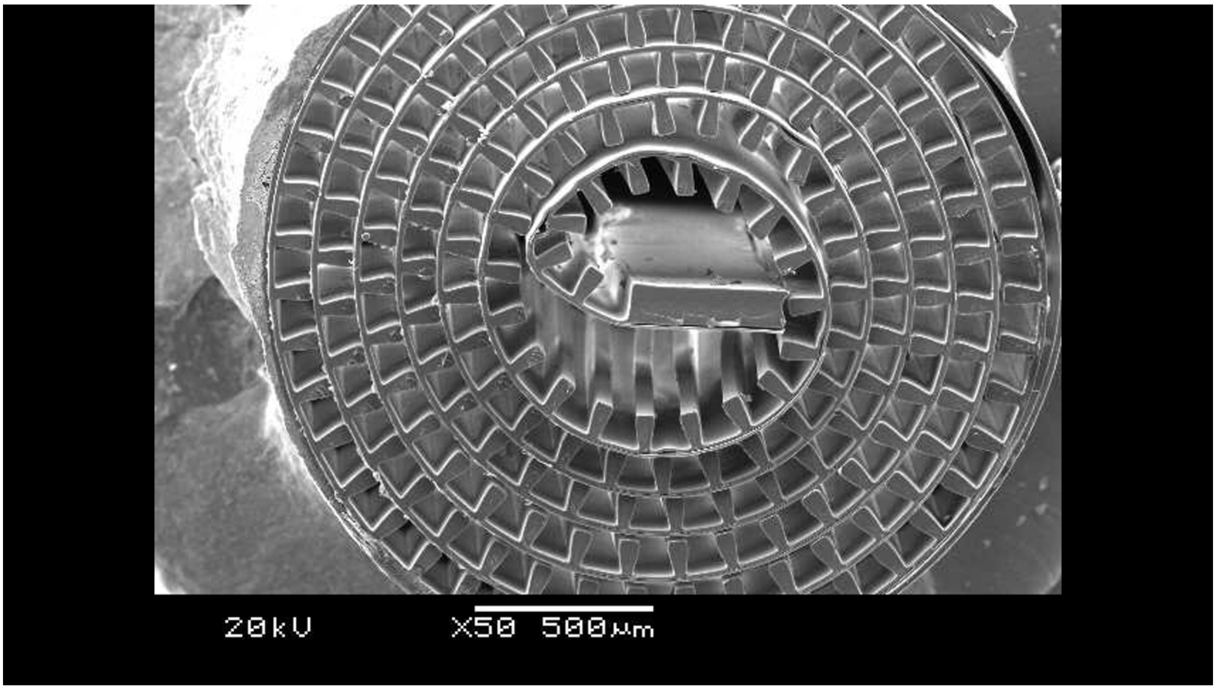

Figure 4.1: Taken from [31], an SEM of the SPNI showing how the original design included channels that all face inward toward the center of the spiral.

unhelpfully by either sagging into channels and reducing the neural transparency of the device or by creating pockets of folded PDMS, though which the leakage current could still flow or in other ways interfere with the structure of the SPNI.

However, if the SPNI is rolled in the opposite direction, so that the channels point outward, divergent from the center of the spiral, then as the device is rolled the PDMS would be pulled taught across the top of the channels, a process which could aid in the integrity of the formed seal, as demonstrated in figure 4.2.

The new orientation of rolling however changes the internal stress structure of the SPNI. A structure that has previously been designed to provide minimum stress on the gold layer. In order to change the orientation of the rolling process, it is first necessary to investigate how the internal stresses of the SPNI affect the gold layer. Due to confusion in previously reported internal stress profiles of the SPNI [31], an experiment is required to investigate how delicate the gold actually is in the SPNI and if a redesign of the layered structure is required when rolling the SPNI country to initial designs.

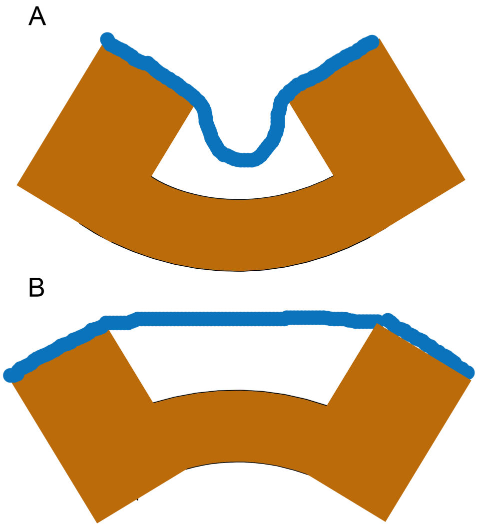

Figure 4.2: Demonstrates the issues with the original design in A, B shows the intention for the SPNI redesign, to pull the silicone seal tort over the top of the channels.

4.2 Stresses within the SPNI

Thin film metals are brittle and have low tensile strengths when compared to the polymers commonly found in neural interfaces. The Young's modulus of thin film gold is around 47-61GPa and the ultimate tensile strength is between 257 and 477MPa for films approximately 200μm thick [53]. When compared to the Young's modulus of 2.5GPa and ultimate tensile strength of 215MPa for polyimide [54], it can be seen that the polyimide substrate of the SPNI can withstand significantly larger strains than that of its gold interconnections. Due to the significantly lower Young's modulus of PI the same strain on a PI film will produce much less stress than when applied to a gold film.

Free standing thin film gold is brittle and can easily break when subjected to strains commonly found within neural interfaces. This is also true of many other metal films [55]. It is therefore common to design a neural interface with any metalization layer located near the stress neutral plane of the device, thus minimising the effect of device deformation on the stresses in the metalized layer.

In order to calculate the strain exerted on the gold layer, elastic bending theory is applied to the SPNI. This assumes that the structure of the SPNI is linearly elastic within the stresses applied, that the modulus of elasticity is the same when the beam is under compression as it is when it is in tension and finally that the SPNI is homogeneously flexible in the direction of bending.

We consider the SPNI being rolled as being analogous to a homogeneous beam being bent. As the beam bends the top of the beam becomes subject to extension stresses as the bottom of the beam experiences compressive forces. This is shown in figure 4.3 where A'B' is greater than AB and C'D' is smaller than CD.

If a profile is taken through a section of the beam, it would show that the stresses vary within the structure with a maximum applied force being seen at the top and bottom. Running throughout the middle of the structure however would be a plane where the compressive and tensive forces acting on the beam cancel out, figure 4.3C. This is the stress neutral plane and the forces experienced on this plane are zero, regardless of the forces placed on the structure as a whole, given that structural integrity of the layers is maintained.

Although the SPNI is not a homogeneous beam, the same principle applies and within the SPNI is a stress neutral plane.

It is common practice with the design of neural interfaces to place metallic conductors within the neutral plane, or as close to it as fabrication limitations allow. The rational behind this is that due to the fragility of the thin film metal, if it is placed in the neutral plane it will not experience forces caused by deformation of the device and thus will be less likely to fracture.

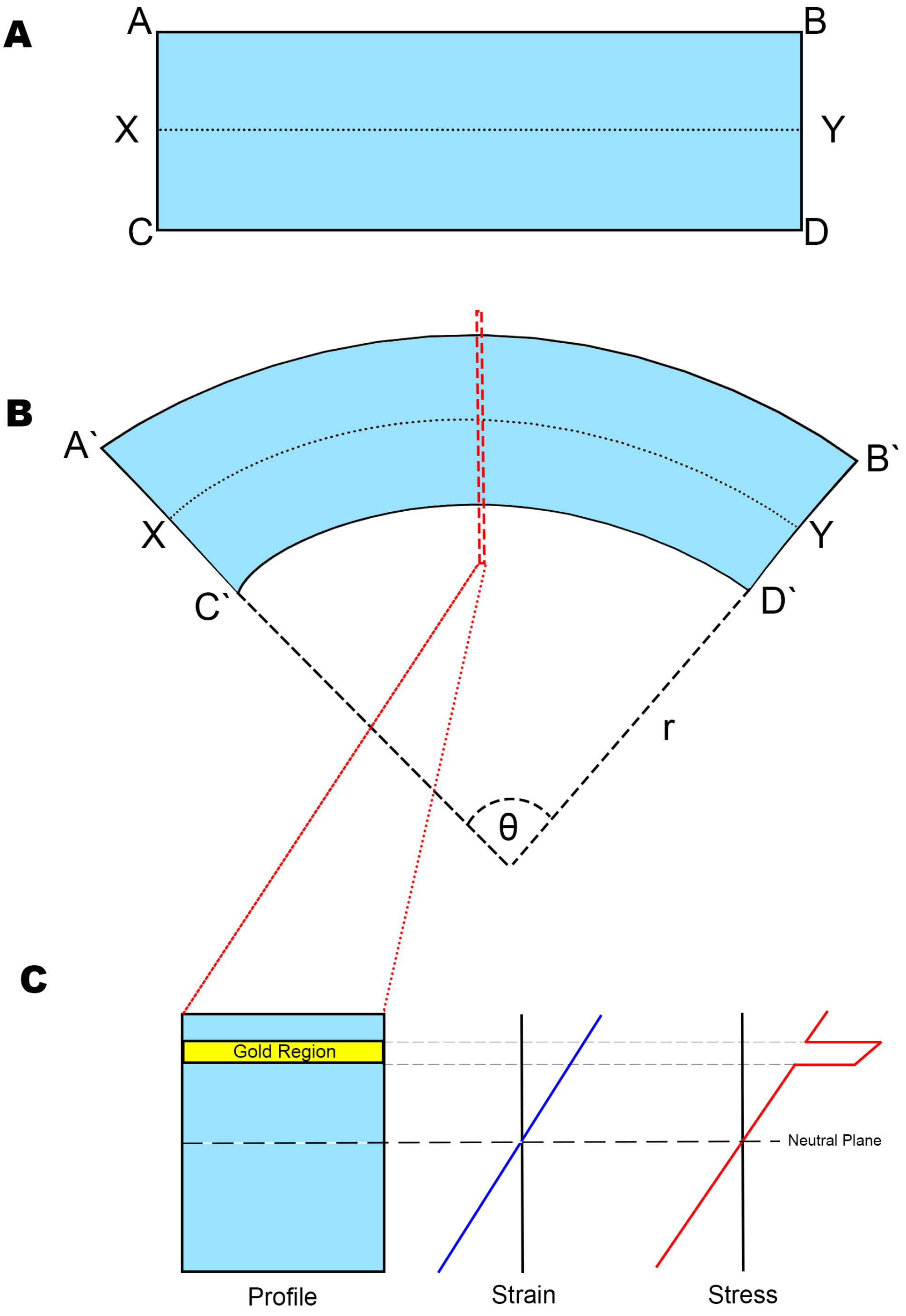

Figure 4.3: Beam (A) ABCD is bent into A'B'C'D' (B), however due to the tension and compression canceling out at the center of the beam, XY remains the same length. (C) shows a section taken through the bent device with an asymmetrical gold plane that is outside the neutral plane, this is shown next to the strain and stresses experienced by the structure going though the profile in blue and red respectively. As can be seen due to the change in Young's modulus in the gold, the same amount of strain results in a much larger magnitude of stress.

4.2.1 Stress Analysis of a Simple Beam

If there is an unbent beam with corner points denoted as A,B,C and D as in figure 4.3A, with a plane cutting through its mid-point as the line XY. This beam can be bent as in 4.3B, where θ is the polar angle and r is the radius of curvature.

If we compare arc lengths of the structure it can be seen that AB has to extend in order to become A'B' and CD has to compress to become C'D'. The length of the XY plane however is unchanged as in the middle of the beam the extension and compression of the beam cancel out. Expressing this in terms of the arc length yields equation 4.1.

$$X'Y' = XY = (r + y_{neut})\theta \tag{4.1}$$

Where y_{neut} is the distance from the bottom surface CD (i.e. the reference place) to the neutral plane. Also in arc notation yields equations 4.2 and 4.3.

$$C'D' = r\theta \tag{4.2}$$

$$A'B' = (r + t)\theta \tag{4.3}$$

Where t is the thickness of the beam.

The strain at any point y meters into the device can be calculated as equation 4.4.

$$\epsilon = \frac{\Delta L}{L} = \frac{\Delta L}{XY} = \frac{(r + y)\theta - XY}{XY} \tag{4.4}$$

Where XY is the length of the neutral plane in a given section, r is the radius of curvature and θ is the polar angle between the two ends of the section, ΔL is the change in length of the beam at the plane y meters into the structure and L is the original length of the the beam. Recalling the XY plane is the same length before and after bending.

By replacing all lengths with arc lengths and simplifying gives equation 4.5.

$$\epsilon = \frac{y - y_{neut}}{r + y_{neut}} \tag{4.5}$$

Where y_{neut} is the distance from the reference plane CD to the neutral plane.

As the neutral plane always falls in the middle of a simple beam structure this becomes equations 4.6.

$$\epsilon = \frac{y - \frac{t}{2}}{r + \frac{t}{2}} \tag{4.6}$$

Where t is the thickness of the beam; or in the case of the SPNI, the unchanneled section.

This result is an extension of the analysis shown in [31] and means that with a known thickness of beam and a known radius of curvature, the strain (ϵ) throughout the device can be calculated. Using this principle an experiment is designed and will be laid out later in this chapter.

It is logical to assume that the thicker sections of the structure do not bend as much as the thinner sections. Due to this assumption, it is likely that the majority of the strain is localised between the channel walls over the thinner sections of the device. This effect can be seen in figure 4.1.

If we assume a beam of 25.1 μm thickness (25 μm for the polyimide and 100nm for the gold) to represent a non-channeled section of the SPNI and that Young's modulus of thin film gold is used, the effective stress on a gold layer if it were located at any point throughout the device can be calculated. The stress and strain profile extracted can be seen in figure 4.4, which shows the zone of acceptable strains to be between approximately 11.3 and 13.8 μm into the device.

This assumes that the channel walls are acting as stationary points; a fair assumption, as the channeled sections are five times thicker than the interconnecting sections. Meaning they will be five times more resistant to movement than the non-channeled sections. Thus

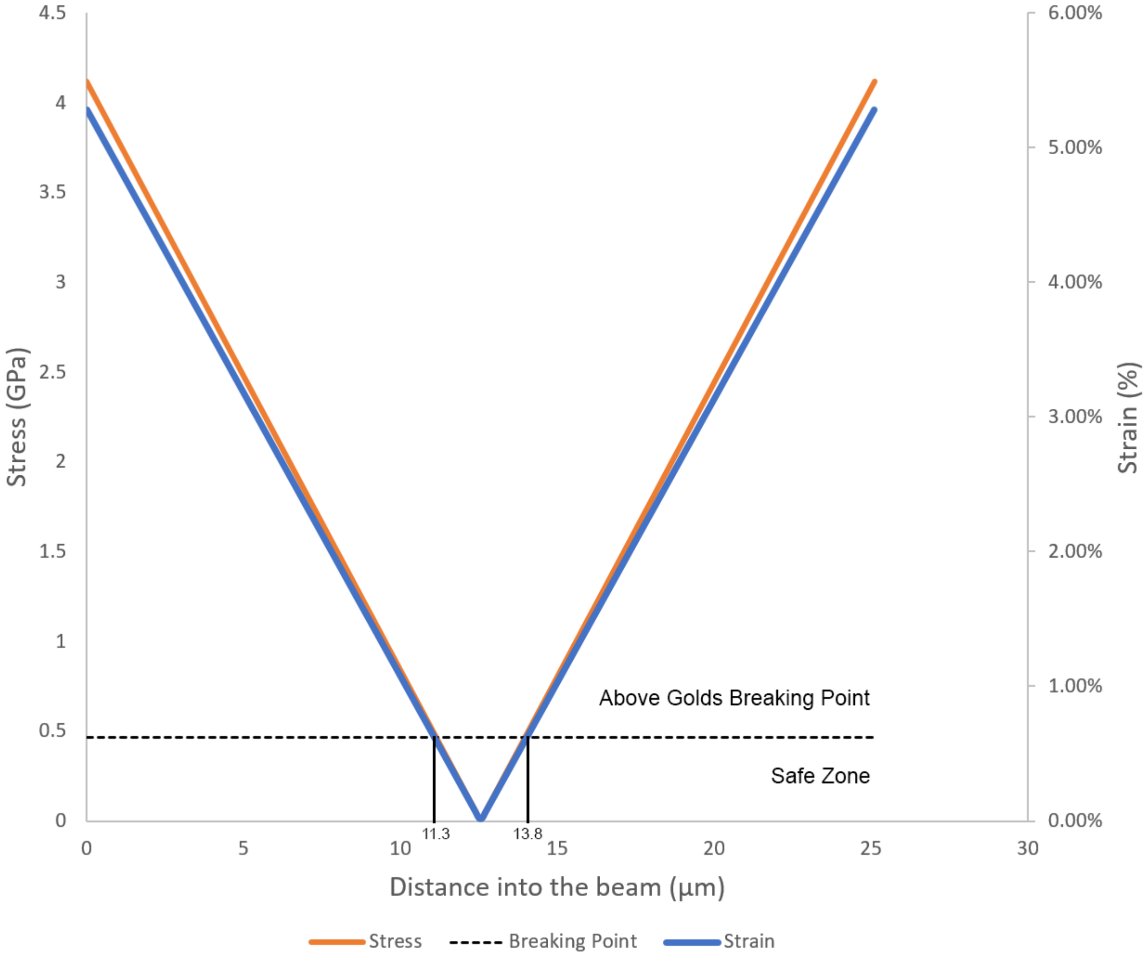

Figure 4.4: A graph of the theoretical stress and strain experienced by a gold layer placed a number of μm through the device. The dotted line shows the ultimate tensile strength of gold, all values above the line should break free-standing gold films. The safe zone is between 11.3 μm and 13.8 μm into the device.

we can assume that they are pseudo-stationary points, as this will give us the worst case analysis for the non-channeled regions.

If this line of thought is applied to the SPNI's current structure, a stress profile as can be seen in figure 4.5 is generated. This shows that in the current configuration (orange) the gold has a stress acting on it of around 1.2 GPa. This is much higher than the ultimate tensile strength of thin film gold which is around 477 MPa at best [53]. If the structure were to be updated to the proposed rolling configuration this stress would remain the same due to the symmetrical nature of the stress profile.

This analysis cannot therefore explain the stresses on the gold and arc-analysis of the initial design should therefore be considered as the gold should not be able to withstand these applied stresses. However, previous experiments with the SPNI in this design have functioned well, without breaks of continuity in the gold layer. This requires an investigation to gain better understanding of the stresses acting within the SPNI's internal mechanical structure.

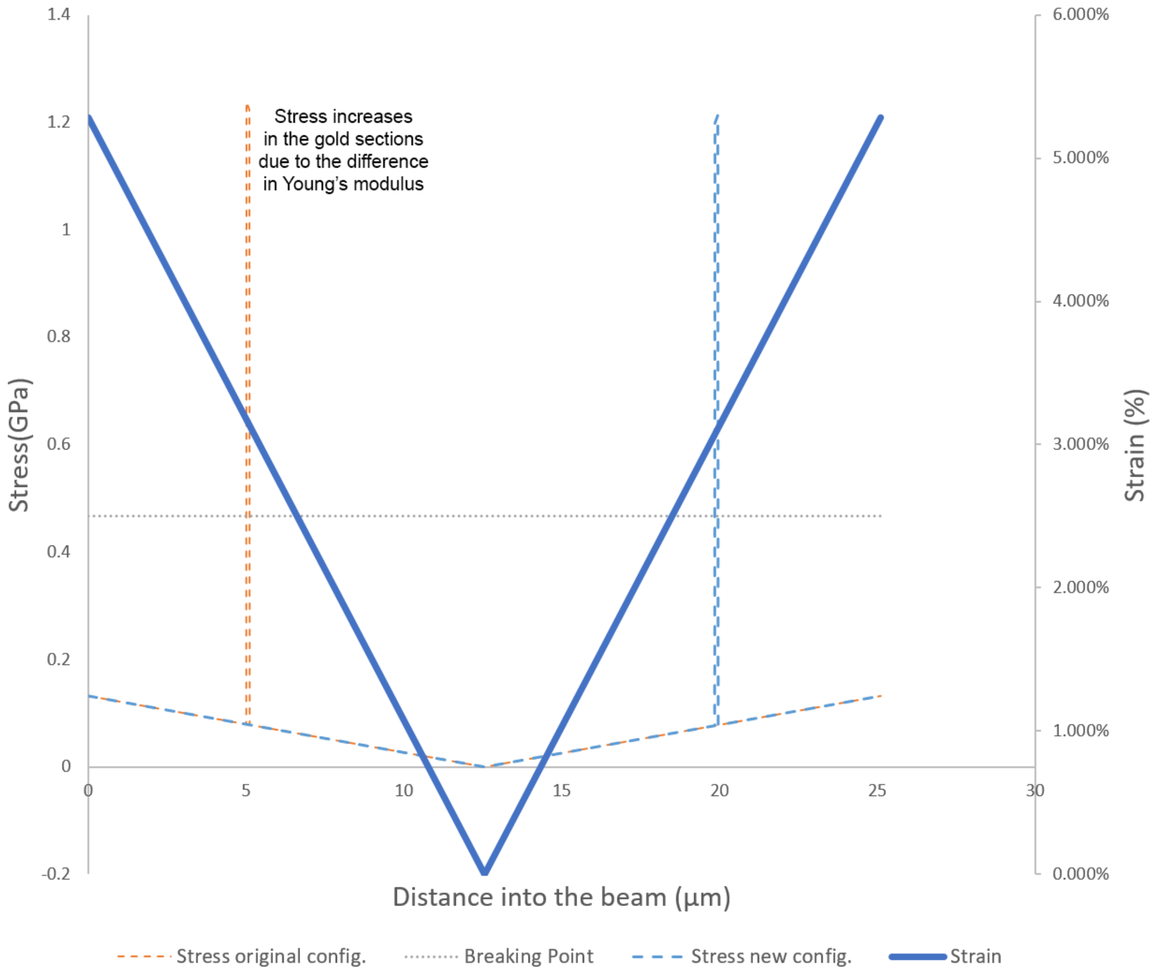

Figure 4.5: A graph showing the stress and strain running through the SPNI taking into account the different material properties of PI and gold. The stress through the gold sections can be seen to dramatically increase when compared to the PI with the same strain due to its much higher Young's modulus. The old and new configuration stresses are shown which are the same with the exception that the original device had its gold layer in compression, whereas the new configuration would have the gold in tension.

4.2.2 Experimental Rational

Another method of modelling the position of the neutral plane of the SPNI is using the parallel axes method. The centroid of each area making up the structure, N_i, is calculated relative to a reference axis. The distance from this reference axis to the centroid is then multiplied by the area of that section, A_i. The distance to the neutral plane is then defined as the sum of this contribution of each section divided by the total area of the structure, ΣA_i, which is given by equation 4.7.

$$y_{neutral} = \frac{\Sigma N_i A_i}{\Sigma A_i} \tag{4.7}$$

For a rectangle this process is simple, the centroid is found at the mid-point of the structure and the area is found by multiplying the rectangles height and width (figure 4.6). Thus if considering the unchanneled region of the SPNI is $(h_p + h_s)$ thick. This would give a neutral plane as shown in equation 4.8.

$$y_{neutral} = \frac{\frac{h}{2}(h_s + L) + (h_s + \frac{h_p}{2})(h + pL)}{(h_s + h_p)L} = \frac{h_s + h_p}{2} \tag{4.8}$$

Where h_s and h_p are the height of the substrate and passivation layer respectively and L is the length between channels. The metal layer is omitted from this equation for simplicity as it is much less than 1% of the overall structure and will not have much of an effect on the result. Similar assumptions are commonly used [56].

This shows the neutral plane for a rectangular profile is found in the middle of its total thickness, which is the same as the previous analysis. These analyses, however, are in direct contradiction to the analysis that lead to the original design of the SPNI which placed the gold layer 10 μm away from this calculated neutral plane. This design however should put the layer under considerable tensile strain, easily enough strain to break free standing thin film gold.

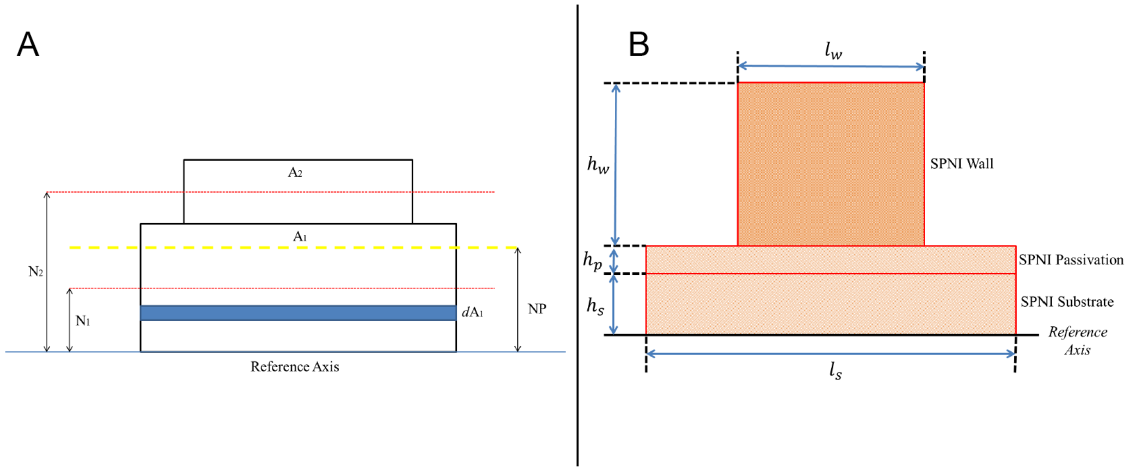

Figure 4.6: A cross section through the composite structure of the SPNI. Where l_w is the width of a channel spacing, h_w is the height of a channel, h_p is the thickness of the passivation layer, h_s is the thickness of the substrate PI layer and l_s is the length of a section. The diagram on the left shows the parallel axis method where A_2 is the area of the channel, A_1 is the total area of the substrate and passivation layer, N_1 is the centroid of A_1 and N_2 is the centroid of A_2 and NP is the height of the neutral plane from the reference axis if it is assumed that the channels are complicit in the bending event.

4.2.3 SPNI Original Stress Design

In the original analysis [48] beam theory was misapplied [31] as it was assumed that the SPNI could be modeled as a T-beam section as can be seen in figure 4.7. However, this paradigm leads to the use of an incorrect bending axis and invalidates the result.

The analysis found in [48] of the SPNI when bent gives a neutral axis as shown in equation 4.9.

$$y_{neutral} = \frac{pbh + 0.5pb^2 + 0.5sb^2}{pb + sh} \tag{4.9}$$

Where $y_{neutral}$ is the location of the neutral plane into the device and p,b,h,s and w are the channel pitch, substrate thickness, channel height, channel spacing and channel width respectively.

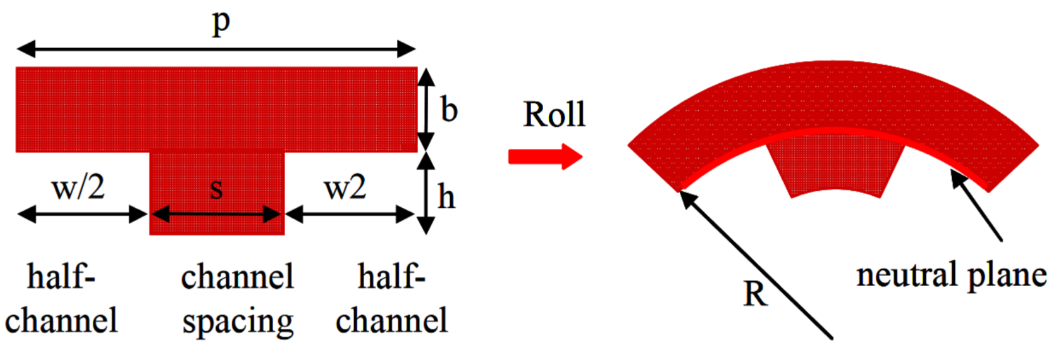

Figure 4.7: Taken from [48], shows the previous model of bending in the SPNI, however the plane of bending in the model is incorrectly shown by the original authors in this diagram. Where w, s, w2, p, b, h and R are the channel trough width, the channel spacing, half of the channel trough width (mistakenly shown in place of $w/2$ in the original publication), the length of a channel and its adjacent trough, the thickness of the layers excluding the channel thickness, the channel thickness and the bending radius respectively.

This model however is not describing the system shown in figure 4.7, as the original authors assumed. This model instead describes a bending axis that is horizontal and perpendicular to the page, rather than one normal to the page as is shown in the diagram, i.e. the SPNI would be being bend longitudinally rather than transversely.

If the original analysis [48] is repeated we also find that the equation quoted in the paper is incorrect even when working with the authors original assumptions as it should read

$$y_{neutral} = \frac{pbh + 0.5pb^2 + 0.5s\mathbf{h}^2}{pb + sh} \tag{4.10}$$

rather than

$$y_{neutral} = \frac{pbh + 0.5pb^2 + 0.5s\mathbf{b}^2}{pb + sh} \tag{4.11}$$

Despite the errors in the analysis in the mechanical structure, studies prior to this thesis have shown between an 80% and 97% success rate in maintaining the continuity of gold layers when rolling SPNI devices [31].

This all serves to raise questions about the validity of the stress model. Thus highlighting the need to investigate the structural sensitivity of the embedded gold on the neutral plane location.

To investigate structural performance further an experiment is designed to test the robustness of the gold layer when the stress applied is changed due to different rolling configurations. The experiment consists of taking specialized SPNI devices and subjecting them to controlled strains by bending them around rods.

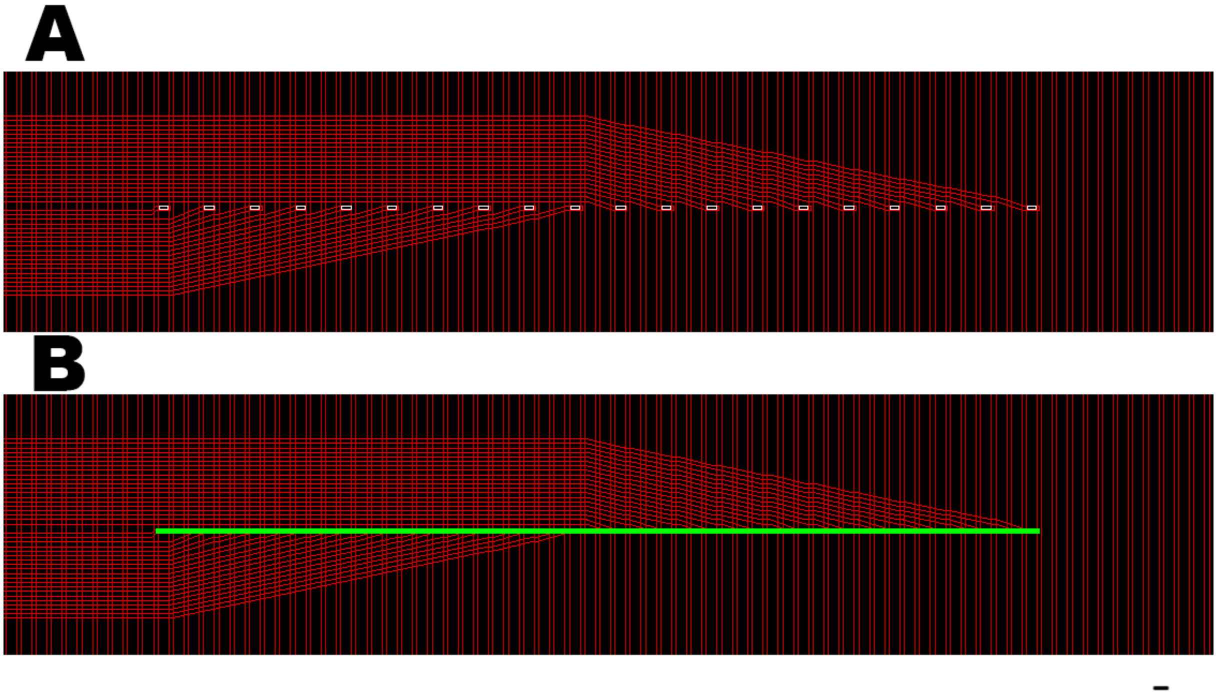

Figure 4.8: Showing how the original electrode gold layer (A) is modified in (B) by adding a line to the mask that shorted all of the electrodes together when fabricated. Scale bar is 170 μm.

4.3 Bend Testing Methodology

A batch of eight specially designed SPNIs were fabricated using the methods outlined in chapter 3. Three of these devices survived to final testing. These SPNIs were fabricated with a specially designed gold layer mask so that their electrode sites were shorted together as in figure 4.8. The electrical integrity of these channels is measured and then resistance measurements are taken between each channel and the first, i.e. the resistance is measured between electrode pin 1 and 2, 1 and 3, 1 and 4, etc. The measurements are taken using a Fluke hand held multimeter, using its ohmmeter setting which gave results rounded to the nearest ohm.

A bending jig was designed as can be seen in figure 4.9. The SPNI was placed in this jig and bent around a rod of 0.45 mm diameter. The SPNI would be forced to conform to the cylinder so that the radius of curvature of the bend would be known.

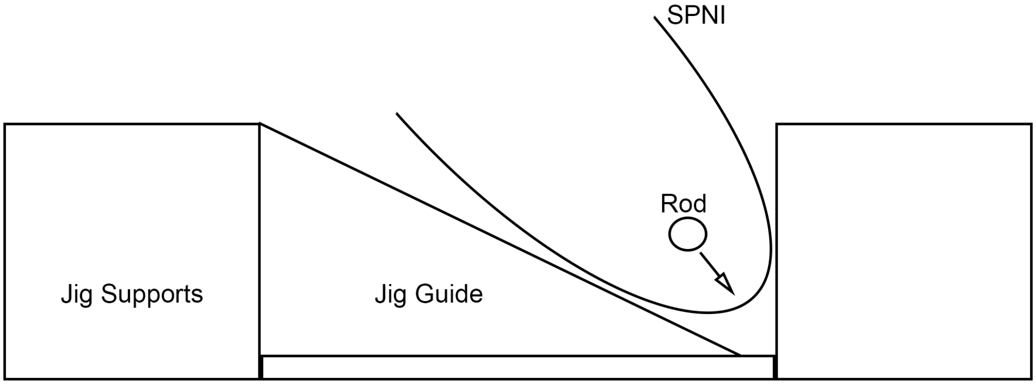

Figure 4.9: A schematic of the jig used in the bending experiments. The 0.45 mm rod is pushed down onto the SPNI into a grove of sufficient diameter to force the SPNI to conform around the rod when presented.

Using the strain equation provided earlier, a 0.45 mm rod provides a strain of 3.2% and a stress of 1.5 GPa on the gold layer assuming the most robust case where Young's modulus is 47 GPa. This is a stress more than three times the 477 MPa ultimate tensile strength of the strongest thin film gold quoted [53].

Smaller rods than this are difficult to source and would not have provided any additional information as this diameter of rod is smaller than the smallest bend within the SPNI that the gold would be subject to.

The resistance measurements are then repeated as the SPNI is held in place around the rod. If the strain is too much for the gold the resistance between two electrodes would read as an open circuit. This would mean that the stresses within the SPNI are sufficient to break the gold film. Measurements are taken with the gold layer in tension and compression by changing which face of the SPNI is bent upward. Finally the devices are fully rolled in the new configuration, with channels facing outward, and retested. The results for the three devices tested in this manner can be seen in the next section.

4.4 Resolving Neutral Plane Reliance

Three of the modified SPNIs were tested, giving 34 measurements in total. The resistance measured between each electrode contact and the first can be seen in figure 4.11. A particular path was chosen through each device (the path from electrode contact point 7 to electrode contact point 1, which has a total path length of 65.5 mm). The resistance for this particular path in each of the devices for each measurement taken can be seen in figure 4.10. The variability shown between samples in these results is a consequence of the inherent variabilities in the fabrication process, this is similar to studies on the SPNI by Barrett (2013) [31] and Benmerah (2015) [57].

Figure 4.10 shows the stability of the resistance measurements and is typical for all of the paths measured. It demonstrates how the gold does not break during tension or compression, and how the resistance rises when rolled. The resistance is not expected to rise during the compression and tension tests due to the small affective area of the strain caused by the rod. The area over which the rod causes the gold to stretch is too small to have an effect on the resistance of the gold path. However, once the SPNI is rolled the entire area of the SPNI is under strain, which is enough to increase the resistance by a few Ohms.

Figure 4.11 shows results from three individual devices. Each of the devices have results for four states, relaxed (i.e. under no strain), compressed (i.e. bent in the direction which causes the gold layer to be compressed), in tension (i.e. bent in the direction which stretches the gold layer) and finally fully rolled in tension.

The values are collected by measuring resistances between the first electrode pin of the device and the all other electrode pins, as depicted in figure 4.12. These results are converted into path lengths by measuring the length of the gold tracks through the shorted electrodes between each of the measured channels.

The results show that the resistance values from the different electrodes to the test electrode do not change appreciably when under compression or tension. After each bend test the resting resistances are retaken and in each case they remained exactly the same

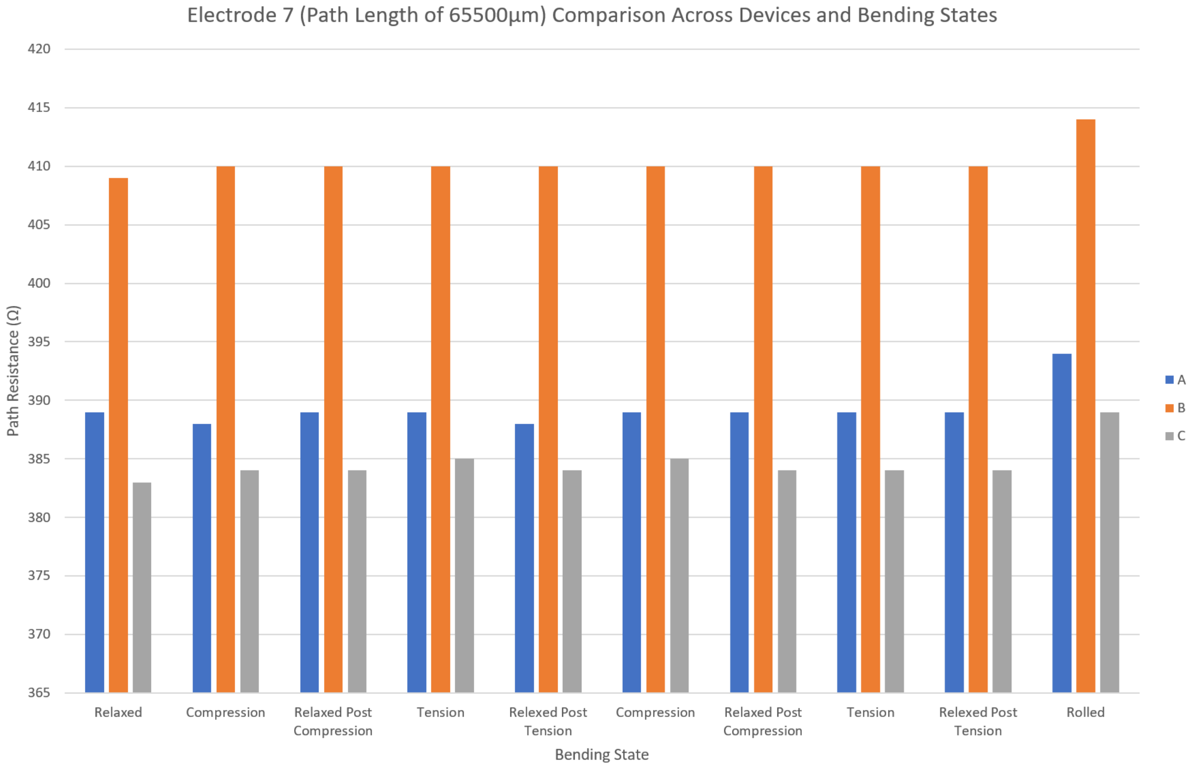

Figure 4.10: The path resistances of three devices: A,B and C, were tested relaxed, then compressed, then relaxed, then under tension, another cycle of those states and then finally rolled. The graph shows one electrode measurement across all the devices and that the resistance across the test states remained constant. The shows that the gold layer did not break during the tests, with the exception of the fully rolled tests where the resistance increases in each sample. This is due to the strain across the entire device increasing the path length enough to have an appreciable effect on the path resistance.

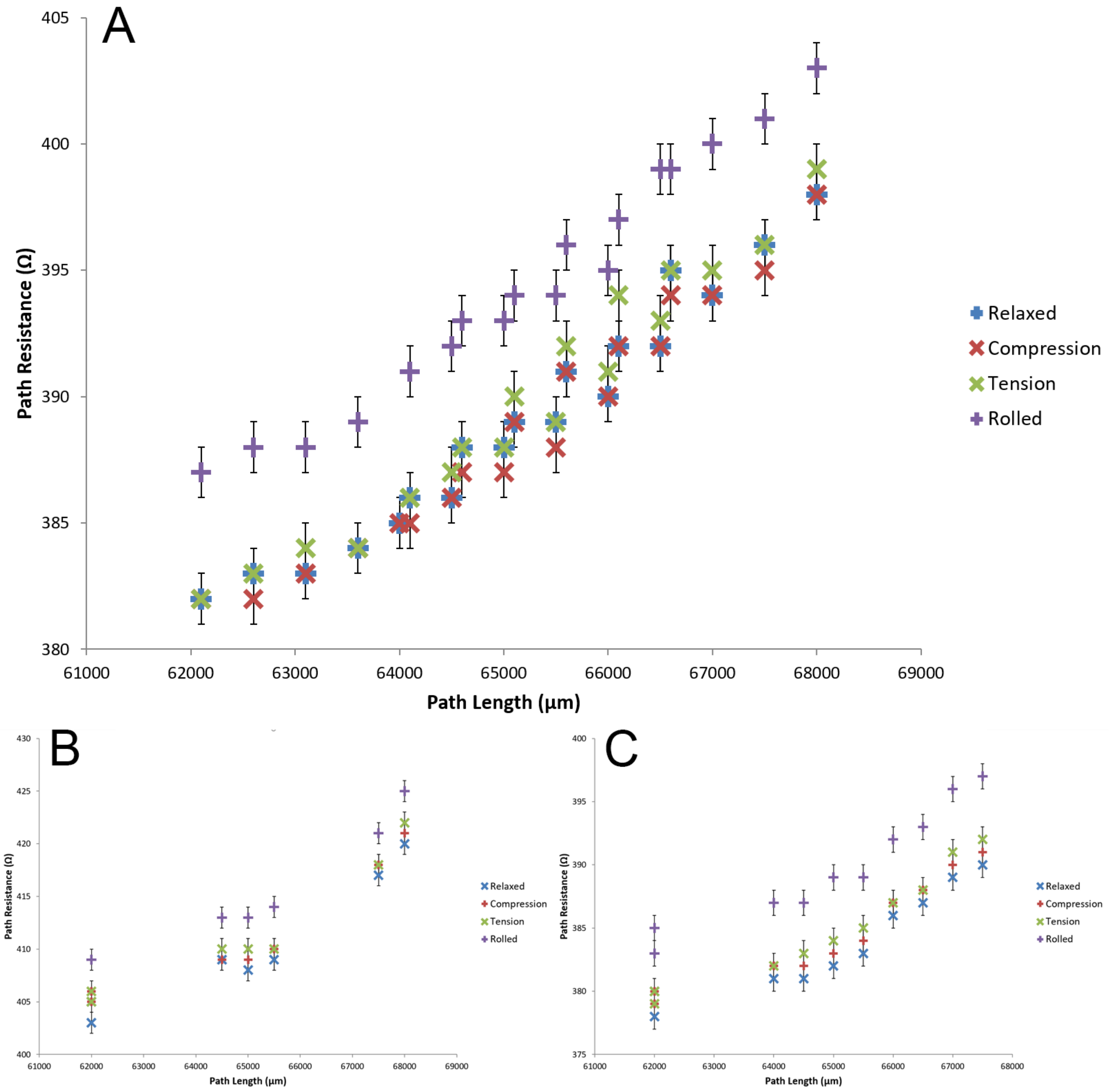

Figure 4.11: These results show the resistance measured from each electrode to the first. The path length has been calculated and plotted here for ease of comparison. Image A shows a device with 18 out of 20 channels which survived fabrication. Image B and C show devices where 6 and 10 channels are functional respectively. All results show an increase in resistance per unit length. Error bars show potential measurement error of ±0.5 Ω.

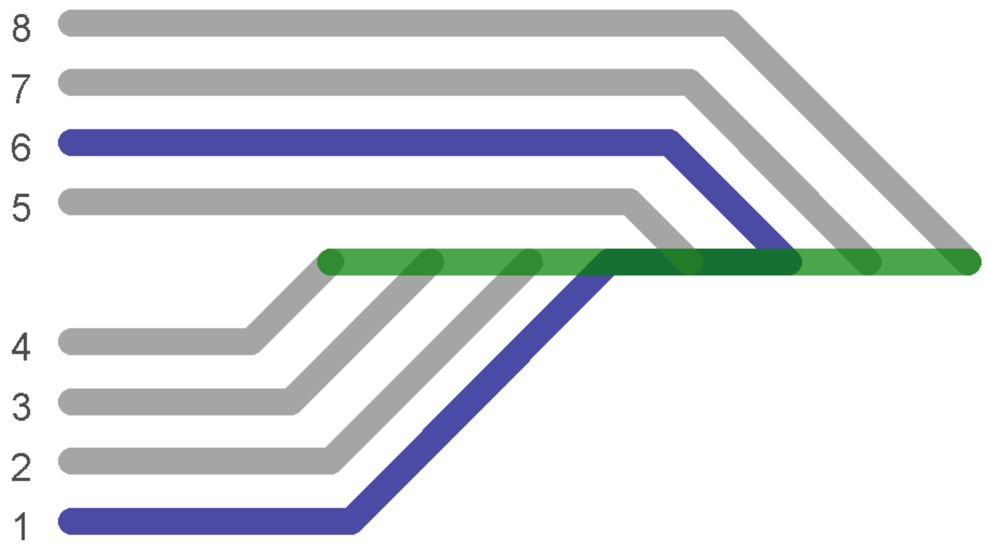

Figure 4.12: A schematic that shows the shorted section of the gold tracks in green with the tracks in gray. The blue highlighted section shows how the path length of the measurement is calculated, for this instance between electrode contact 1 and 6.

after each test.

The results of this experiment show that bending around the cylinder and thus subjecting the gold layer to 1.5 GPa of stress in compression or tension does not break the gold layer. The resistance does not temporarily change when the gold layer is in compression or tension due to the effective area of the stress being too small to generate any meaningful differences in resistance measurement. However, when the whole SPNI is rolled the entire length of the gold layer is under stain and so the resistance between channels can be seen to increase.

The results of one of the relaxed devices was verified using an impedance analyzer which showed good agreement with the resistance measurements made using the ohmmeter.

These results begin to question whether the placement of the metallic layers in the neutral plane is a requirement for mechanical stability of the gold *in situ*.

4.5 Internal Stresses and the SPNI Redesign

From the measured resistance results of the rolled case an estimate of the average stress experienced by the gold in the SPNI can be made. The average increase in resistance between unrolled, relaxed states and a fully rolled state is 5.3 Ω (with a standard deviation of 0.8, n=34). The differences measured can be seen in figure 4.13.

If Pouillet's law is taken and applied to the relaxed and rolled states of the SPNI we get equations 4.12 and 4.13.

$$R_{relaxed} = \frac{\rho l}{A} \tag{4.12}$$

$$R_{rolled} = \frac{\rho (l + \Delta l)}{A} \tag{4.13}$$

From this we can get equation 4.14

$$\frac{R_{relaxed}}{l} = \frac{\rho}{A} = \frac{R_{rolled}}{l + \Delta l} \tag{4.14}$$

Extracting Δl gives equation 4.15.

$$\Delta l = (\frac{R_{rolled}}{R_{relaxed}} - 1) \times l \tag{4.15}$$

Thus the strain can be calculated by comparing rolled and unrolled resistances, giving equation 4.16.

$$\epsilon = \frac{\Delta l}{l} = \frac{R_{rolled}}{R_{relaxed}} - 1 \tag{4.16}$$

Using equation 4.16 across all tested channels of one of the devices, reveals that the strain experienced by the SPNI when rolled varies between 1% and 1.8%. This is in-line with the expected 1.3% strain average on the gold in a rolled SPNI. This expected value is calculated by fitting circles of known radius to images of the SPNI and calculating the

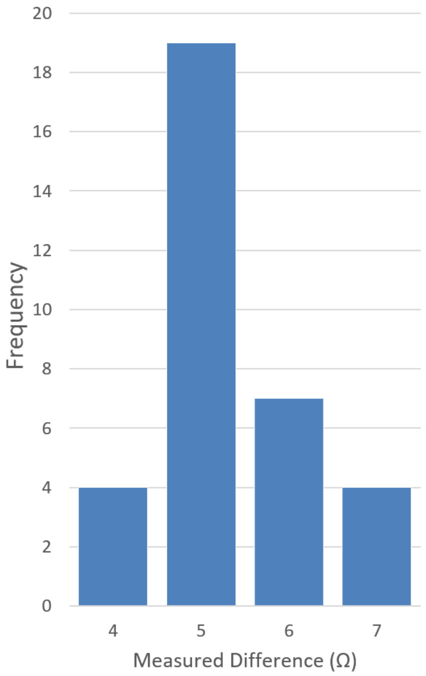

Figure 4.13: The frequency of measured differences between rolled and unrolled resistance results across all tested channels.

spiraling contribution to the strain using equation 4.5.

Due to the confusion generated by neither of the theoretical models fully accounting for the behavior observed it is thought that a more complex interaction needs to be taken into account. It is thought that the lamination of the gold by the polyimide is acting as a protection mechanism, preventing the gold from reaching its breaking point. It is thought that as the structure is bent and the gold undergoes deformation, that the plastic nature of the PI is pulling back on the gold, therefore countering some of the applied force. If this is so then removing the top layer of PI from the structure should dramatically weaken this effect and provide further evidence to whether the gold can withstand strains exceeding 4%.

Another batch of eight shorted SPNIs were fabricated, this time with the 5 μm encapsulation layer and channel layer missing. Out of the two devices which survived to final testing, 75% of the channels tested survived bending both in compression and tension. The results for one of these devices can be seen in figure 4.14. In the other device over half

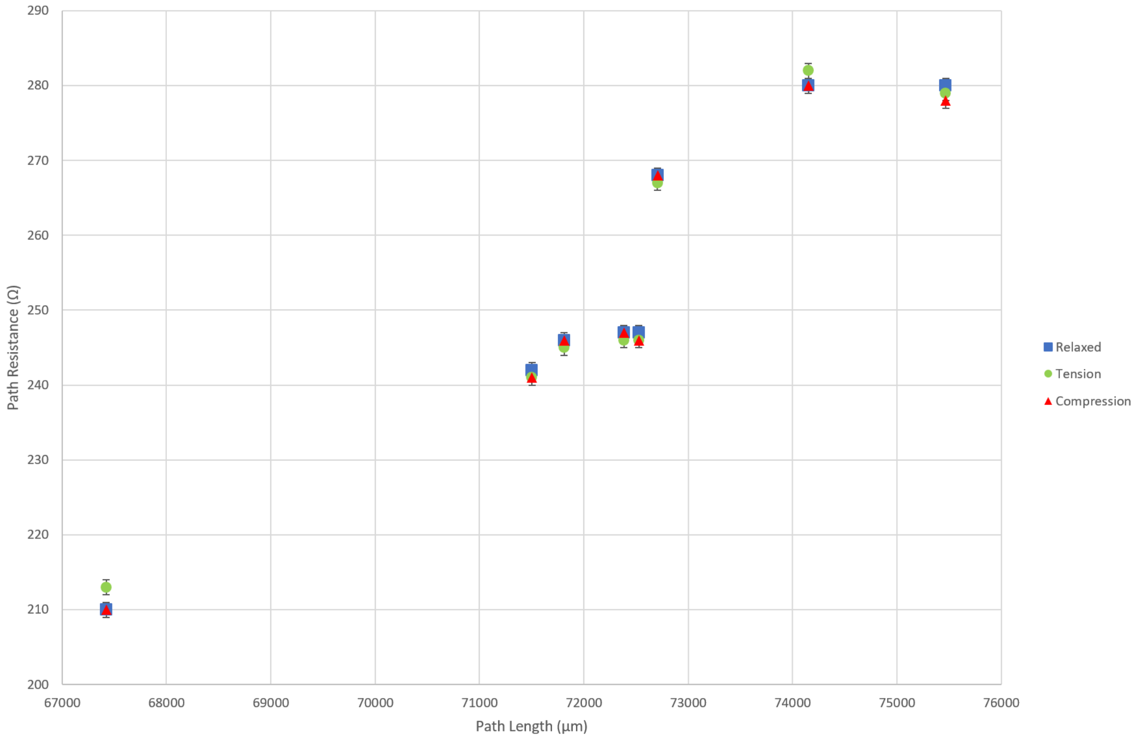

Figure 4.14: These results show the resistance measured from each electrode to the first in one sample that has no channels or encapsulation layer. Error bars represent a ±0.5 Ω measurement uncertainty.

of the gold tracks had broken before testing. It is unclear whether this was a fabrication or a stress based issue. In this configuration the gold would be under approximately 5% strain under a stress of around 2 GPa, lending even more support to the durability of gold when on a polymer.

Without the laminate significantly more tracks failed either during or before testing. However, 12 of the measured tracks survived the applied strain, providing evidence that 100 nm gold is withstanding strains of around 5% without fracture.

It could be that the gold is simply no longer acting in the elastic region and that the assumptions made about the stresses on the gold are faulty, however these assumptions are common in analyses made during neural implant design. It may be a combination of plastic deformation and another phenomenon are at play which needs further investigation. Regardless of the type of deformation, these results shows that the gold can withstand much more strain than previously thought.

4.6 Discussion Regarding Metal Laminates

Based on the results from this experiment it is worth revisiting the literature to explain the result. The Benmerah-Lacour model assumes that the mechanical fracture of thin film gold within the SPNI is likely if the gold layer is not located closely to the stress neutral plane of the structure [48]. This is mirrored in other studies such as Chou et al (2013), who fabricated a PDMS based device for insertion into the brain through a small trephination hole in the skull, and states the metalisation needs to be placed in the stress neutral plane of the device in order to avoid the large deformations causing mechanical failures during insertion [58]. Doubley et al (2011) developed a highly conformal electrode array that uses the same assumptions, which are very common within the field [59].

The assumption about golds fragility is warranted as regardless of deposition method or grain size of the deposited gold the ultimate tensile strength of thin films of gold differ between 257 MPa and 477 MPa for films around 0.2 μm as shown by Emery and Povirk in 2003 [53]. Similarly the Young's modulus varies between 39 and 78 GPa, depending on deposition method [53, 60–62]. However in any of these ranges the stresses within the SPNI should break the gold given that these values hold. All of these results from the various papers however have made measurements of free standing gold films and have not analysed the effects that laminating a metal film or placing a metal film on a more compliant material may have on its mechanical properties.

There is, however, much in the literature on flexible electronics that succeed in getting gold films to withstand much higher strains than are usually observed. These methods include using creative geometries of gold [63], using rigid islands with short and flexible interconnecting zones [64–68] and prestraining substrates so that upon the relaxation of the material ripples form in the gold which can be flattened out as the substrate is later deformed [69]. It is possible that during the final baking process of the SPNI, the PI shrinks to such an extend that it acts as a prestraining method. However, upon close inspection of the profile of the gold, no curving geometries into the plane of the substrate can be observed, which is country to what other studies utilizing this method

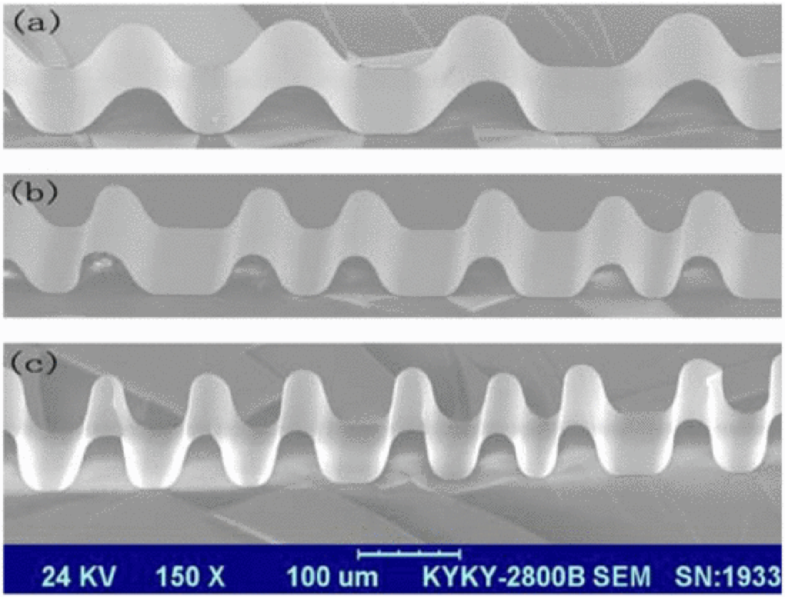

Figure 4.15: Taken from [68] shows SEM images of 100 μm-wide wavy gold interconnections after release from pre-strain of (a) 25, (b) 50 and (c) 100%.

have reported, an example of which can be seen in figure 4.15.

If a literature survey is conducted outside the focus of stretchable gold and mechanical design of neural interfaces other examples can be found. Notably in steel and copper where it has been shown that adding laminates to a metal can increase the robustness of its mechanical properties [70, 71]. [70] shows how a laminate of brittle high-strength steel and ductile low-strength steel can reduce localised necking and increased the strength of the component steels.

Results even more applicably have been shown in [71] by Lu et al., 2007. That metal films on polymer substrates can demonstrate surprising stretchability. This study shows how a 12.7 μm thick copper film when deposited onto a PI substrate can be stretched by up to 50% before micro-cracks begin to emerge.

The failure mode of the copper is experienced when localised strain (usually around an impurity) produces a local elongation which deforms quickly and propagates a break. The introduction of the polymer however prevents this strain localization by having an averaging effect over the entire metal surface. It thus produces an effective retardation of the stain localization, hence preventing breakage from occurring. A diagram of this can

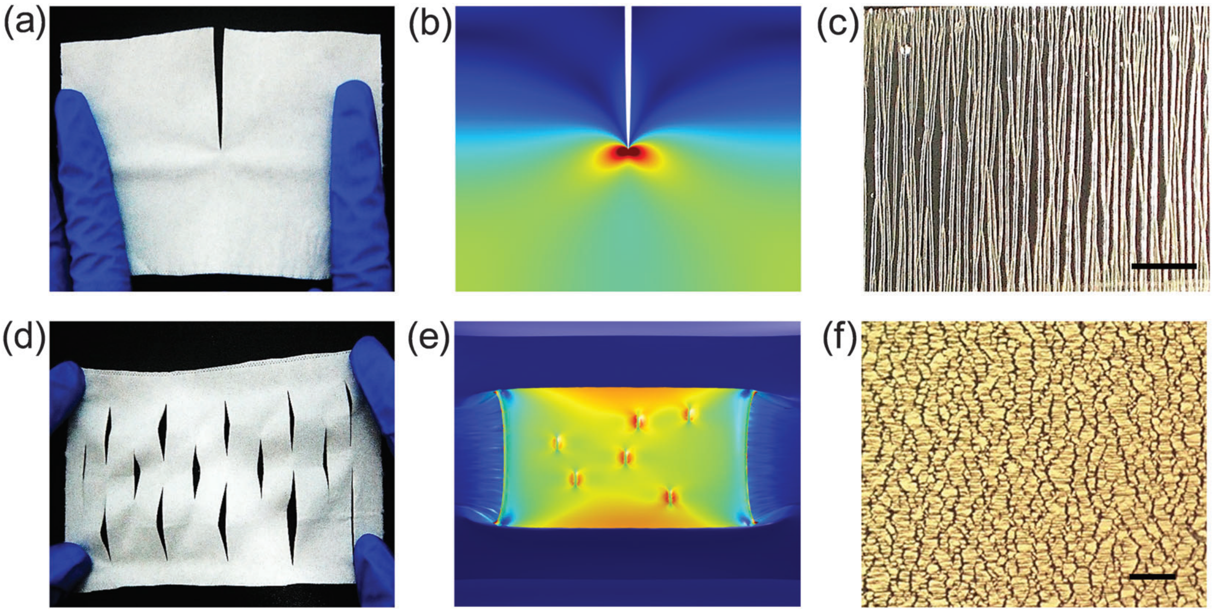

Figure 4.16: Taken from [73] who uses paper to demonstrate the effects of strain localization. b) shows a crack, which is analogous to an impurity in the gold layer, on a gold layer that is poorly adhered to a PDMS substrate. e) shows strong adhesion to a PDMS substrate. As can be seen by the heat maps on the two models the stress on the strongly adhered averages the strain over the surface of the polymer, as opposed to the poorly adhered specimen which has localized strains which will serve to propagate the crack. Scale bar: 20 μm.

be seen in figure 4.16.

Although the 12.7 μm copper is significantly thicker than the 0.1 μm gold contained within the SPNI, this mechanism is still likely to apply. A similar study has shown that gold of 100nm can experience the strain averaging effect when on PDMS [72].

It is possible, as has been reported elsewhere, that the gold is in fact forming microcracks under the strain and thus maintaining conductivity via different routes through the cracked surface, however this is less likely as no cracks are noticed and one would expect a larger change in the measured resistance when under strain if microcracks are also widely present in the gold. It is more likely that laminating the gold with two sheets of polyimide is having a dramatic effect on averaging the strain over the device and thus not allowing strain localization to occur at weak points in the gold which would have acted as failure points without lamination.

4.7 Conclusions on stresses affecting the SPNI redesign

The sealing of the SPNI requires it to be rolled in the opposite direction than originally designed. This has been proven not to be a problem in the case of the SPNI as the gold layer can withstand at least 5% strains when mated with a PI substrate. This has been seen in other fields but has now been shown in neural interface technologies. The conventional wisdom in the field is to put the metalized layer within the neutral plane of the device. Although this may still be advisable for overall robustness and ease of fabrication, it should be noted that it is not a necessity for good functionality. This opens up the possibility of more complex structures being used in neural interface technology such as multilayer conductors and integrated components which will dramatically increase possible electrode densities and interface functionality.

It has been shown rolling the SPNI in a configuration country to its initial design should not interfere with the performance of the metalization. Due to this a structural redesign of the device is not necessary when incorporating the sealing layer into the device.

When including the PDMS layer the strain will increase on the system by forcing the SPNI to conform to a tighter spiral. This did not have an effect on the viability of the gold layer and suggests that greater strains could be achieved before functional retardation.

The next step to inclusion of a functional sealing layer is to rigorously test the effect of PDMS sealing on the SPNI. Before a thin film of PDMS is incorporated into the SPNI layer structure and the quality of the electrical seal can be analyzed, a discussion into the nature of electrode interfaces needs to be undertaken, the next chapter will discuss how electrodes behave and go on to demonstrate how the effectiveness of a seal may be evaluated.

CHAPTER 5

THE ELECTRODE-ELECTROLYTE INTERFACE AND THE ELECTRICAL BEHAVIOR OF ELECTRODES

The previous chapter has shown how a PDMS film can be incorporated into the mechanical structure of the SPNI without requiring a redesign of the device. In order to measure the PDMS membrane's effectiveness on the reduction of cross-talk within the SPNI, the nature of the electrodes themselves needs to be addressed. This chapter outlines the relevant electrode theory, going on to apply this in the context of a brain interface that is used in a study on sensing epileptic activity of the brain.

The chapter then goes on to present how the impedance of electrodes can be analysed using standard circuit analysis techniques and how impedance measurements are conducted. The measurement technique is validated using the brain array followed by an assessment of the limitations of the impedance measurement process and how the solutions in which electrodes are submerged can affect this.

5.1 Cross-talk and Impedance

The stimulation signal cross-talk experienced with the SPNI in [25] was a result of electrical currents flowing from the stimulated electrode into other, adjacent electrodes, causing voltage changes strong enough to trigger undesired action potentials. To understand this process electrodes and their properties need to be considered.

Electrodes in the context of the neural interface act as biological transducers which convert between ionic currents in solution and electronic currents in metals. The interface between the ionic and electronic domains is extremely important when it comes to analysing the performance of an electrode. Electrodes have a characteristic impedance profile which can be used to characterize this process.

Impedance is the opposition to current flow in an electrical system and affects the current phase and magnitude. The impedance of electrode/electrolyte interfaces can contain much information about the performance of the electrode and as such impedance spectroscopy is a standard tool used in testing neural interfaces, along with other electrode types. By submerging an electrode in an electrolyte solution, key parameters can be extracted by studying how the electrodes impedance changes over different frequencies.

5.2 Electrode Electro-chemistry

The impedance model of the electrode/electrolyte interface was subsequently developed between 1853 and 1947 by Helmholtz [74], Gouy [75], Chapman [76], Stern [77] and Grahame [78], resulting in the development of the Grahame model [78]. The Grahame model states that when a metal is placed in a solution it has a charge density that depends on its electrical properties. This charge density can either supply an excess or deficiency of charge at the surface of the metal. The resulting charge attracts ionised and polarised molecules to the surface of the electrode which will absorb some of these molecules and reach equilibrium [74]. The absorbed molecules do not fully compensate the charge balance, but do prevent other charged species getting in close physical proximity to the metals surface [77, 78].

Ionic species in solution attract water molecules which form a shell around the charged ion. The ions and their shells with opposite polarity to that of the electrode are attracted to the metal surface [75, 76]. This results in a model that can be seen in figure 5.1.

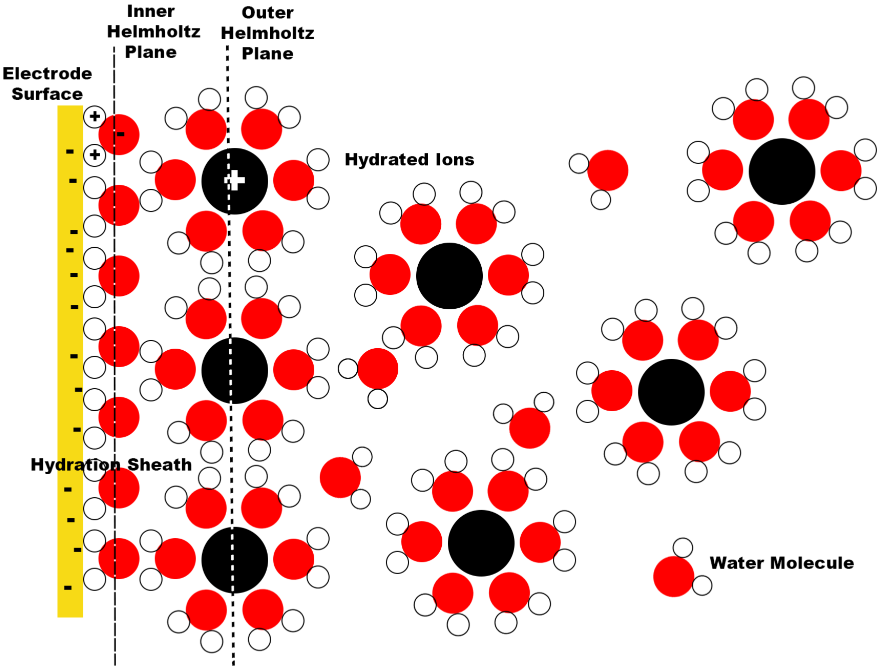

Figure 5.1: A diagram of the electrode-electrolyte interface. When charged the electrode surface attracts highly mobile water molecules and less mobile ions in the solution. These form a layer on the surface of the electrode with the inner and outer Helmholtz planes as shown. In the style of [79].

There are two routes by which charge can pass through this film coating the surface of the electrode. The first process is faradaic, where an electron gains enough energy to force its way through the molecular blockade to be absorbed by a species on the other side. This mode of transmission is not desired in neural interfaces as it requires large DC voltages to achieve and the resulting compounds formed on the other side of the layer due to chemical reduction can create undesired chemicals within the body and the oxidation of the electrode degrades neural interface performance.

The other transmission mode is due to the capacitative nature of the interface. Figure 5.1 shows that the metal plane is separated from the ions by two layers of solvent molecules. The plane at which the ions can get closest to the electrode surface is the Outer Helmholtz Plane (OHP) and the plane of charge from the specifically absorbed ions is the Inner Helmholtz Plane (IHP). The Helmholtz-Perrin model states that together the OHP and IHP are two parallel sheets with a characteristic charge separated by a dielectric of water molecules, and thus form a parallel plate capacitor. Due to this, energy can be coupled from one side of the capacitor to the other as long as the signals are AC in nature. Using this transmission mode bypasses the faridic processes and allows for current injection and detection without the downsides of direct current stimulation.

5.2.1 Electronic Model of an Electrode Interface

The overall electrical model of an electrode/electrolyte interface can be seen in figure 5.2. This consists of the electrode interface capacitance, C_I, the charge transfer resistance, R_t, the Warburg impedance, Z_w and R_s is the combination of the spreading resistance and the solution resistance. Each of which will be addresses in turn.

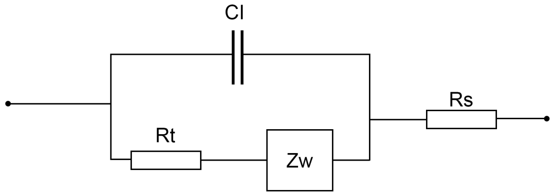

Figure 5.2: The equivalent circuit diagram of the electrode-electrolyte interface where C_I is the interface capacitance, R_t is the charge transfer resistance, Z_w is the Warburg impedance, R_s is the is the spreading resistance R_{spread} plus the solution resistance R_{sol}.

Interface Capacitance

C_I is the effective capacitance across the Helmholtz planes and can be modelled using the parallel plate capacitor equation, giving the Helmholtz model, equation 5.1.

$$C_I = \frac{\epsilon_r \epsilon_0 A}{d} \tag{5.1}$$

Where ϵ_r is the relative permittivity of the separating electrolyte solution, ϵ_0 is the permittivity of free space, A is the surface area of the electrode and d is the distance from the electrode surface to the OHP (approximately 1nm i.e. 10 Å). The relative permittivity is assumed to be 6 but can range from 6 - 50 depending on the solution, with the higher values for more concentrated solutions. The value of 6 was chosen as it gives a worst case assumption to the value of the capacitance and has been used to predict such systems accurately in previous applications [79].

Charge Transfer Resistance

Referring back to figure 5.2, R_t is the charge transfer resistance which is the opposition to direct current when an electron is traveling across the Helmholtz boundary, i.e. when the transfer is faradic in nature. This is given by equation 5.2.

$$R_t = \frac{V_t}{J_0 z} \tag{5.2}$$

Where V_t is the thermal voltage (approximately 25 mV at room temperature), J_0 is the charge density of the electrode (2×10^{-9} Ccm^{-1} for gold) and z is the valence of the ions involved in any interactions (this is safely assumed to be close to 1 for physiological conditions as the main species present in the body are K$^+$ and Na$^+$) [79].

Warburg Impedance

Z_w is the Warburg impedance which arises due to the concentration gradient into the solution varying with frequency. The higher the frequency the higher the concentration gradient due to the signal dropping off with distance to a greater extent at higher frequencies. The Warburg impedance is often cited as a RC network, but this can be misleading as it is really a complex impedance that acts with a constant phase shift of $-45°$, given by equation 5.3 [79].

$$Z_w = \frac{\sigma}{\omega^{\frac{1}{2}}}(1 - j) \tag{5.3}$$

Where σ is the conductivity of the solution and ω is the radial frequency [79].

Spreading and Solution Resistances

Once a current has left the surface of the electrode it then travels through the spreading and solution resistances.

R_{spread} is a resistance associated with the current spreading away from the electrode and is dictated by the geometry of the electrode. For rectangular electrodes is given by equation 5.4.

$$R_{spread} = \frac{\rho ln(\frac{4l}{w})}{\pi l} \tag{5.4}$$

Where ρ is the resistivity of the solution and l and w are the length and width of the electrode [79]. For planar disk electrodes R_{spread} is given by equation 5.5.

$$R_{spread} = \frac{\rho}{4r} \tag{5.5}$$

Where r is the radius of the electrode [79].

The spreading resistance represents the current spreading out from the surface of the electrode, the smaller the surface, the higher the resistance against the currents entry into the solution.

Once spread out into the solution the current will be subject to the solution resistance which is the resistance of the electrolyte itself, a result of the resistivity of the electrolyte and the geometry of the path between the electrode and ground. With electrodes of the scale considered in this thesis, the solution resistance is always minuscule when in comparison to the spreading resistance. This is due to the small electrode area causing large spreading resistances and the comparatively large solution volume causing small solution resistances.

As the spreading and the solution resistance always appear in series and are always linked, they will be referred to in the rest of the text as the spreading-solution resistance and will always be assumed to be equal to the spreading resistance.

Using these parameters it is possible to analyse electrode systems and to predict what impedance is to be expected from a particular electrode in a particular solution.

5.3 The ECoG Array: An Electrode Test Case

Before going on the analyse the electrode interface of the SPNI, a simpler electrode array was considered that had larger electrodes and no channels to take into consideration. This array was an electrocorticography (ECoG) array that was designed for use on the CNS to monitor epileptic activity in the brain. The array can be seen in figure 5.3.

5.3.1 The Electrocorticography Array

The ECoG array consisted of 26 disks of 480 μm diameter, arranged in a tapered layout designed to better conform to the hippocampus of the rodent brain.

The ECoG array was fabricated using the processes as outlined in chapter 3, with a 18 μm substrate layer, 100 nm gold conductor and 18 μm encapsulation. The arrays were ball-bonded to a custom made connector (1219, Omnetics) breakout board and impedance could then be measured using a custom made cable assembly.

As the electrodes on this array were large in comparison to those of the SPNI, they yield results that are more easily measured and as such present a good device on which to validate the impedance modelling and measurement.

5.3.2 Biological Results

As part of a collaboration with the University of Birmingham Medical School, School of Clinical and Experimental Medicine with Professor John Jefferys, the ability of the array to detect biological data was tested. The brain of an unconscious rodent was exposed and the ECoG array was placed on the hippocampus. The experiment took place in a faraday cage with the device connected to a preamplifier, which was then fed to a power amplifier feeding a data acquisition system, all of which were build in house.

The validity of the array was shown as biological data could be detected from the array.

One of the electrodes on the edge of the device was placed over the motor sensory part

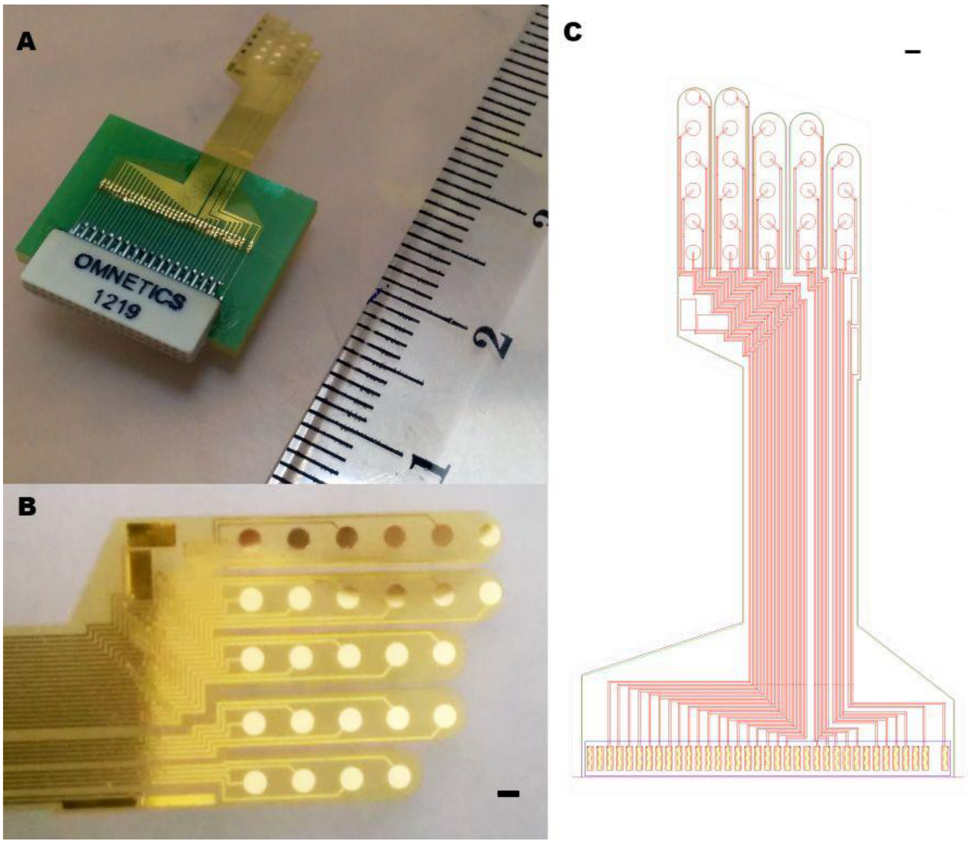

Figure 5.3: The ECoG device. (A) shows the device ball bonded to an interface PCB, (B) shows a close up of the 26 large electrode sites and (C) shows the mask schematic. Scale bars are 480 μm.

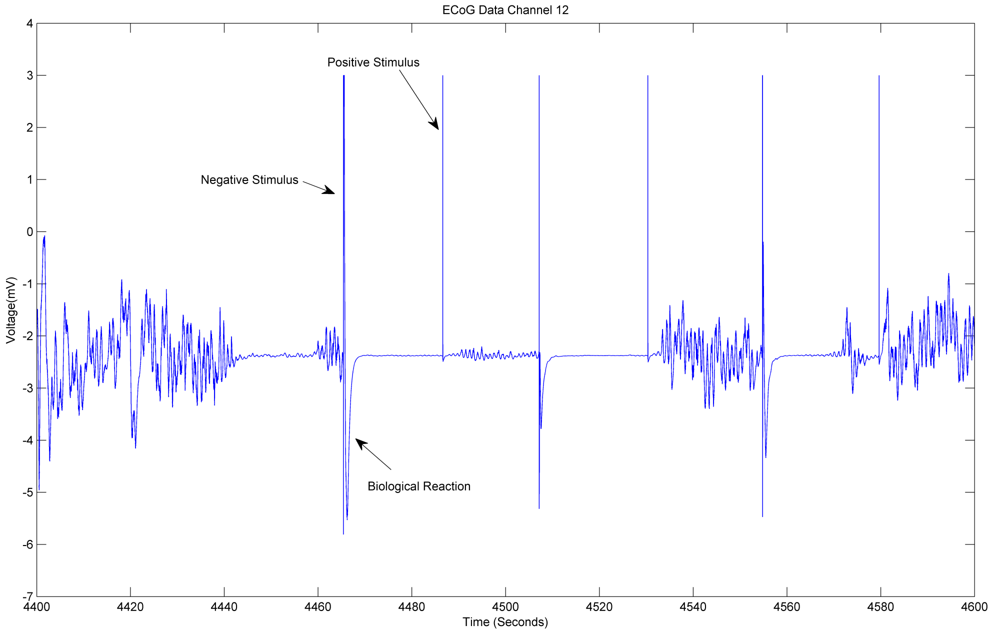

Figure 5.4: Biological results from *in vivo* testing of the ECoG device. Positively and negatively polarized stimulation pulses were transmitted to the brain. A curving response can be seen on positive stimulation which are absent during negatively polarized stimulation. This suggests that there is a biological activity rather than a measurement artifact.

of the rodents brain, the hind paw of the rodent was stimulated using an electric probe and a biological reaction was observed as can be seen in figure 5.4.

The results show a positive and negative stimulus applied to the hind limb, on the negative simulation a reaction was observed as the electrode potential returned to its resting voltage. However, this reaction does not occur when the polarity of the applied signal is reversed. This is the classic behavior of a biological reaction, as action potentials do not trigger unless the threshold voltage is exceeded. This provides evidence that biological signals can be gathered from these electrodes.

The impedance of these electrodes will now be discussed as an example of a good quality and functioning electrode.

5.4 Impedance Modelling

In previous sections we have considered the electrode/electrolyte interface; this model can be further simplified when considering only AC signals. In this case most of the current will bypass Z_w and R_t as the impedance of C_I can be given by equation 5.6.

$$Z_c = -jX_c = -\frac{1}{j\omega C_I} \tag{5.6}$$

Where ω is the angular frequency of the signal, Z_c is the measured impedance of the capacitor and C_I is its capacitance.

Equation 5.6 shows that the impedance of a capacitor is inversely proportional to the signal frequency. The negative sign denoting that the phase of the signal lags by 90 ° when crossing the capacitor.

The reduced impedance for higher frequency AC signals though C_I simplifies the model to C_I in series with R_s, the spreading-solution resistance, as current will shunt through C_I instead of flowing through the charge transfer and Warburg impedances. This leads to the impedance of the electrode interface simplifying to equation 5.7.

$$Z_e = R_s - jX_c = R_s - \frac{1}{j\omega C_I} \tag{5.7}$$

Taking the magnitude of this gives the real component of the impedance to be equation 5.8.

$$|Z_e| = R_s + \frac{1}{\omega C_I} \tag{5.8}$$

The capacitance can be found using the Helmholtz parallel plate equation, which for the ECoG electrode is equation 5.9.

$$C_I = \frac{2\pi r \epsilon_r \epsilon_0}{d} \tag{5.9}$$

Where r is the radius of the disk electrode (240 μm), ϵ_r is assumed to be 6 and d is 0.5 nm, which is a common value used for the distance to the Helmholtz plane [79]. This

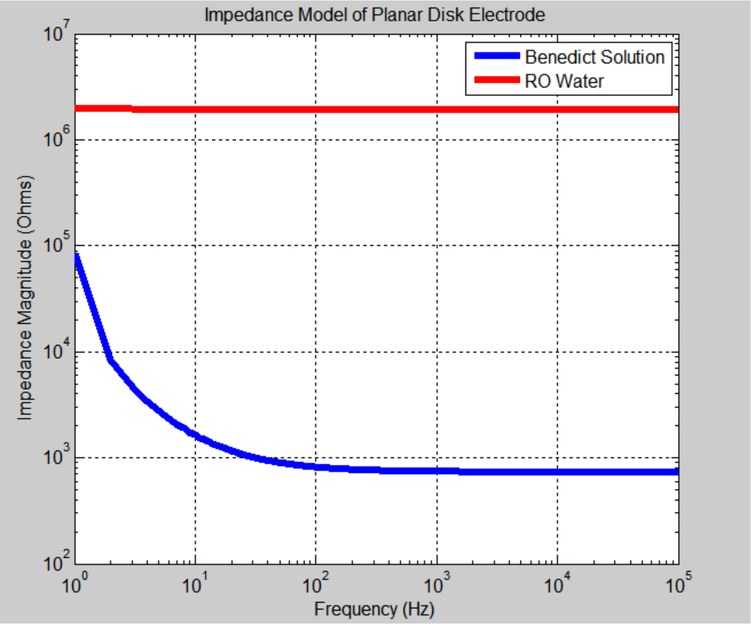

Figure 5.5: A simulation of the impedance of the ECoG array in Benedicts solution and RO solution based on the impedance equations.

gives an interface capacitance of 19.2 nF.

Using the equation for spreading resistance of a planar disk, the spreading resistance for the ECoG array is calculated to be 730 Ω in Benedicts solution and 1.9 MΩ for RO water. Assuming the resistivity of Benedicts solution is 0.36 Ωm and of RO water is 1.8 kΩm. Both of which were measured using a hand held conductivity meter.

RO or reverse osmosis water is water that has been treated to remove impurities, this causes RO water to have larger resistivity than other waters.

Using these values figure 5.5 shows the expected impedance magnitude of the ECoG electrode in the two solutions.

Figure 5.5 shows how in the Benedict solution, the capacitance of the interface dominates the impedance, reducing as frequency increases until the impedance reached the value of the spreading-solution resistance, which then dominates.

For the RO water however the spreading resistance is high enough to dominate the impedance over the entire spectrum.

This shows how physical properties of the interface can be used to predict the electrodes impedance profile.

5.5 Impedance Measurements

In order to test the samples an impedance analyser (4294a, Agilent) was used which uses an auto balancing bridge to determine impedance, which was seen in chapter 3.

A two point impedance measurement is carried out where the test electrode is placed in a test solution along with a counter electrode of negligible impedance, in this case a large platinum planar disk electrode.

The auto balancing bridge applies a 5 mV sinusoidal voltage between the two electrodes, the counter is kept as a virtual ground, artificially held at 0 V by a negative feedback amplifier. All of the current flowing through the cell is then passed through a known resistor. The voltage dropped across this resistor is proportional to the current flowing through it, so the current can be calculated. This is then compared to the input voltage and the impedance is calculated. This is repeated for each frequency of interest.

The frequency sweeps were set to between 40 and 10 MHz and the system outputs both impedance magnitude and phase data.

The experiment was conducted with the electrode array in both Benedicts solution, the impedance results for four representative electrodes can be seen in figure 5.6, and in RO water, representative results for which can be seen in figure 5.7.

Figures 5.8 and 5.9 are the corresponding phase profiles of the electrodes showcased in figures 5.6 and 5.7. These show that during flat regions of the impedance curves the phase tends toward 0 degrees phase, which is the characteristic response of a resistance. However, during sloping regions on the impedance curves, the phase tends toward -90 degrees, which is the characteristic response of a capacitance.

The average impedance profile for 10 of the 26 electrodes of the ECoG in both Benedicts solution and RO water can be seen in figure 5.10. This shows that the average impedance of the ECoG electrodes in Benedicts solution follows the expected progression, being dominated by capacitive processes at lower frequencies (as shown by the inverse proportional relationship), then being dominated by the spreading-solution resistance at higher frequencies. The spreading-solution resistance extracted from the graph for

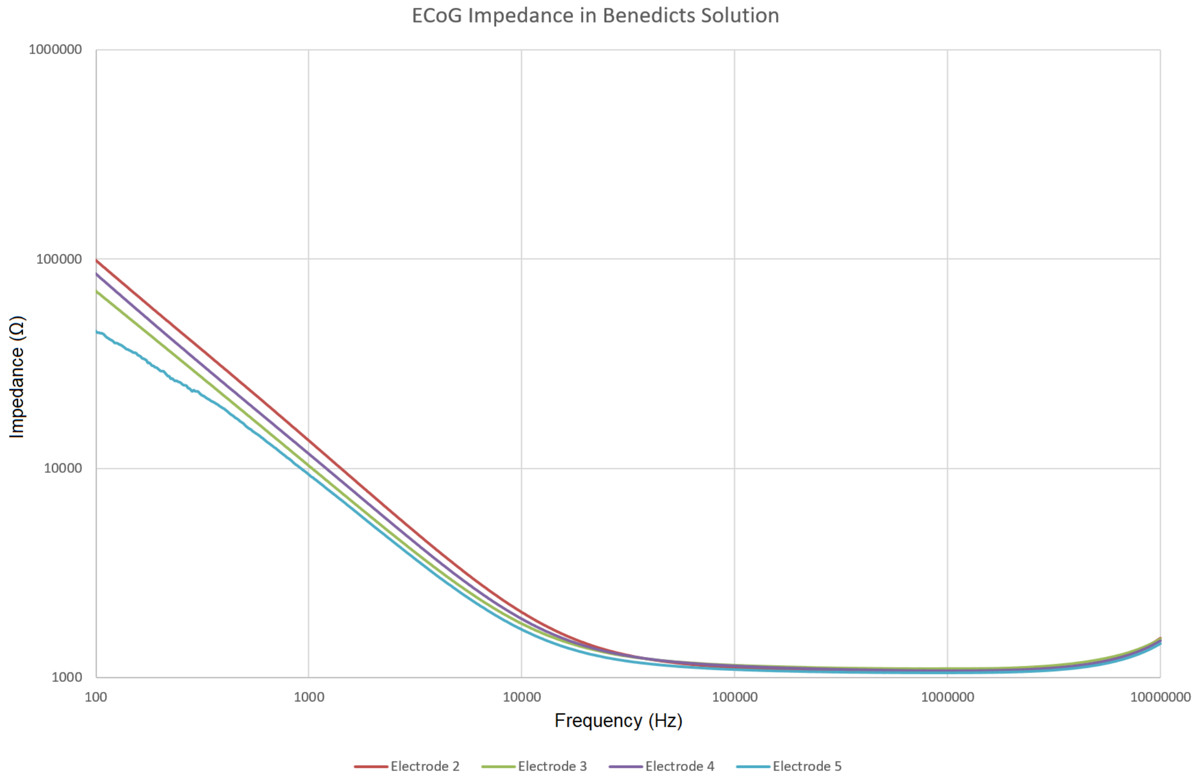

Figure 5.6: The impedance profiles of the first four working electrodes in the ECoG submerged in Benedicts solution.

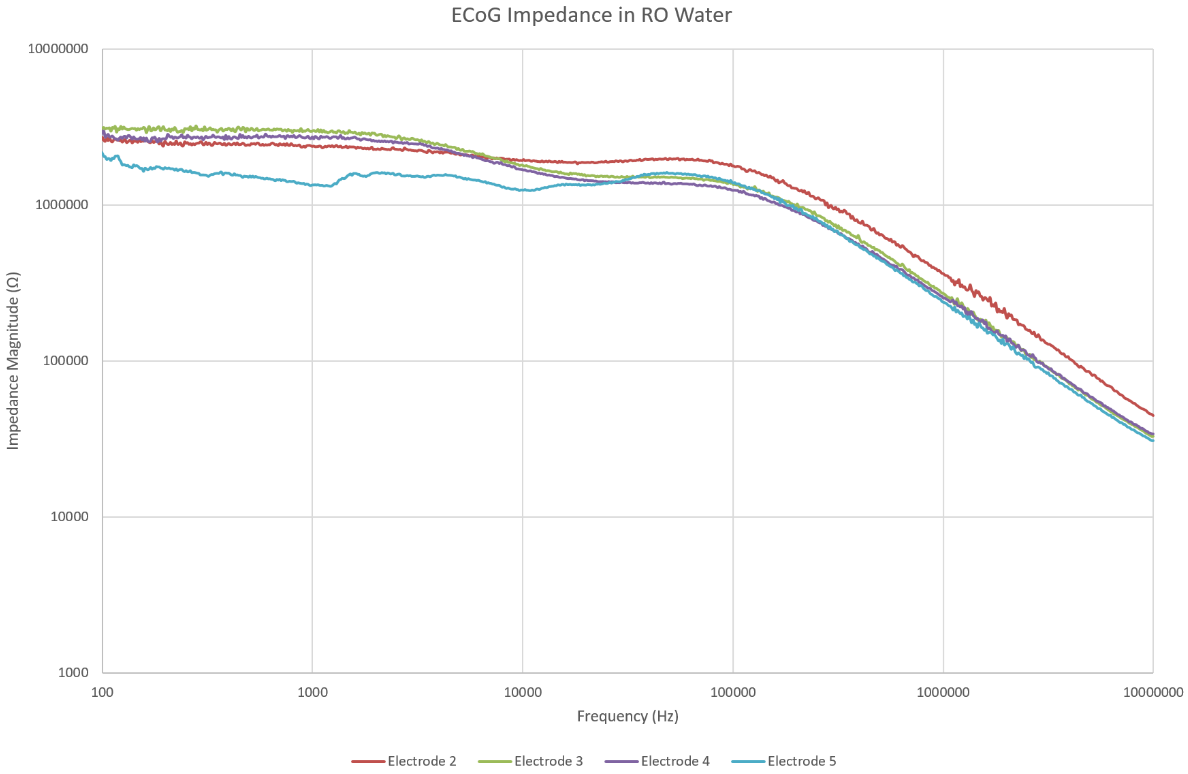

Figure 5.7: The impedance profiles of the first four working electrodes in the ECoG submerged in RO water.

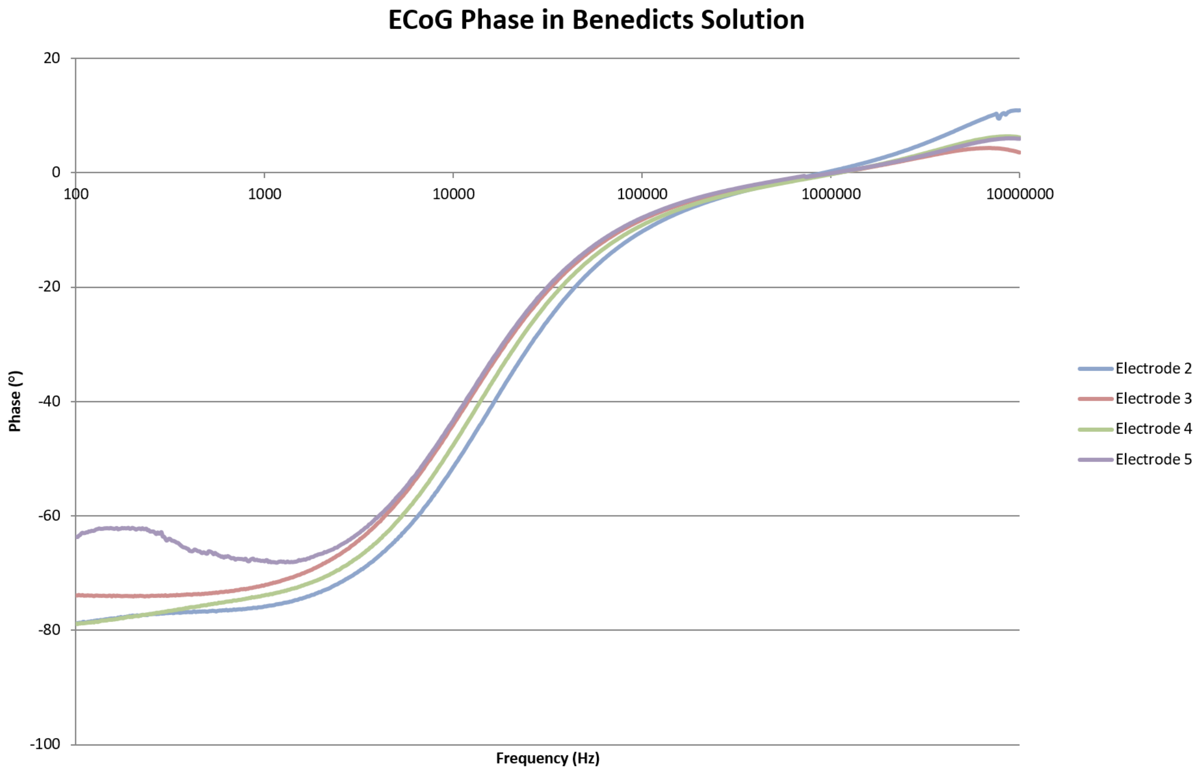

Figure 5.8: The phase profiles of the first four working electrodes in the ECoG submerged in Benedicts solution.

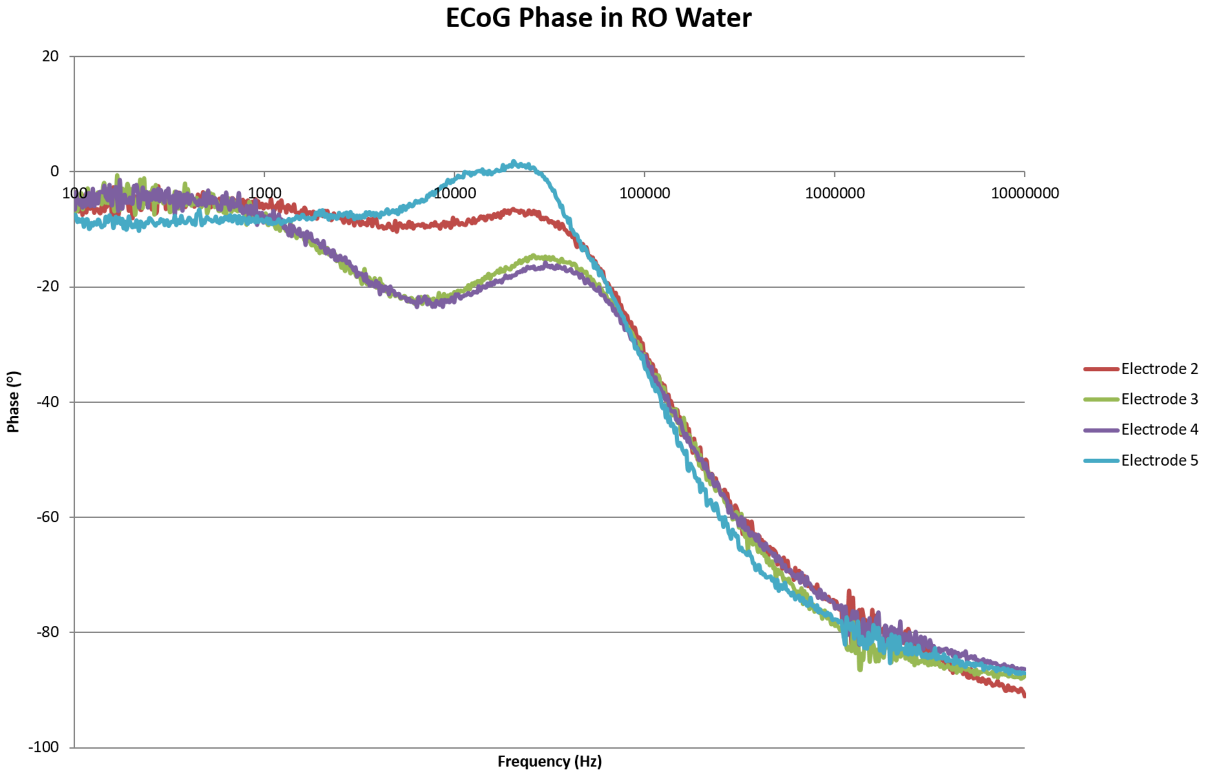

Figure 5.9: The phase profiles of the first four working electrodes in the ECoG submerged in RO water.

Benedicts solution is 1085 Ω, which is close to the estimated 730 Ω calculated from the spreading resistance equation.

It is also possible to extract the interface capacitance from this graph, as if a value is taken from the capacitance dominated section of the graph. For example, where $f = 1061$ Hz and $Z = 10,676$ Ω. It is possible to rearrange the equation used to predict the impedance of a capacitor to get equation 5.10.

$$C_I = \frac{1}{Z_{measured}\omega} \tag{5.10}$$

Using values from the graph gives a Helmholtz interface capacitance of 14 nF, which again is close to the expected value of 19.2 nF.

These results therefore validate the experimental setup as measurement results are in-line with expected values.

Considering the RO case, it can be seen that the solution resistance dominates across the spectrum as expected, up until around 25 kHz where the impedance begins to drop, as if the impedance were being dominated by a capacitor. This is an inherent limitation of the impedance measurement setup.

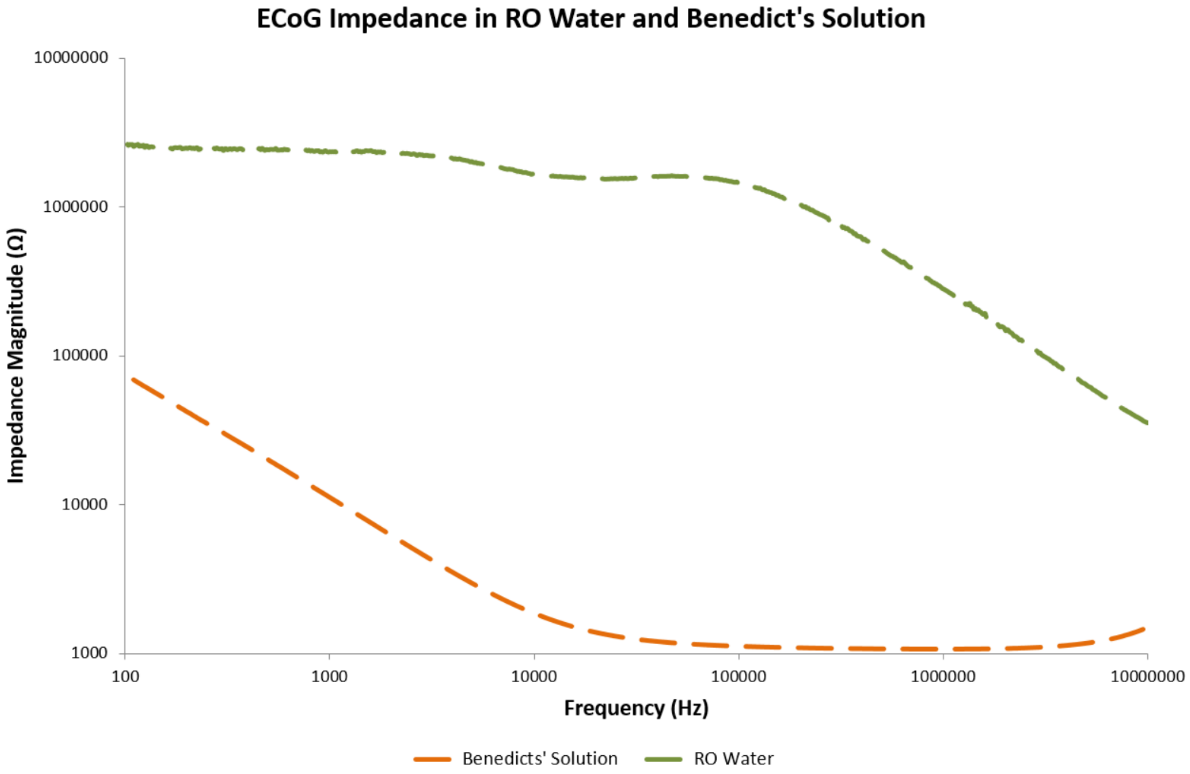

Figure 5.10: The impedance profiles of the average ECoG electrode impedance in RO water and Benedicts solution

5.6 Limitations of Impedance Measurements

The impedance measurements taken, using the setup described, have inaccuracies at either high or low frequencies. The low frequencies include noise, as measured from the voltage sensors inside the analyser due to the extremely high values of impedance. The higher the impedance, the lower the current through the balanced bridge of the analyser. Measuring these minuscule currents leads to sizable inaccuracies in measurements taken below 500 Hz, although averaging over multiple electrodes that have similar impedance profiles removes this noise.

The higher frequencies also suffer measurement error. As can be seen in figure 5.10 in the average RO water measurements, at frequencies above 25 kHz the impedance begins to reduce and exhibit capacitive behavior. This phenomenon is further demonstrated in figure 5.11, which is a measurement of a 1 MΩ resistor using the same setup as used in the impedance experiments.

A series of measurements were taken where the impedance analyser and the interface PCB were tested with a 1 MΩ resistor across their terminals. The 1 MΩ resistor placed directly across the terminals of the analyser resulted in a flat 1 MΩ reading across the entire frequency range. However, when the 1 MΩ resistor was placed across the terminals of the PCB and measured the results can be seen in figure 5.11. This characteristic response is due to parasitic capacitances from the internal wiring of the test chamber and of the PCB. These cause the signal to short as the frequency increases, reducing the measured impedance.

The overall shapes of the graphs produced will still yield useful results on the effectiveness of the electrode interface, however the limitations of the impedance measurement setup mean that the impedance can only be considered to be truly accurate between 500 Hz and 25 kHz. This range is suitable for the work considered in this thesis, however, careful selection of the solution will be required when considering the SPNI electrodes.

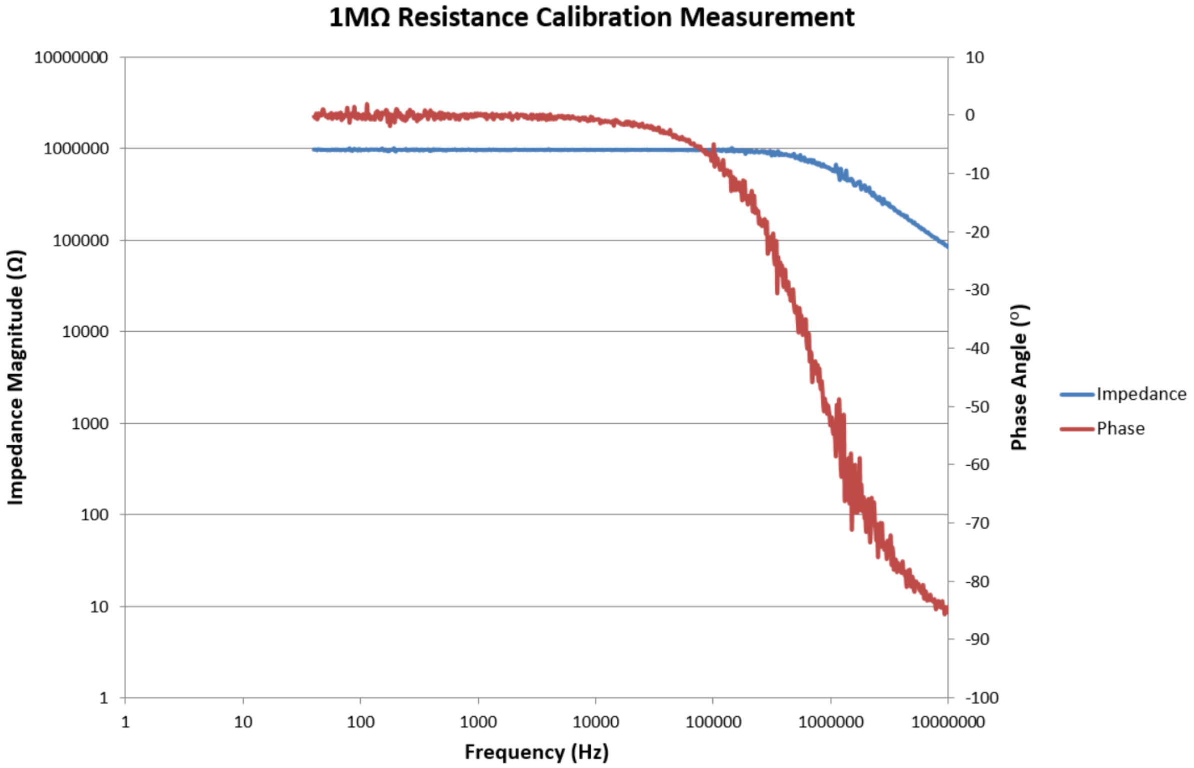

Figure 5.11: Showing the phase and impedance magnitude response of a 1 MΩ resistor in parallel with the PCB and connectors used to interface with the SPNI. Measuring a 1 MΩ resistor directly gives a flat 1 MΩ reading across the entire dynamic range. This therefore shows a parasitic impedance being added by the use of the interface circuitry.

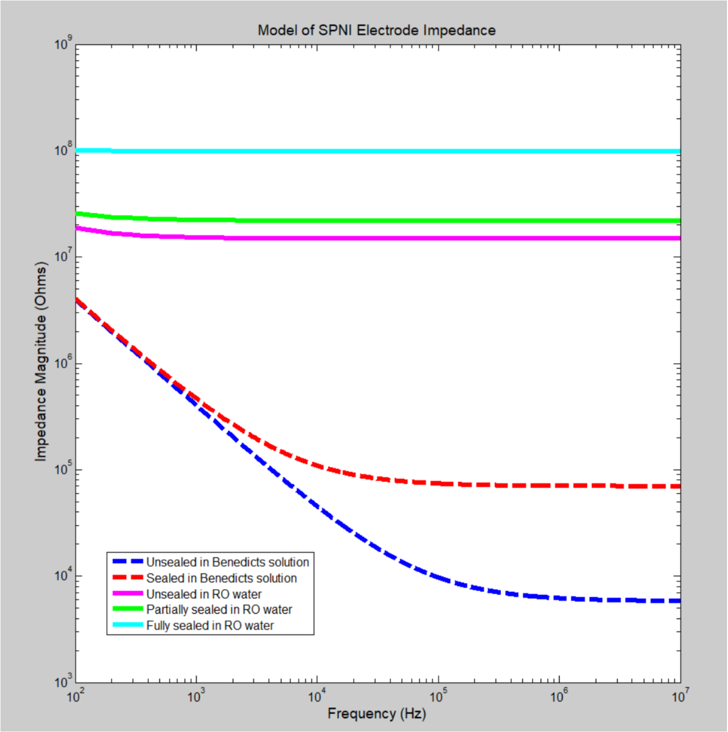

Figure 5.12: The expected impedance magnitude spectrum of fully sealed and fully unsealed devices in Benedicts solution and RO water, and a partially sealed channel in RO water using the theoretical equations.

5.7 SPNI Modelling

The impedance modelling and measurement have been shown to work on larger electrodes, however the SPNI electrodes are fifty times smaller than those of the ECoG array. This dramatically reduces the capacitance of those electrodes and increases the spreading-solution resistance. Along with this, the addition of sealed channels into the SPNI requires special consideration.

Considering first the capacitance of the rectangular electrodes gives equation 5.11.

$$C_I = \frac{wl\epsilon_r\epsilon_0}{d} \tag{5.11}$$

Where w is the width of the electrode and l is the length, these are 30 μm and 120 μ respectively for the SPNI. This gives an interface capacitance of 0.4 nF.

The spreading resistance of the rectangular electrode is 5250 Ω for Benedict's solution, and 49.5 MΩ for RO water.

If a channel with a functional sealing layer were included around this electrode, the resistance of the channel itself would be added between the spreading and solution resistances. The resistance of this channel can be found using Pouillet's law, equation 5.12.

$$R_{channel} = \rho \frac{l}{A} \tag{5.12}$$

Where $R_{channel}$ is the channel resistance though its entire length l and A is the cross sectional area of the channel.

However, the electrode itself resides in the center of the channel, allowing parallel paths out of either end, thus the parallel combination of these two resistances results in a impedance contribution of the channel to be equation 5.13.

$$R_c = \rho \frac{l}{4A} \tag{5.13}$$

Which gives $R_c = 64k\Omega$ in Benedict's solution and $R_c = 165\text{M}\Omega$ for RO water.

Including this in series with the interface capacitance and the spreading-solution resistance gives equation 5.14.

$$Z_s = \frac{1}{\omega C_I} + R_c + R_s \tag{5.14}$$

Using this for various channel scenarios produces figure 5.12, with the green line showing a partially sealed case, where the channel resistance is 0.7 MΩ, representing the impedance of a partially sealed channel filled with RO water.

This shows that the addition of the sealing layer should dramatically increase the impedance of the SPNI and thus should reduce the leakage current. It is shown that even if the seal is not total, a significant increase in exit impedance can be achieved.

Figure 5.12 does however show that the use of Benedict solution may be problematic to the accurate reading of the spreading-solution resistance. The spreading-solution resistance can be extracted from the graph as the section where the impedance converges to a single value over a range of frequencies. This is the resistive part of the graph and as such must be a serial combination of the solution and spreading resistances. As can be seen in the unsealed case, the spreading-solution resistance is not apparent at these frequencies, and due to the capacitance of the electrode interface, will require higher frequencies to measure accurately.

This may be sufficient to provide evidence that sealing is adding significant impedance to the device, but if accurate differences are required to be measured, then the solution resistivity could be increased, so that the spreading-solution resistance would dominate at lower frequencies.

The impedance models and testing procedures have been demonstrated for the ECoG electrode and a model for the sealing of the SPNI has been derived. The next chapter will go on to test the SPNI and validate the effectiveness of the sealing process.

CHAPTER 6

PREVENTING CURRENT LEAKAGE IN CHANNELLED NEURAL INTERFACES

The previous chapters have shown how an SPNI electrode array behaves mechanically and electrically. This chapter will go on to show how a PDMS layer can be incorporated into the SPNI with a view to sealing the channels, along with electrically characterising the electrode performance using impedance spectroscopy. It will then go on to put the impedance results in context by showing how this relates to signals sensed in adjacent channels.

6.1 Mechanism of Channel Crosstalk

The initial *in vivo* experiments preformed using the SPNI were conducted by surgically implanting the devices into the sciatic nerve of rodents and is outlined in chapter 2 and [25]. The research acted as an excellent proof of concept for the device, however, the lack of selectivity between channels of the device dramatically reduces the potential usability of the SPNI as a clinical solution.

In the study presented by FitzGerald (2012) 30% of the channels used to stimulate neural activity were found to trigger the same activity in one or more adjacent channels [25]. Along with this, significantly more current was required to drive the electrode during stimulation than would have been expected. These observations lead to the conclusion that the channel that was under stimulation was not appropriately sealed, thus allowing the current leakage between adjacent electrode sites. This in turn means that the stimulus selectivity of the device is reduced.

In a practical prosthetic, stimulation signals need to be specific enough to enable a patient to recognise the difference, for example, between a thumb and middle finger sensation. Uncontrolled crosstalk would considerably reduce the ability to distinguish such sensations.

Sealing the individual channels of the SPNI would prevent this current leakage and would also have a beneficial effect on the SNR of recorded neural activity. However, the limiting factor of the SPNI in its current stage of development is the lack of selectivity when stimulating, so this is the criterion that will be the main focus of this chapter.

The issue that allows channel crosstalk can be seen in figure 6.1. The channels highlighted green show how the tops of the channel layer for each channel are flush to the back on the substrate layer in the next roll. This kind of channel accounted for the 70% of channels that could only be stimulated by one electrode [25]. The channels highlighted in red however show examples of channels that do not sit flush to the substrate layer, leaving large open gaps through which electrical current could easily flow. This lack of adequate sealing is the reason for the current leakage which causes the interchannel crosstalk.

6.2 PDMS Sealing of the SPNI

In order to prevent this leakage a PDMS layer was included in the SPNI design, on top of the channel layer. It has already been shown that including this layer within the SPNI is possible structurally, and now the PDMS layers performance as a sealing layer will be determined.

A batch of eight SPNIs were made as described in the chapter 3, two of which survived to final testing. These two were bonded to their PCBs and sealed. The seal was made by using a 20 μm PDMS film fabricated as in chapter 3. The SPNI was soaked so that it sat

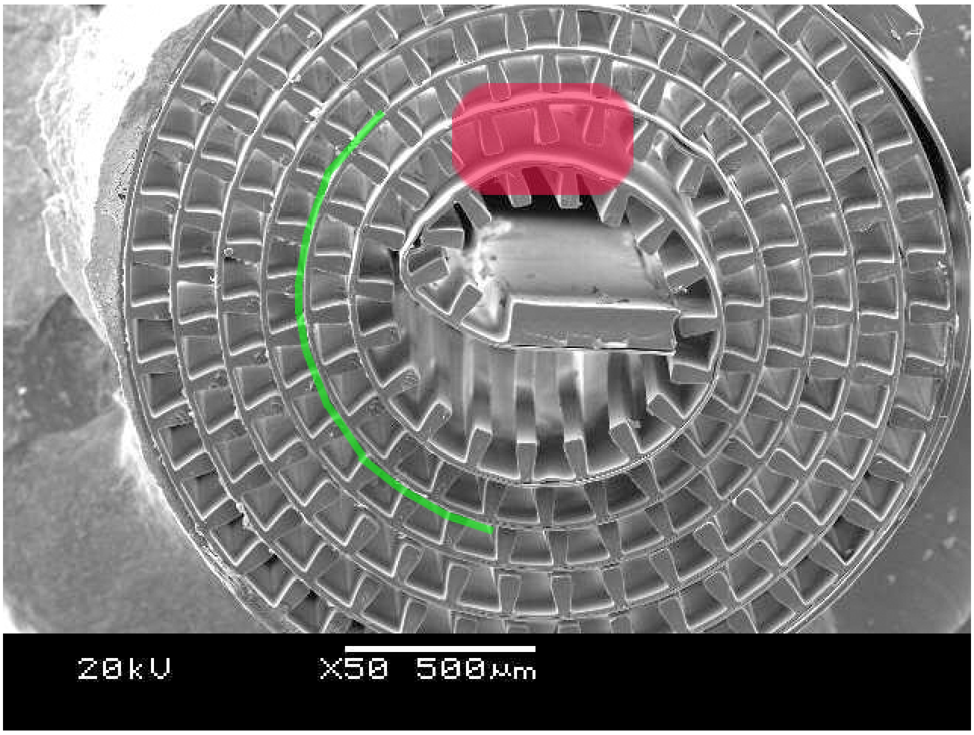

Figure 6.1: Adapted from [31]. SEM of the SPNI as presented to a nerve. The individual channels down which nerves will regenerate can be seen. The channels contained within the red section show an extreme example of how the channels do not form tight seals within the coil. The green highlighted section shows a good seal and an example of where the proposed PDMS layer will reside, providing augmented channel insulation.

in a pool of IPA, the PDMS was then floated on top of the IPA and gently maneuvered over a section of the SPNI that was to be sealed. The IPA was left to evaporate which allowed the PDMS to mate with the SPNI. This created a good bond between the two polymers. Any excess PDMS was cut away using a sharp scalpel. The quality of the seal placement was assessed under a microscope and the SPNI was rolled, resulting in devices such as those seen in figure 6.2.

In order to ensure like for like comparisons for the experiments, due to inherent variability between batches, each device was only partially sealed, so that each device would have around ten channels which were sealed and ten channels which remained unsealed. The seal placement is shown in blue in figure 6.3.

A small amount of silicone was smeared along the neck of the devices so that breakage would be less likely during testing. During previous testing it was observed that the SPNI necks would fracture at the points indicated in figure 6.3, due to concentration of stress at the points of the corners.

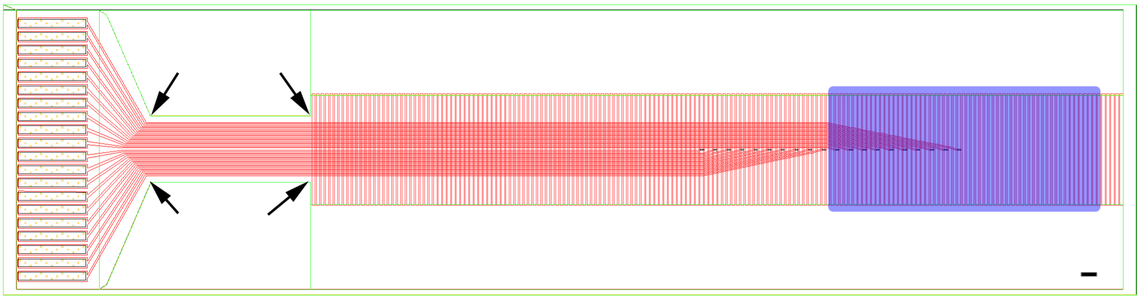

Figure 6.3: The SPNI was partially sealed as shown by the blue section, representing the PDMS sheet. The arrows show possible stress concentration regions where breakages were common. Scale bar is 630 μm.

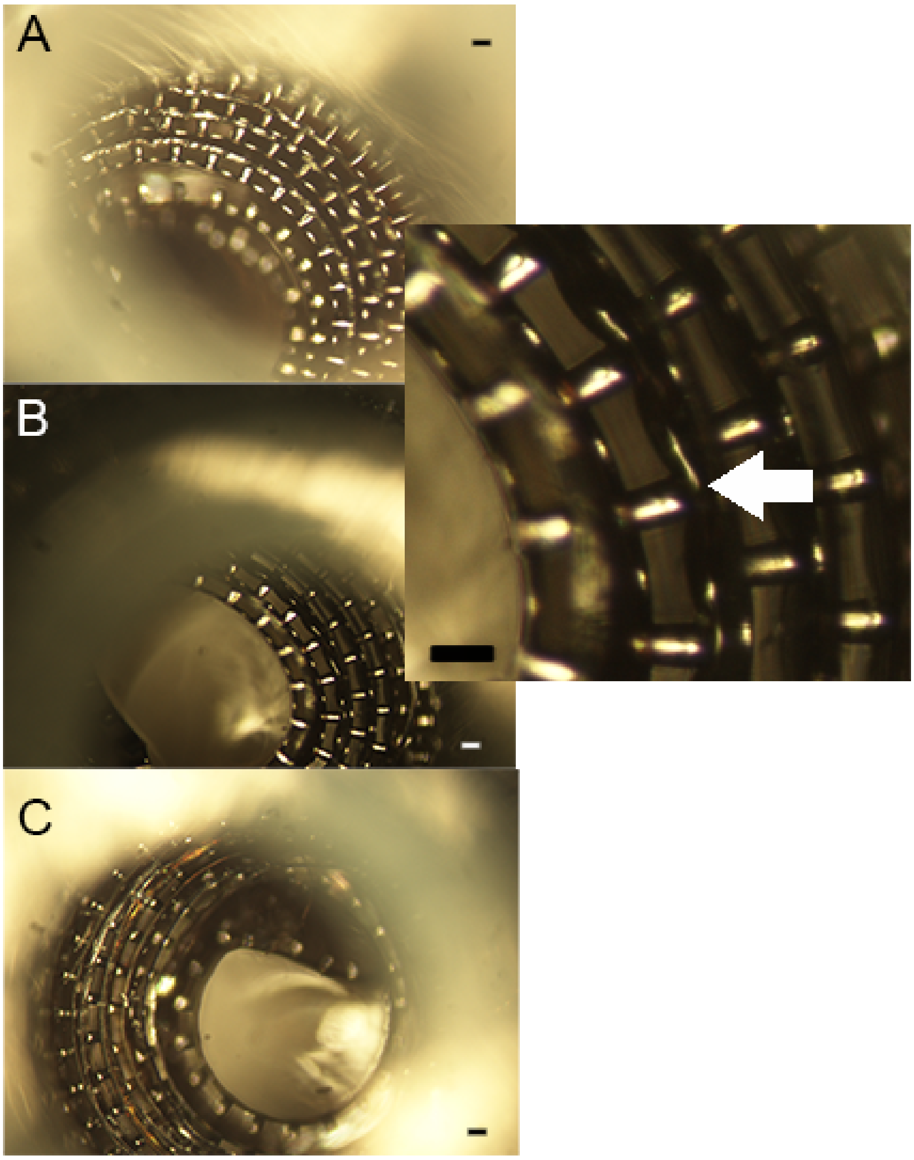

Figure 6.2: Images of the SPNI sealing under a microscope, demonstrating how the PDMS layer is pulled taut across the channel openings. Scale bars are approximately 100 μm.

6.3 Characterisation of the Array in Benedicts Solution

In order to measure the impedance of the SPNI, the channel needed to be filled with the solution of interest. Simply submerging them would produce an airlock within the device, preventing electrolyte flow. The two SPNI devices were filled with Benedict's solution by placing one end of the SPNI in solution and allowing capillary action to draw the fluid up through the device. This process was observably complete within two or three hours, but was left overnight to be sure that the fluid had risen all the way up the channels. This was confirmed under a microscope before testing.

Each SPNI was then submerged in fresh Benedict's solution so that any concentration change due to solvent evaporation would have minimal effect. The neck of the device was carefully kept out of the solution to avoid any shorting of the PCB contacts. The impedance tests were then carried out as with the ECoG devices, with each channel of the SPNI tested against the platinum counter placed a fixed distance away in the bulk of the solution (approximately 2 cm). The results of which can be seen in figure 6.4, typical values of which can be seen in figure 6.5.

The average impedance results for one of the partially sealed devices in Benedict's solution can be seen in figure 6.6. All impedance measurements of the unsealed channels were within ±8% of the average impedance value, however the sealed channels had considerably greater variation, which is indicative of the sealing quality not being consistent across the device, with the maximum values being well sealed and the minimum values being the worse sealed channels, the spread of the sealed results in comparison to the non-sealed results can be seen in figure 6.4.

The figure shows the characteristic capacitative behavior at low frequency, with impedance inversely proportional to the frequency. The solution resistance from these measurements was difficult to detect due to the high frequency problems predicted in the previous chapter.

These results do show that sealed channels offer higher impedance than non-sealed

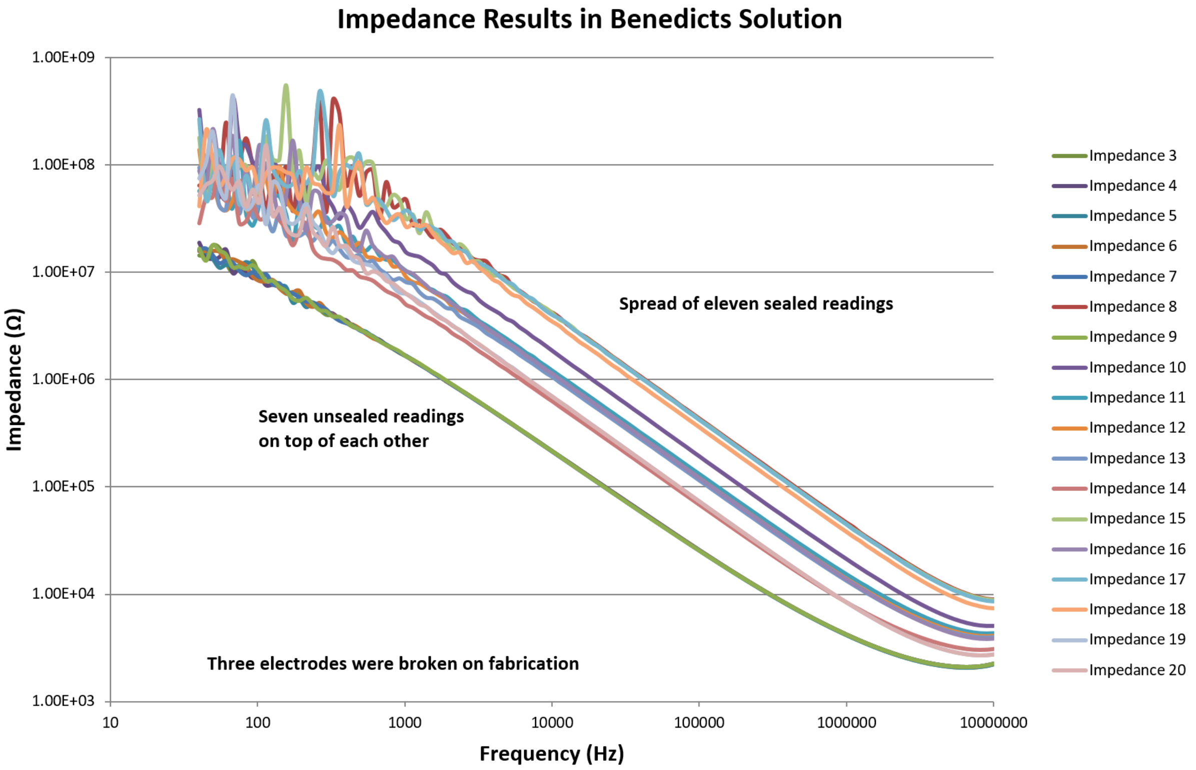

Figure 6.4: Impedance results of an SPNI in Benedicts solution showing how tightly clustered unsealed impedance profiles are in comparison to the wide spread of sealed channels.

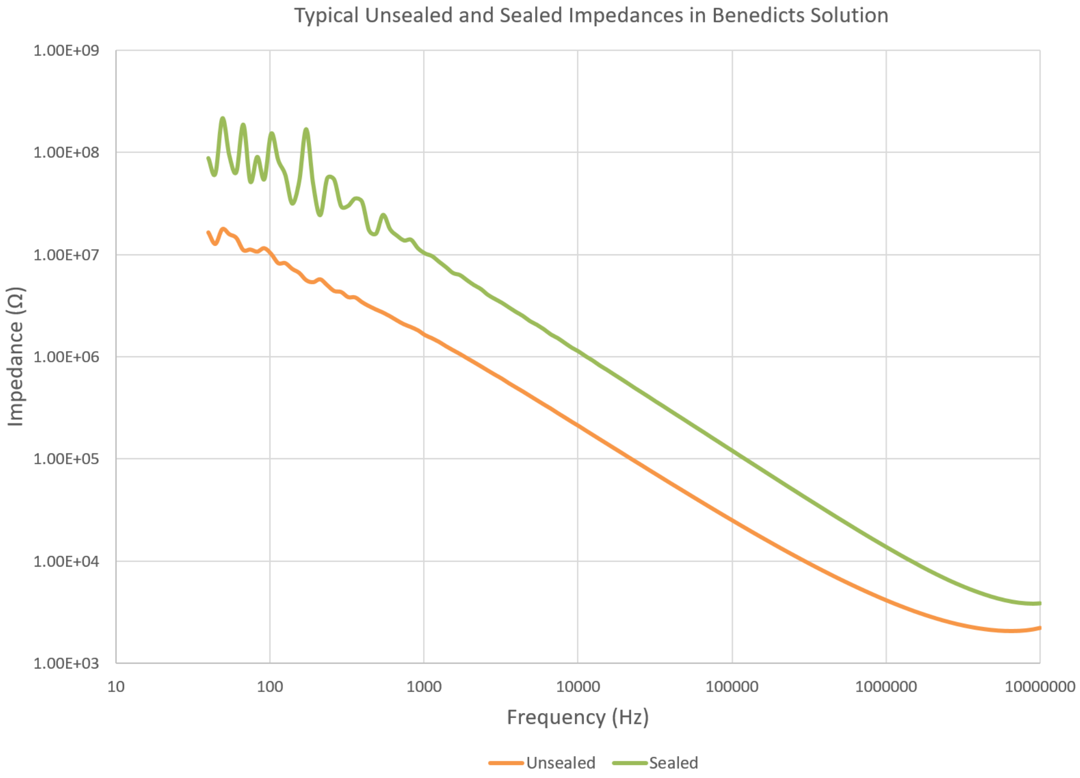

Figure 6.5: Extracting a typical unsealed and sealed case of an SPNI electrode in Benedicts solution.

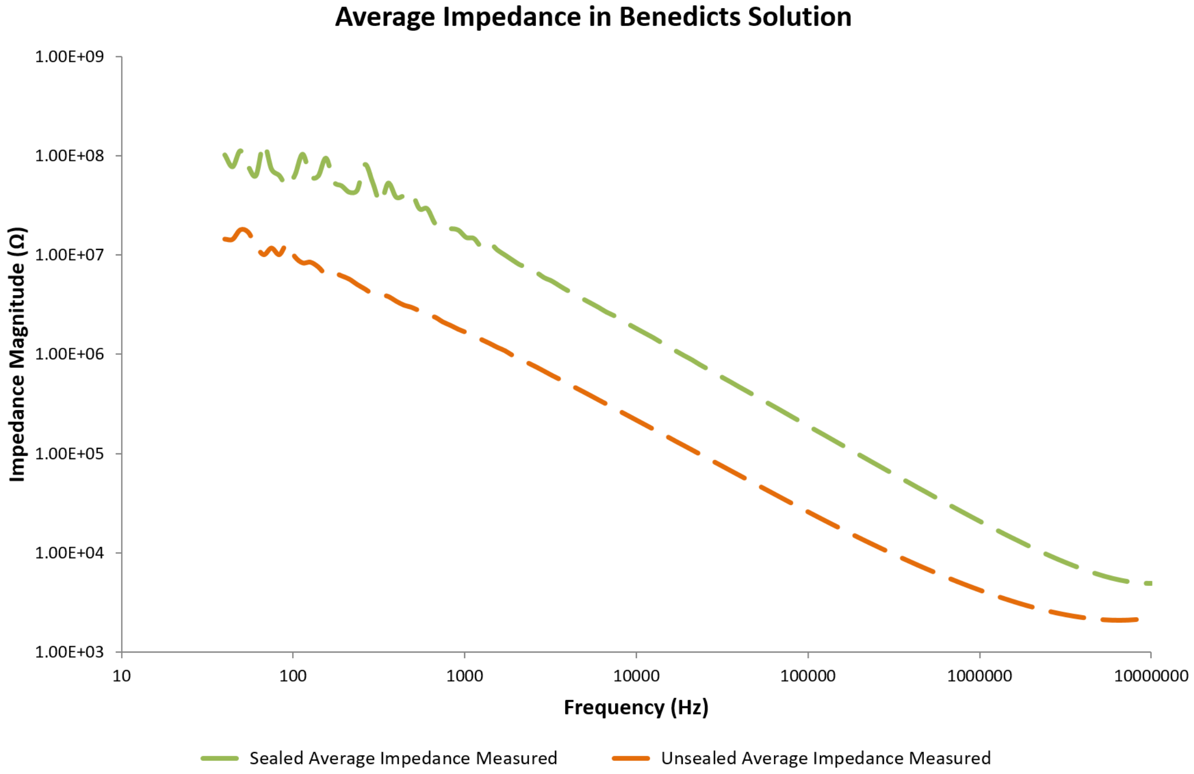

Figure 6.6: The average impedance profile of a unsealed and sealed SPNI channel in Benedicts solution.

channels, however they do not fit exactly with the expected results. The sealed result has considerably lower impedance when entering the resistive frequencies than expected, and the two results remain in parallel with each other at low frequencies which is also contra to expectations.

Although proving that sealing does have an effect on the electrode impedance of the SPNI, further investigation into the nature of the interface is required.

6.4 The Effect of Sealing on Electrode Impedance

In order to gain a better understanding of the electrode operation within the SPNI the solution was switched to RO water, instead of Benedicts solution. This would not test the device in a solution in which the SPNI is intended to operate, but would form a good test to whether the impedance increase caused by the sealing would be effective. The resistivity of the RO water used was 1.8 kΩm, and was measured using a hand held conductivity meter.

The impedance measurements in RO water can be seen in figure 6.7 for the first SPNI tested and figure 6.10 for the second. With typical values of the first and second devices shown in figures 6.8 and 6.11 respectively.

The average values of the impedances can be seen in figures 6.9 and 6.12. These have been cut off above 25 kHz to remove any results caused by the parasitic set up impedance.

These results clearly show that the sealed channels have significantly higher impedance across the spectrum when compared to the non-sealed channels. It also shows however, that the two impedances continue to run parallel with each other over the entire spectrum. This is in contrast with what is expected; that the impedances would only to diverge from each other when hitting the channel or solution resistance.

The devices were also tested in RO water prior to rolling to note how their impedance changed during the process, results of which can be seen in figure 6.13. The electrodes prior to sealing were classified to be sealed or to be left unsealed. As seen in the graph both sets

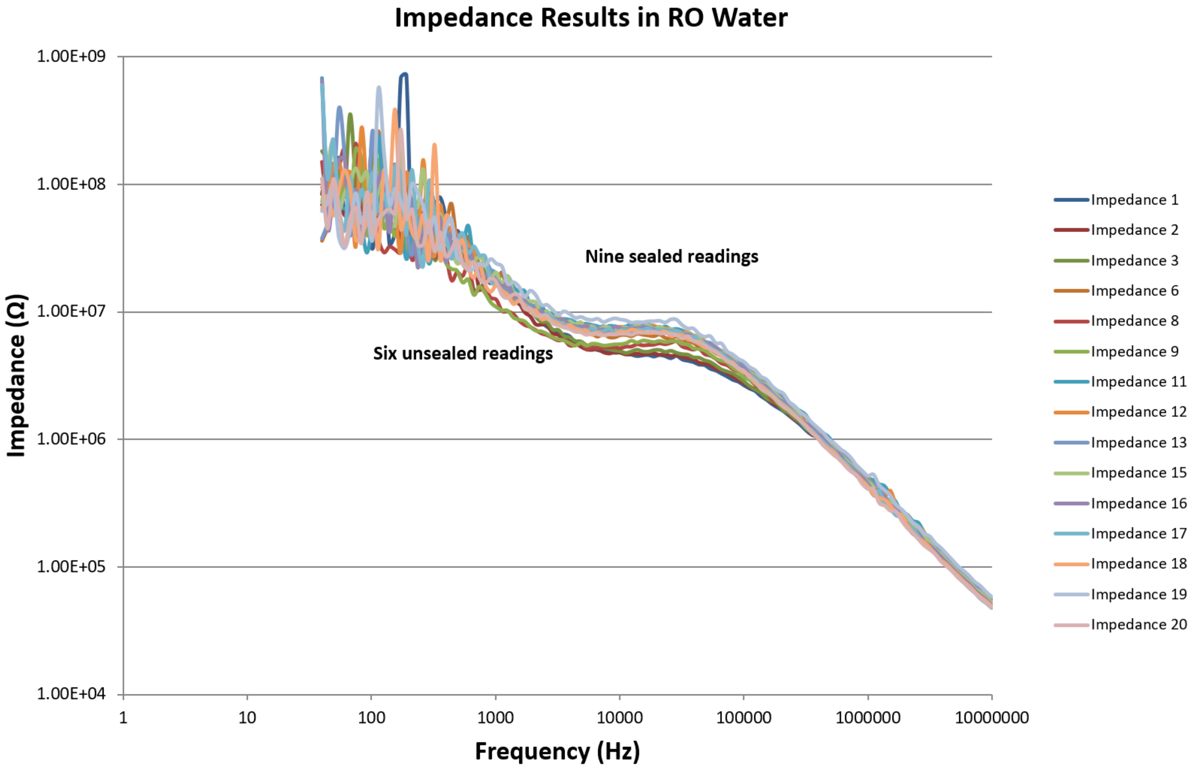

Figure 6.7: Impedance measurements for the first device in RO water.

of electrodes had very close average impedance levels. The sealing layer was then applied to the relevant channels and re-tested. This significantly increased the impedance of the electrodes, however the resistive part of the result was difficult to measure, appearing to be at around 2 MΩ. The devices were then rolled and re-tested, and a dramatic increase in both sealed and unsealed impedance is noticed, along with this the difference between sealed and unsealed impedances also increases.

This supports the hypothesis that the PDMS film is sealing the channels, and is then being pushed down on, or stretched across the channel to form a better seal once it is rolled.

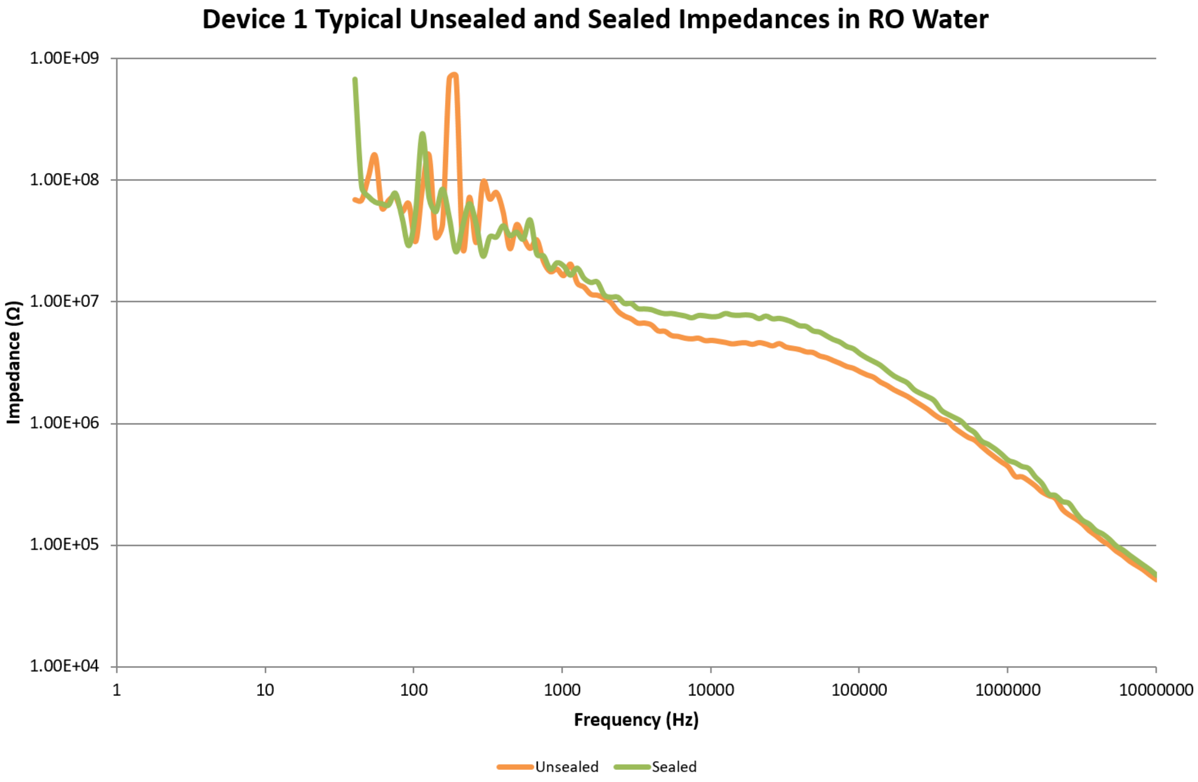

Figure 6.8: Typical impedance values for the first device in RO water.

6.5 Analysis of Impedance Results

The data gathered clearly shows that the impedance of the microchannels can be increased with the use of PDMS films. It shows that the act of sealing is superior to simply rolling the SPNI. The measured change however, is not as large as would be expected. With the channel geometry and solution resistivity of RO water used being 1.8 kΩm, you would expect a $R = \frac{\rho l}{A} = 480$ MΩ increase. Instead there is a 2.21 MΩ increase for the first SPNI and a 2.91 MΩ increase for the second. This difference between the two devices can be explained by variable sealing quality between devices. It is also unlikely that samples will be perfectly sealed, which would dramatically decrease the impedance of sealed samples across the board. Another factor which would decrease the expected impedance change is the contamination of the SPNI with the residue of Benedict's solution from the initial impedance tests, as there was no way for the salts in the solution to leave once they were inside the channels. When RO water enters the channels again, the salts may

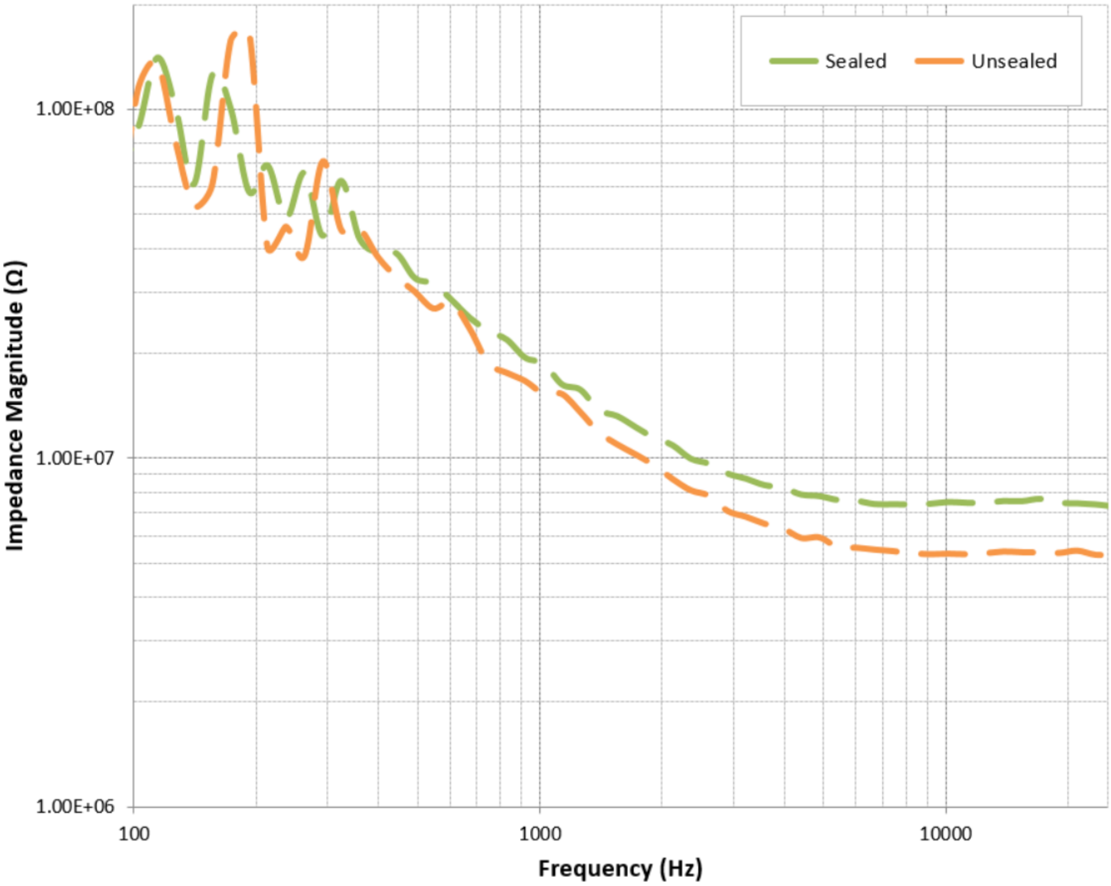

Figure 6.9: Average impedance profile of the first rolled SPNI in RO water, demonstrating the sealed and unsealed channel impedance averages. It can be seen that the addition of the sealing layer increases the resistive part of the graph which demonstrates the increased resistance.

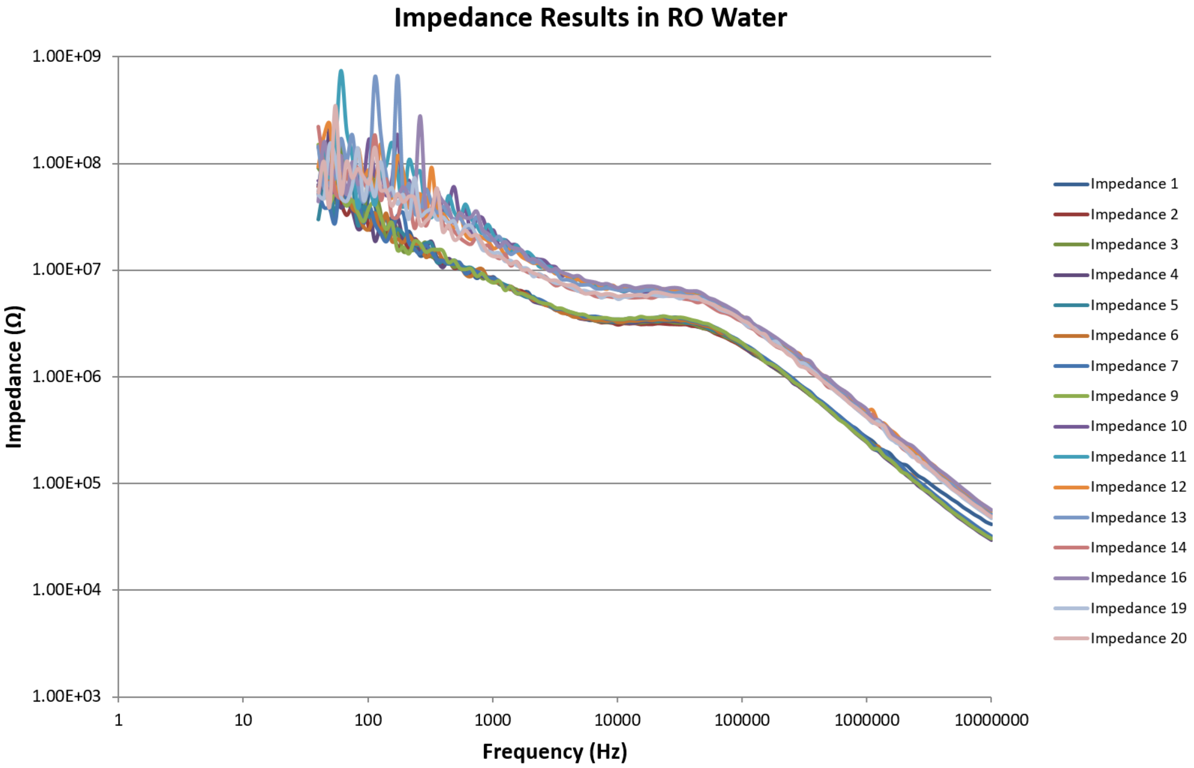

Figure 6.10: Impedance measurements for the second device in RO water.

contaminate the solution and reduce the resistivity of liquid within the channels. The fact remains however, that the data proves that significant and consistent increase in electrode impedance can be achieved by sealing the channels with a PDMS membrane.

Extracting the interface capacitance from the two devices it can be seen that sealing the device has an effect. The two devices give an unsealed capacitance of 0.1 pF and 0.2 pF with the sealed devices giving a capacitance of 8 pF and 9 pF, a large increase. All of these values however are less than the estimated 0.4 nF using the Helmholtz capacitor model. This decrease in capacitance can be caused by either a decrease in electrode area or dielectric constant of the water, or an increase in the separation between the metal surface and the outer Helmholtz layer. The area of the electrode is fixed and measured to be accurate. Surface roughness can alter the affective surface area of an electrode, however this always increases the area, which is not what has happened here. The dielectric constant used was 6, which assumes that only two molecules of perfectly aligned water

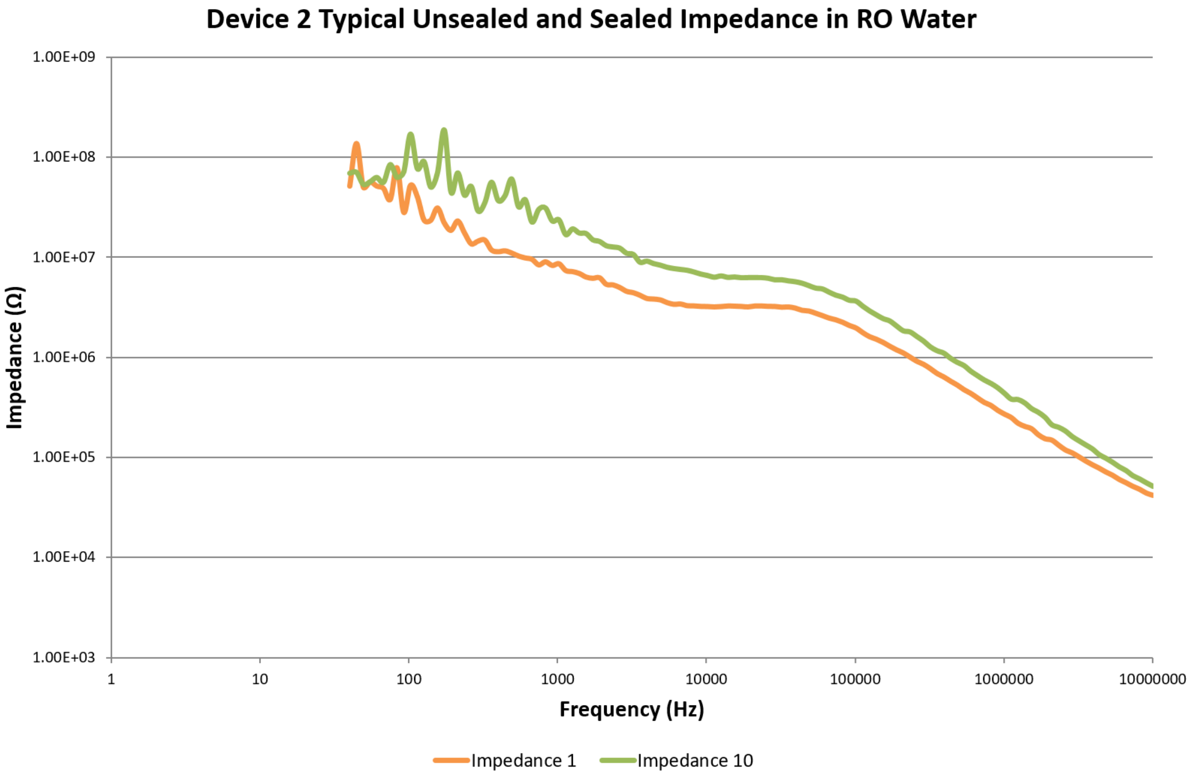

Figure 6.11: Typical impedance values for the second device in RO water.

are between the metal and the outer Helmholtz layer [79], this therefore cannot be any smaller in a physically realisable system. Therefore the separation between the metal surface of the electrode and the OHL must be around 19 nm which is significantly larger than the estimated 5 nm [79]. This may be due to contaminates on the surface of the electrode not being fully removed during the cleaning processes, this would leave a small residue on some parts of the electrode that could account for this increase of separation.

The spreading-solution resistance for the unsealed samples were 5.3 MΩ for the first and 3.35 MΩ for the second, rising to 7.51 MΩ and 6.26 MΩ when including the channel resistances for the sealed cases. The unsealed spreading-solution resistance for a rectangular electrode in RO water would be expected to be around 13.4 MΩ. This difference can be accounted for by the contamination of the device with saline in the channels of the device, resulting in a significantly reduced resistivity inside the channel. The geometry of the channels may also have an effect on the spreading resistance, as the SPNI tends to

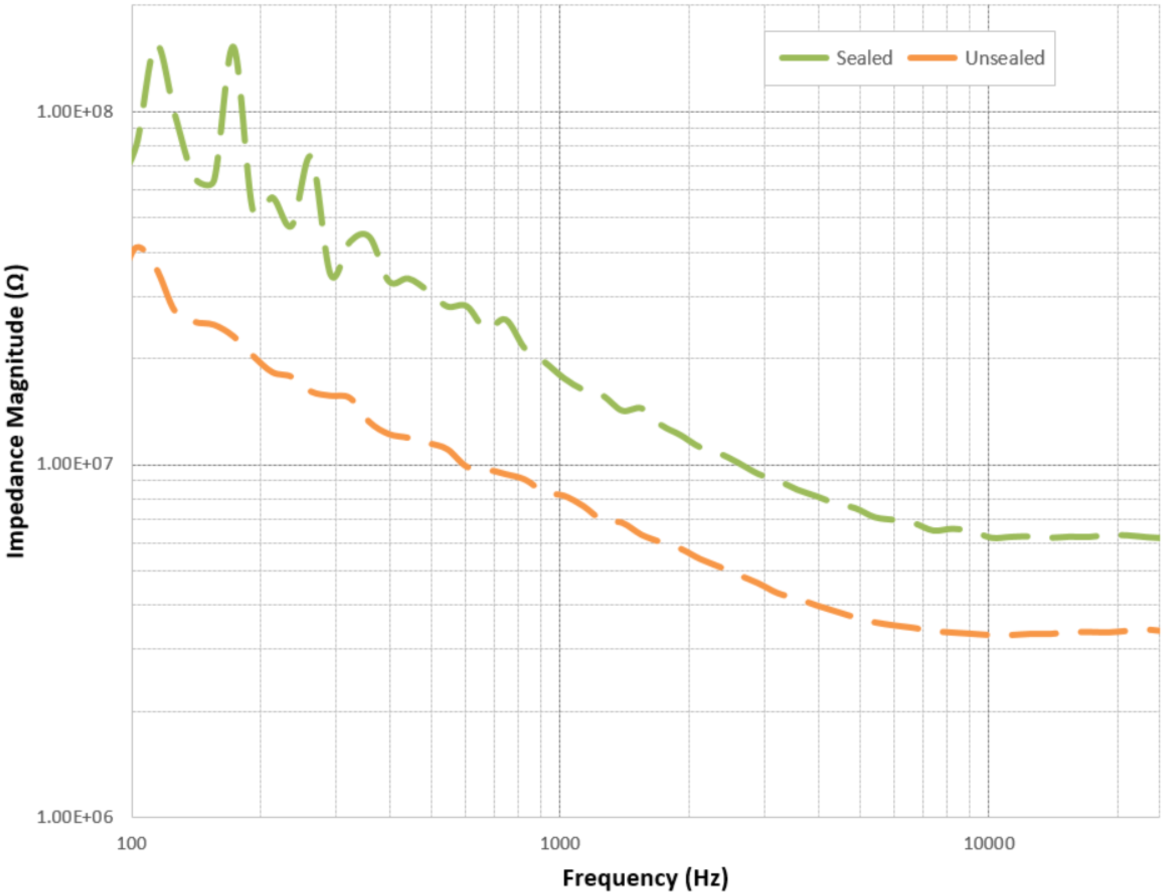

Figure 6.12: Average impedance profile of the second rolled SPNI in RO water, demonstrating the sealed and unsealed channel impedance averages. This sample too demonstrates an increases resistance with the addition of the sealing layer.

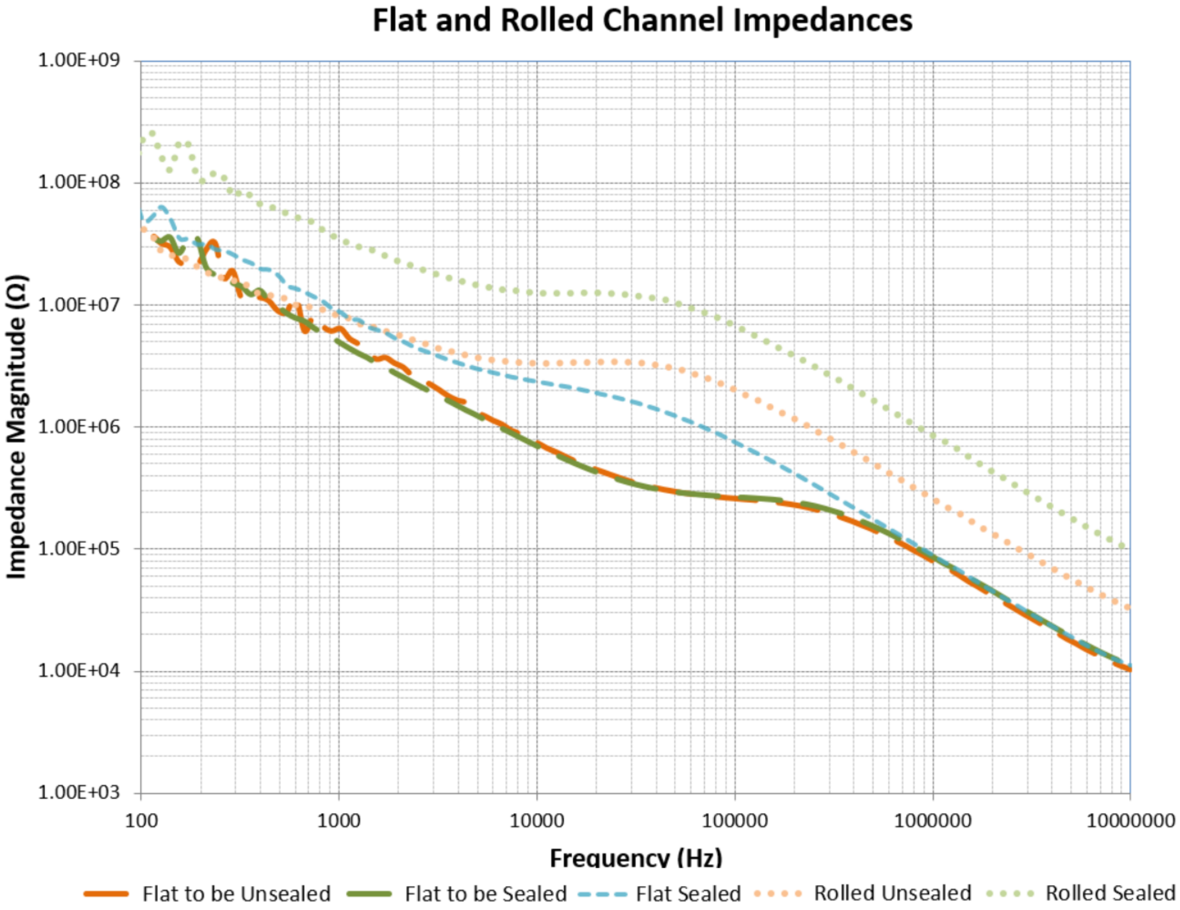

Figure 6.13: Impedance results showing how the rolling and sealing process affect the impedance of the electrodes within the SPNI.

curl even when not rolled, the curving of the electrode could affect the way current leaves it and therefore its impedance.

The data from RO water measurements in figure 6.13 also show a large and consistent roll off of impedance when the frequency goes over 25 kHz along with the impedances consistently running in parallel in the capacitive regions of the graph between rolled and unrolled electrodes. These discrepancies from expected readings are a result of the parallel combination of the parasitic impedance described in chapter 5 and the interface capacitance. This can be proven by adding in the parasitic capacitance to the model of the electrode impedance.

The data taken of the parasitic effects when using the 1 MΩ resistor in chapter 5 can be used to extract a characteristic impedance profile of the parasitic elements in the test chamber and PCB. This is done by assuming that the parasitic component runs in parallel with the impedance measurement setup. Therefore it can also be assumed that in the 1 MΩ test measurement, the parasitic impedance also ran in parallel, as in equation 6.1.

$$\frac{1}{Z_t} = \frac{1}{Z_p} + \frac{1}{1 \times 10^6} \tag{6.1}$$

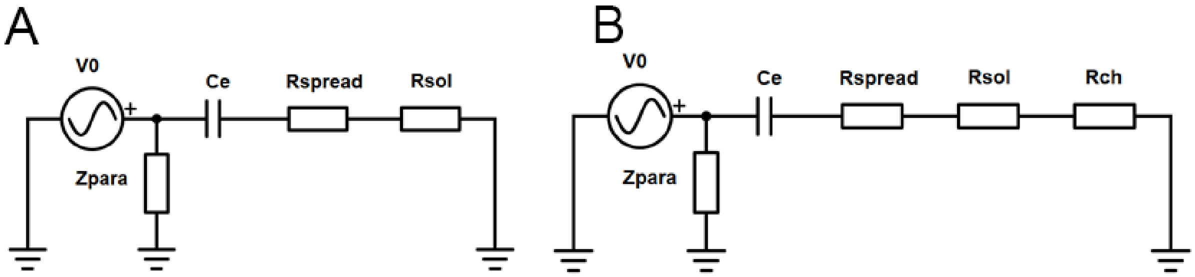

Figure 6.14: The circuit used for the theoretical model and how the addition of the sealing adds a channel resistance.

Therefore we can get equation 6.2.

$$Z_p = \frac{1 \times 10^6 Z_t}{Z_t - 1 \times 10^6} \tag{6.2}$$

Where Z_t is the measured impedance of the 1 MΩ resistor and PCB parasitics, Z_p, at a particular frequency. This was then used over all of the frequencies from the measurement to extract the parasitic impedance, isolated from the 1 MΩ.

This was then included in the impedance model as can be seen in figure 6.14. Doing this yields figure 6.15, with the values used presented in Table 6.1. The modelled values appear to be nosier than the measured values; this is due to the noise from including the parasitic results extracted from the measured 1 MΩ resistor.

The addition of the parasitic impedance helps explain some of the differences between measured and modelled impedance spectra. The theoretical perfectly sealed case still dramatically exceeds all other values, however, this is not considered to be representative of the seal achieved within the SPNI. The ‘Sealed Fit’ plot in figure 6.15 was acquired by reducing the channel resistance until the model fit to the measured data and shows the model when the channel resistance is 2.91 MΩ. This suggests that the achieved level of

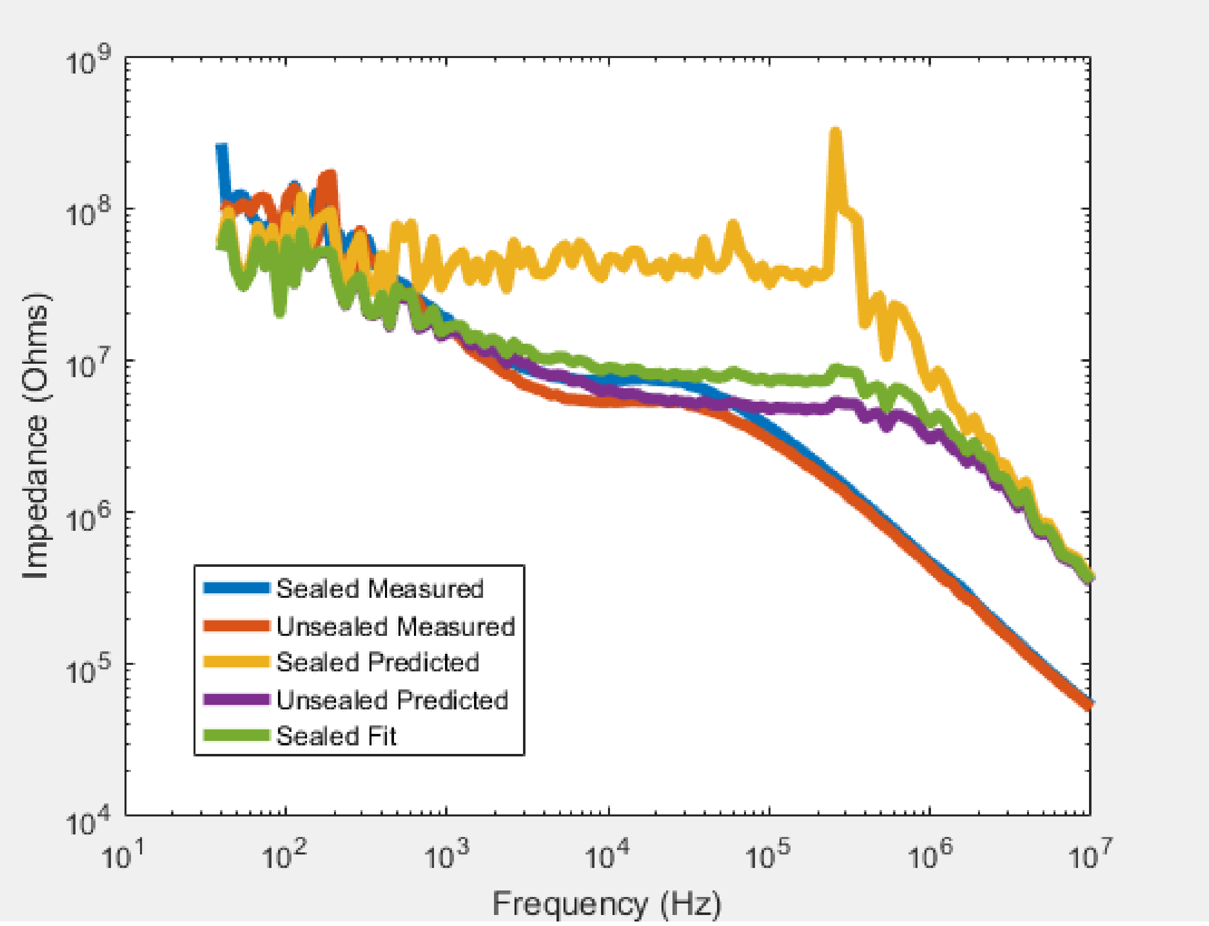

Figure 6.15: The updated model showing sealed, unsealed and partially sealed channels next to the measured data, all in RO water.

Table 6.1: Values used in the modelling of impedance based on experimental results

Variable	Symbol	Value	Justification
Electrode capacitance	C_I	8 pF	Using the extracted capacitance.
Bulk solution resistance	R_{sol}	0 ω	The resistance of the bulk solution is small when compared to R_{spread} and R_{ch} and so can be neglected from calculations.
Spreading resistance	R_{spread}	5.3 MΩ	Based of model fitting to the measured and predicted unsealed curves. Analytical solutions were not available due to the uncertain amounts of salt contamination within the channels.
Channel resistance initial value	R_{ch}	165 MΩ	Based on standard resistance equation $R = \rho \frac{l}{A}$, assuming ρ is 1.8 kΩcm for RO water used.
Channel resistance revised value	R_{ch}	2.91 MΩ	Based on fitting to the data. This value is much lower than the perfect value due to salt contamination and non-perfect sealing.

sealing afforded by the PDMS layer increased the channel resistance by around 2.91 MΩ.

Due to the parallel combination of the two capacitative paths, the modelled unsealed and sealed run in parallel when in the capacitive region under 10 kHz, but still converge at higher frequencies. It is possible to separate the two lines at higher frequencies and generally get a much closer match between the modelled and observed results by adding another capacitor in parallel with the circuit model. However, the source of this capacitance was not identified and so is omitted from this model. The addition of systematic parasitic impedance therefore explains many differences between modelled and measured results, further justifying the model here presented.

The model can fit even closer to the result if different values of capacitance are used for the sealed and unsealed cases, however, the mechanism for this remains elusive and so was also left out of the model.

The model fits to the data in two key ways: the rate of impedance decay at low frequencies is comparable, suggesting that the electrode impedance is modelled correctly, and the solution-spreading resistance inclusive and exclusive of the channel resistance is also comparable. The model loses validity over 25 kHz which suggests that the SPNI also has parasitic elements in its fundamental structure that have not yet been identified. However, the model can be used to predict electrode impedance below this frequency with an acceptable amount of accuracy.

6.6 Signal Transmission Testing

In the previous section it was shown that the impedance of a channel increases with the addition of a PDMS sealing layer. But to prove that this phenomenon is correctly understood and to ensure that the achieved level of sealing is appropriate for the SPNI's application; a second experiment was designed to test the sealing layer. This involved filling and submerging the partially sealed SPNIs in Benedict's solution. One of the channels was then stimulated. While stimulation was occurring, other channels which were close to the stimulus site were measured to see if significant signal crosstalk could be detected, and how this would vary between sealed and unsealed channels.

It would be expected that if the addition of a sealing layer were increasing the impedance between channels, then a smaller signal would be measured in adjacent channels when applying a stimulus to a channeled electrode, due to the decreased current flow between channels.

The experimental setup can be seen in figure 6.16. The SPNI was submerged in saline with the counter at a fixed distance of approximately 2 cm. A signal generator was used to supply a sine wave of 81 mV at 1 kHz to a selected channel. Signals in adjacent channels were then measured by passing the signal though a custom built instrumentation amplifier based around a INA111 chip (Texas Instruments), with gain 32, this was then fed into a standard laboratory oscilloscope (Tektronix) which was also used for data acquisition.

The data gathered was contaminated with low frequency noise, which made direct comparisons of magnitude difficult. To combat this, the signals were passed through an FFT algorithm using MATLAB and the magnitude at 1 kHz was taken. These were then plotted against the separation distance between the measured electrode and the stimulus electrode. Results of which can be seen in figure 6.17 and 6.18.

Figure 6.17 shows the voltage measured at unsealed electrodes was constant over the nearest three electrodes to the stimulus site. Unfortunately more data from consecutive channels was not available as some of the channels had broken in the unsealed section of the device. In opposition to this the sealed channel electrode voltages are lower than their

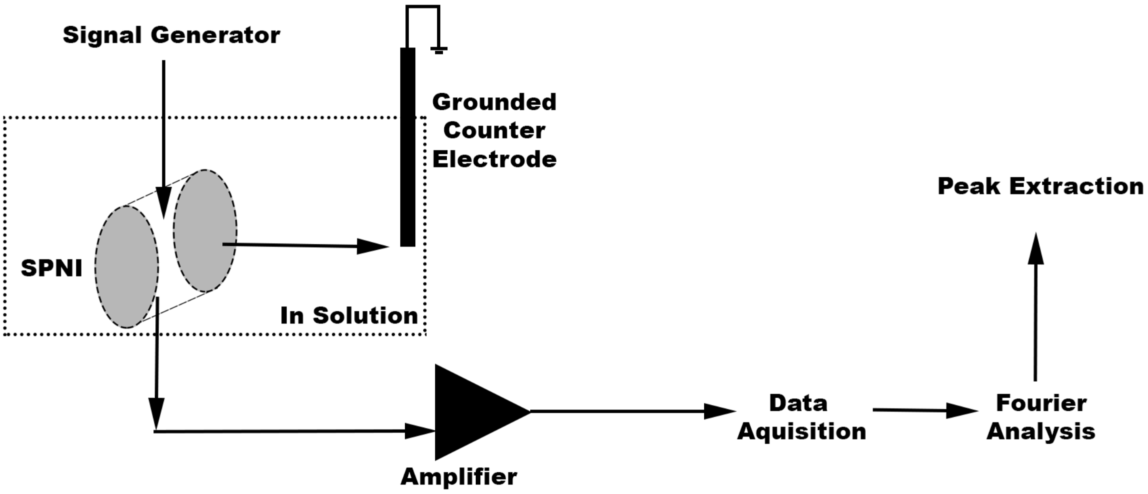

Figure 6.16: Showing the experimental setup of the signal tests. A signal generator provided a 1kHz sine wave which was fed into a SPNI electrode. The current would flow to a ground electrode in the bulk of the solution. Other electrodes in channels near to the stimulation site were then measured by amplifying any signal captured and digitizing using an oscilloscope. These results were then passed through a FFT and values at 1kHz extracted.

non-sealed counterparts and that they drop off very quickly with separation distance.

Figure 6.18 shows the same measurement but for the second device, however the unsealed channels provide a much higher measured voltage than those in the previous sample. These electrodes barely dropped in voltage at all and are extremely close to the amplified stimulus voltage of 2.6 V. The difference between the two sets of unsealed results can be explained by the difference in sealing quality (without PDMS) between the two devices.

As discussed at the beginning of this thesis, some of the channels naturally form better seals than others in a non-sealed rolled device. The sealing however is inconsistent and unpredictable. The inclusion of a PDMS insulating film however yields more consistent results across the two samples tested at considerably lower voltages than their non-sealed counterparts.

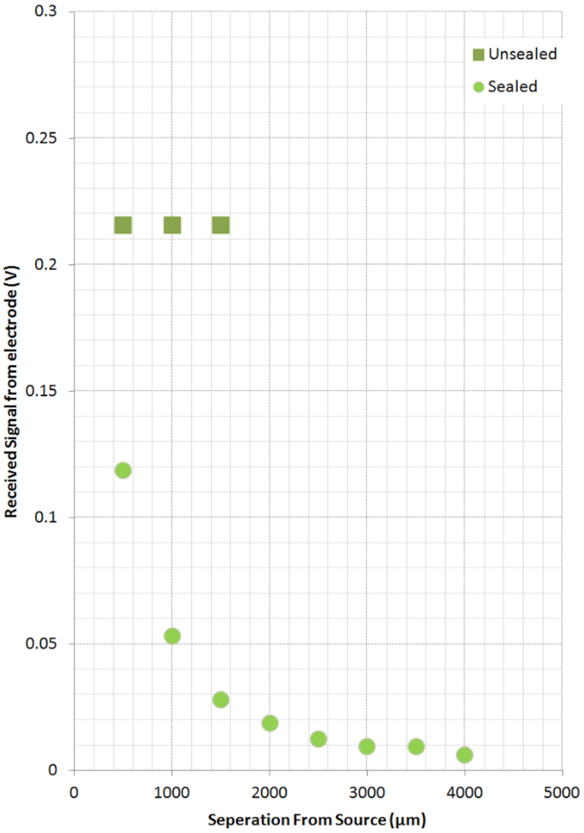

Figure 6.17: Crosstalk results for the first SPNI showing that unsealed results had significant attenuation from the stimulated electrode, however, between the measured electrodes the same potential was consistently measured. In the sealed channels however a significant drop can be seen in consecutive channels.

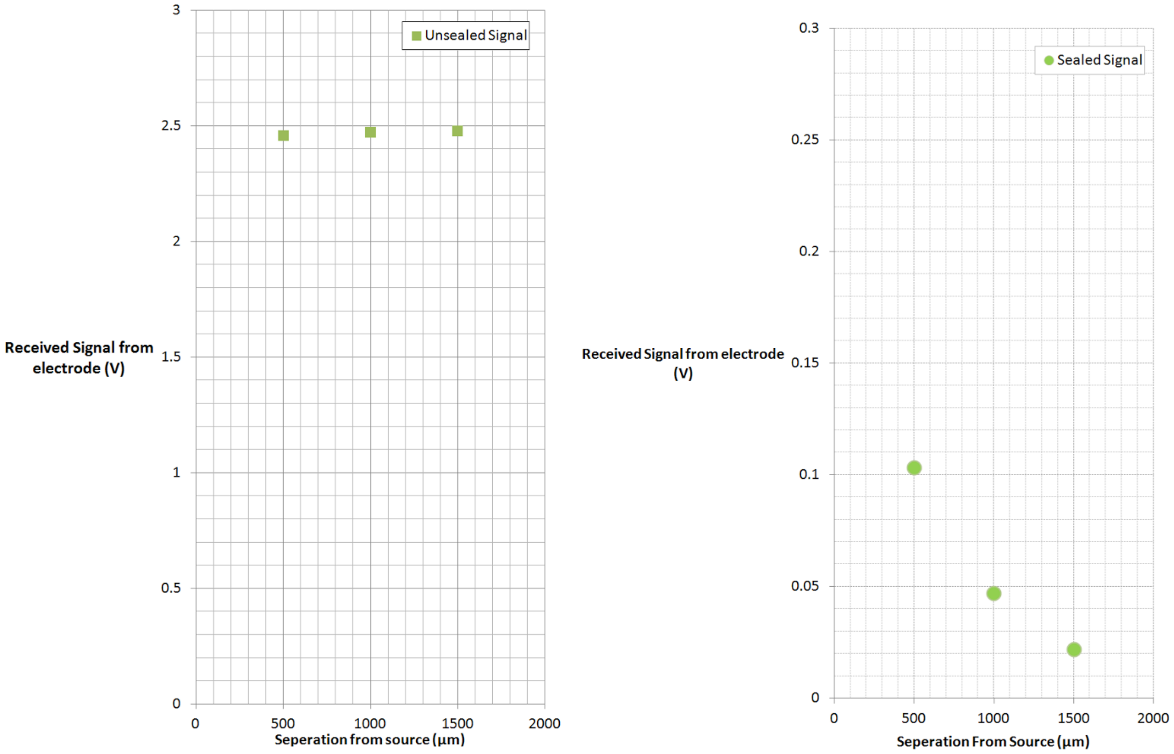

Figure 6.18: The crosstalk results for the second SPNI, like the first the sealing has had a significant affect on how the measured signal drops with electrode distance, however in this sample the unsealed results have barely dropped from the stimulus voltage.

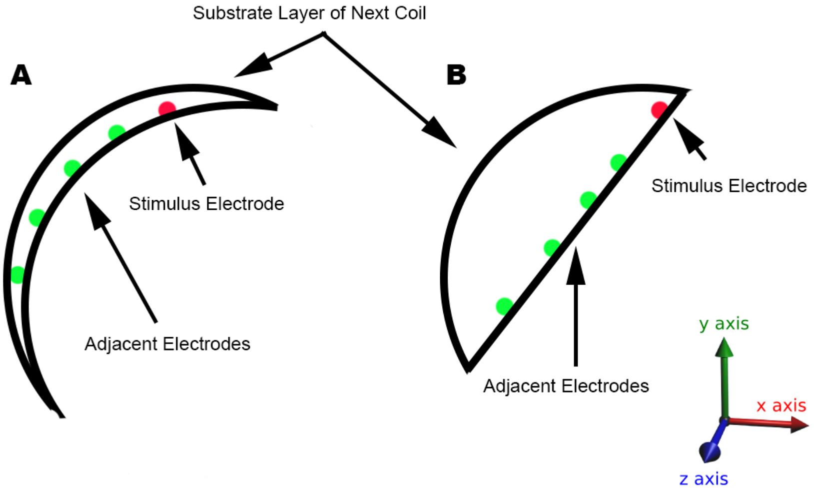

Figure 6.19: Showing how the geometry of a cavity within the SPNI can differ depending on how the roll forms between layers. The x and y axes are in the plane of the cavity with the z axis coming out of the plane of the image. (A) shows how a small cavity can be formed when the next roll has a substrate layer that falls in close proximity to the channel layer, and (B) shows how a large cavity can be formed when it lies back from the channel layer.

6.7 Signal Modelling of a Sealed Microchannel Array

The signal measurement results show a distinct difference in the behavior between unsealed and sealed measurements. These results can only be explained by two distinctly different modes of conduction occurring in the sealed and unsealed cases.

Conduction in the unsealed case

In the unsealed case a cavity is formed within the SPNI which can vary in geometry depending on how it has been rolled, as can be seen in figure 6.19. This allows low impedance pathways between electrode sites.

If a voltage is applied at the stimulus electrode, this will cause current to flow out of the devices, along the z axis of figure 6.19. However, as there is no current flowing in the x or y directions, a planar isopotential is formed.

The current flowing out of the device can be modelled by two parallel egress resistances in series with the electrode impedance, as in figure 6.20. This voltage across the electrode plane is a function of the cavity's cross sectional area, as R_{egress} is proportional to cavity

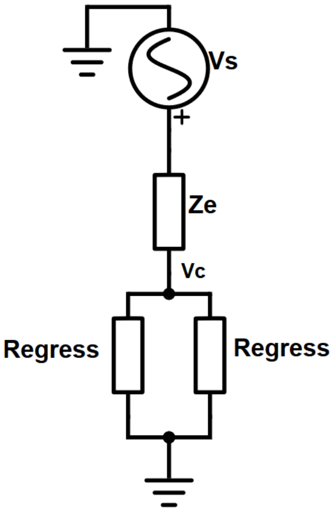

Figure 6.20: The equivalent circuit model of the unsealed device with the source supplied from the stimulation electrode traveling though the electrode impedance and then splitting between the two egress routes out into the bulk of the solution and down to ground.

area from Pouillet's law.

Figure 6.20 can be analysed as a potential divider to give equation 6.3.

$$V_c = \frac{R_{egress}}{2Z_e + R_{egress}} \times V_s \tag{6.3}$$

Where V_c is the voltage measured at a channel, V_s is the source voltage applied to the stimulus electrode, R_{egress} is the resistance of the path out of the device and Z_e is the electrode impedance.

From this model it can be seen that if the substrate of the roll is close to the channels, R_{egress} would be high, forcing the channel voltage to be close to the input voltage. This is what can be seen in the results from sample 2.

However, if the roll forms a large cavity, R_{egress} would be low, resulting in a low channel voltage, as in the results from sample 1.

Conduction in the sealed case

In the sealed mode however the current paths are completely different as the sealing layer makes all routes between electrodes high impedance. The current is therefore forced out

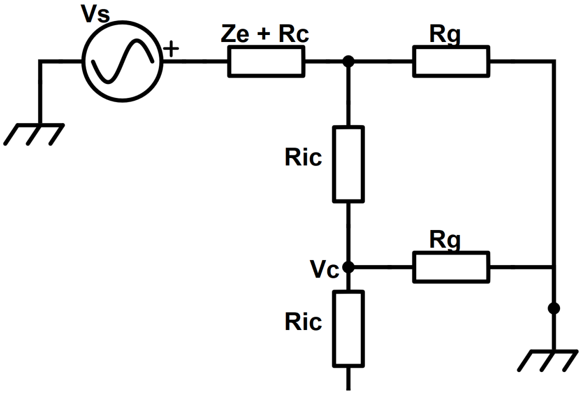

Figure 6.21: The equivalent circuit model of the sealed device where current from the stimulus electrode travels through the electrode impedance, is forced along the channel and out into solution where a small portion of the current leaks to adjacent electrodes with most of it traveling through the bulk to ground.

of the channels and into solution where it diverges to ground. Some of this current will alter the voltages of other channel apertures as it passes by. This can be modelled by a resistance network as can be seen in figure 6.21.

Where R_g is the resistance of the bulk solution down to ground and R_{ic} is the inter-channel resistance.

If this kind of network is applied the voltages at the channel nodes can be seen in figure 6.22, which has been generated from a MATLAB circuit simulation.

This is exactly the kind of relationship as was seen in the sealed cases of sample 1 and 2.

This shows that the act of sealing the channels changes the current paths within the SPNI in a manner that significantly reduces the current leakage into other channels and increases the reliability of the seal.

If the same benefits translated into *in vivo* experiments then the voltage contamination in adjacent channels would be less than 4.2 mV if a 20 mV voltage were applied in the stimulus channel. This is below the threshold voltage required to trigger an action potential in those channels, while still providing more than enough voltage in the stimulus channel to trigger an action potential.

This proves the validity of introducing the sealing layer and suggests that it would make a good addition to the SPNI design.

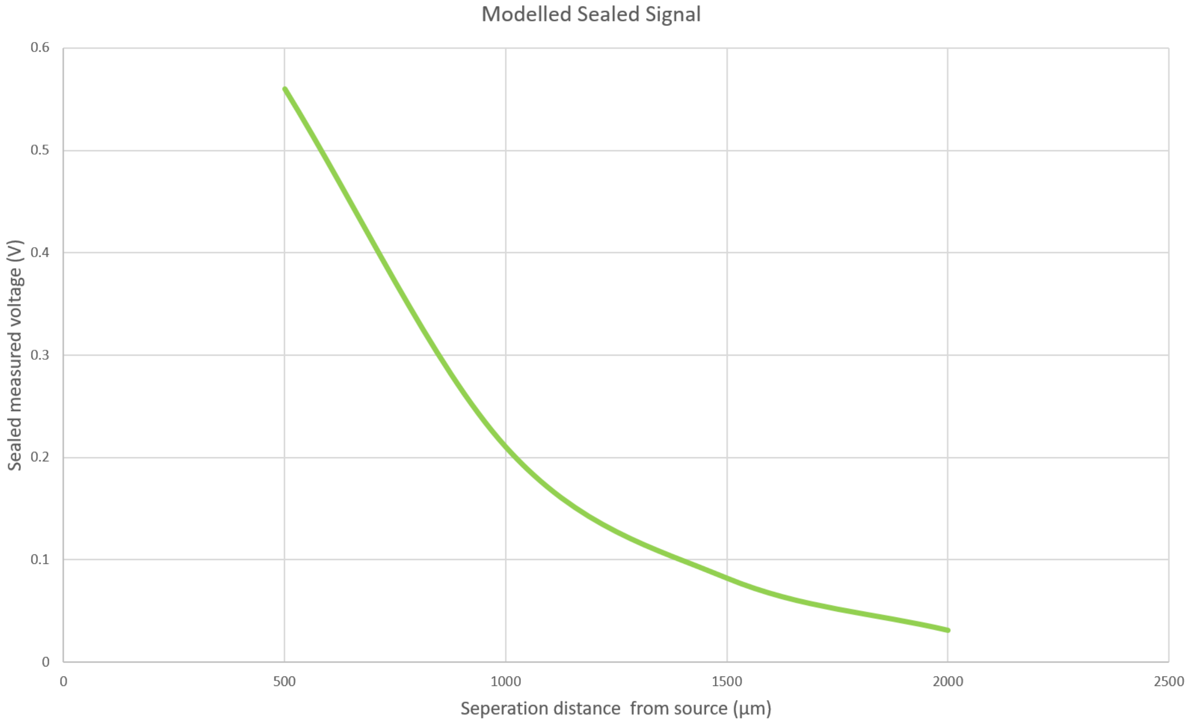

Figure 6.22: Graph derived from the potential divider model for electrode separation distance verses expected signal measured.

6.8 Sealing of Microchannels in Neural Interfaces

Current leakage has been a problem for the SPNI in previous studies and has resulted from the imperfect sealing of channels within the device. Resulting in the impedance between neighboring channels being low enough to allow current to flow to other electrode sites and cause the stimulation signal to be measured in other channels. This mechanism has been confirmed along with the fact that adding a PDMS sealing layer increases the effects of the channel resistance by well over 2 MΩ. It has also been shown that the added resistance is enough to reduce signal crosstalk in adjacent channels by at least 44%, up to a maximum of 96%, which is to an extent that would be advantageous in an *in vivo* experiment.

This new evidence suggests that one of the initial problems with the SPNI has been addressed, such that it will now preform more predictably and reliably when inserted into a nerve bundle. The addition of the insulation layer should give the SPNI much greater resolution when it comes to stimulating regenerated nerves, this will mean that the device can be much more selective when stimulating, and the sensing SNR should also be increased [25]. Bringing neuroprosthetics one step closer to a viable bidirectional neural interface.

There are still some barriers for the SPNI to overcome before it can be used in a clinical application. The final major issue is that of biocompatibility which will be explored in the next chapter.

CHAPTER 7

SILICONE SHEETS AS A CARRIER FOR ACTIVE AGENTS

The previous sections have focused on the inclusion of a PDMS layer into the SPNI and its effect on the electrical sealing of the device. This chapter however will go on to discuss other benefits of having silicone films present within implants. This chapter will demonstrate how drugs can be included in and released from PDMS and how they may be a route to increasing the chronic viability of neural interfaces.

7.1 Biocompatibility and Implants

A device or material is biocompatible if it is not toxic, injurious or negatively physiologically active and does not cause an immunological reaction. Hench et al (2002) defines several generations of biocompatibility based on the historical development of the field. The first generation of biocompatible materials were developed to replace biological materials while minimising their toxic and pathogenic effects [80]. This includes using only bio-inert materials such as gold and polyimide in implants. The second generation aimed to elicit a controlled mechanism within the body which would actively improve the physiological environment's response to an implant [81]. This includes drug delivery systems such as the one presented in this chapter [82, 83]. The third generation of biocompatible materials aim to modulate the bodies responses at a cellular and molecular level, including bioactive and resorbable materials. These materials are capable of biologically complex feats such as activating genes that stimulate regeneration [82], which may be particularly relevant to the future of neural interface technologies.

One of the fundamental limits on the use of neural interfaces is the body's reaction to foreign objects, as the immune system is designed so that alien objects within the body are continuously sought out and attacked by white blood cells. Biocompatibility is a problem for all neural interfaces, but is exemplified by the Utah array which is a brain computer interface currently licensed for use in human patients in the USA [84]. Even with its relative success, the Utah array causes serve scaring in the region of the brain in which it is implanted. This scaring is permanent and gets worse the longer the array is implanted. Through similar processes, the same effect is commonly reported for peripheral neural interfaces [23, 85].

The foreign body response is at least partially responsible for the issues with device longevity, as it causes swelling and inflammation in the short term and scaring along with mobility of the implant in the longer term. The swelling inhibits neural growth and prevents reinnervation, causing the viable distal nerve ends to deteriorate. It is common for implants to function for up to a few months before the negative effects caused by foreign body response gets severe enough to cause the device to fail.

The SPNI has already been designed to be first generation biocompatible, being made from polyimide and gold which are non-toxic materials approved for use in implants. However, the issue of biocompatibility still arises, and the difference in Young's modulus between the tissue and the implant causes long term compatibility problems.

7.1.1 The Foreign Body Response

A neural interface, once implanted within the body, is an irritant to the immune system and cannon be broken down as would normally be the case with an invading virus or bacteria. This will cause a fibrous capsule to form around that material, through the mechanism of the foreign body response.

The foreign body response occurs through five discrete stages, first proteins are absorbed into the surface of the implant, next acute inflammation affects the implant site, quickly followed by chronic inflammation, followed by foreign body giant cells which finally trigger the formation of a fibrous capsule around the implant where on-going reinforcement of the process continues. Each of these stages will be looked into in more detail [86].

With stage one, upon implantation, blood plasma absorbs to the implant materials and forms a protein matrix around the implant, which develops a thrombus. The cells responsible for the severity of the foreign body response, interact with this sheath rater than the implant surface. The protein composition of this matrix depends very much on the physical and chemical properties of the implant materials such as their wettability, topography, Young's modulus, surface chemistry and charge balance. The types and relative abundances of the absorbed proteins dictate monocyte adhesion and giant cell formation, as well as attracting mast cells which trigger the acute inflammation stage. It should be noted that mechanical stress caused by the relative motion of the implant to the body can exacerbate the foreign body response at this point by producing pro-inflammatory signals which encourage fibronic encapsulation. Hilborn (2007) states that increasing the biocompatibility of materials is likely to come from reducing the mechanical mismatch between materials and the body [87].

The amount of protein absorbed in stage one along with the amount of damage at the implantation site have a large affect on the acute inflammation stage which can last between hours and days. Polymorphnuclear leukocytes and mast cells release many inflammatory and signaling chemicals that attract the leukocytes which trigger stage three.

The third stage of the foreign body response, chronic inflammation, is characterised by the infiltration of lymphocytes and monocytes. These cells also increase the inflammatory response and break down any damaged tissue around the implantation site. These cells promote tissues regeneration, enhance capsule formation around the implant and try to engulf the implant. If the implant is persistently non-digestible, the monocytes produce chemical signals that trigger the formation of foreign body giant cells.

The fourth stage of the foreign body response is denoted by the formation of foreign body giant cells. In response to the signals from the chronic inflammation stage, macrophages begin to fuse together to form large multi-nucleated cells. These cells continue to attempt the digestion of the implant, however they also, through several signaling pathways, attract fibroplasts and endothelial cells to trigger the final stage. In the long term they also release potent chemicals that can degrade the implant.

In the fifth and final stage the fibroblasts and endothelial cells arrive at the implant site and begin to lay down collagen to form a peripheral fibrous capsule around the entire site. The continued presence of the implant maintains the presence of mast and giant cells which continue to provide chemical signals encouraging further inflammation and fibrotic stimulation.

All of these stages cause different problems for the functionality of the implant, the swelling around the implant limits the proximity to which the nerves can approach the device (thus reducing the signal to noise ratio) and the scar tissue retards neural regeneration, both issues prevent the adequate functionality of neural interfaces. The reactions to the biomaterial and the results in the tissue are summarised in figure 7.1 [88].

It is important to note that the composition of the neural implant materials determines how hostile the foreign body response will be to a given device. A compatible biomaterial must not only be non-toxic, but be physiologically non-reactive, have appropriate surface topology, relative elasticity, wettability etc. and this provides a significant problem for neural interface research due to the sensitivity of the implant to the foreign body reaction.

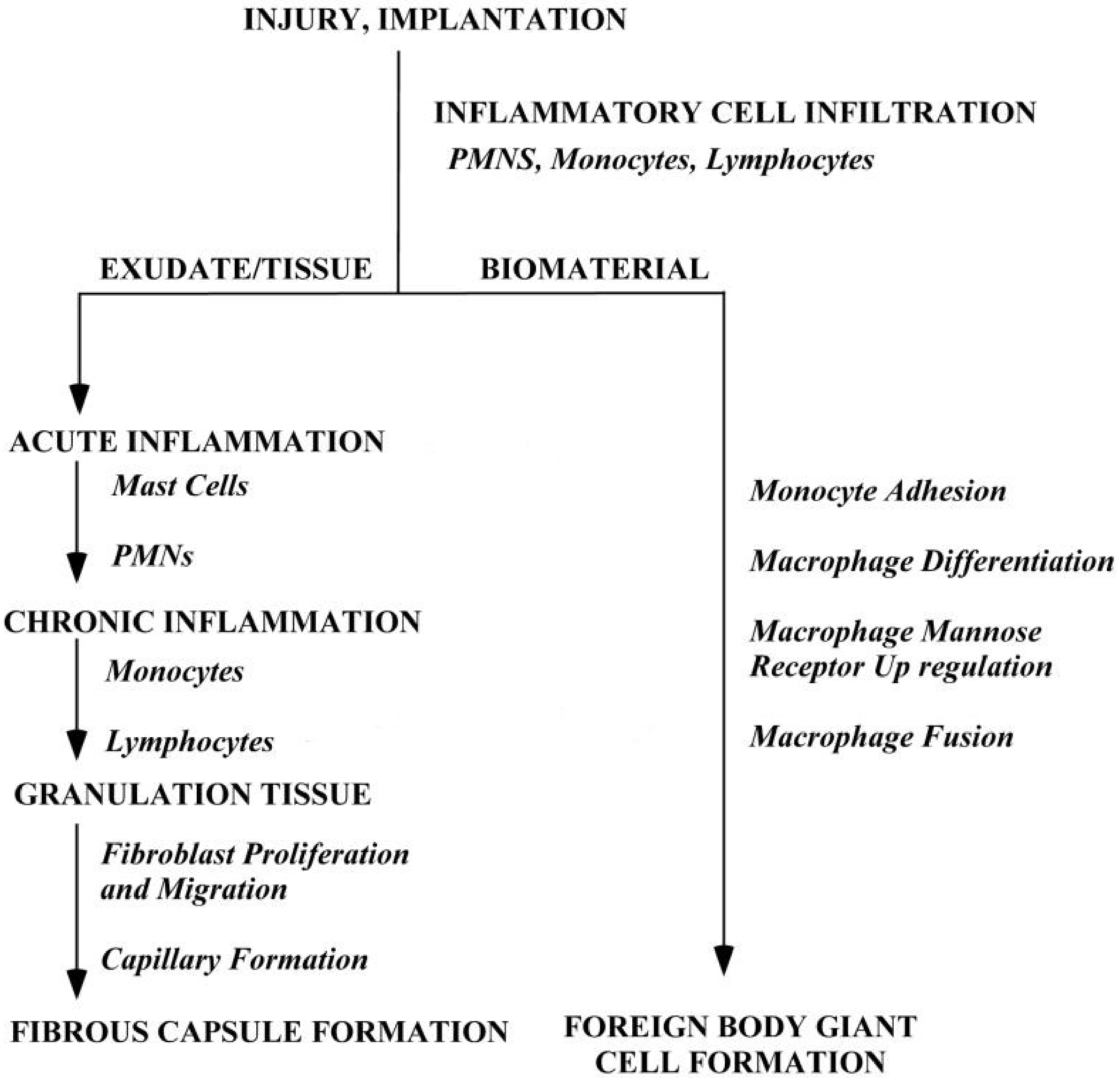

Figure 7.1: The process diagram taken from [88] showing the body's reaction to foreign bodies. The left track shows the reaction to the invasion in the tissue and the right track shows the response of the various white blood cells to the biomaterial.

7.1.2 Mitigation of the Foreign Body Response

It has been shown that the foreign body response can be mitigated with the use of ultra-complaint materials such as silicones [89–91]. However devices that are made completely out of silicone materials often require intricate manual assembly and a high skill level to create [25], making mass fabrication and quality control difficult, meaning that these silicone based devices are not a practical solution to the neural interface problem.

There are drugs that can be used to suppress the adverse reactions within the body, for long term use, however they need to be applied locally to the site of injury [92]. This thesis proposes the hypothesis that drugs can be included within the SPNI so that the foreign body response is suppressed at the implant site itself, thus elevating the SPNI from a first generation biocompatible device to a second generation biocompatible device, that is actively moderating the physiological environment.

7.2 Silicone as a Carrier

The idea of drug doped implants is not a new one and has been clinically used in devices such as heart probes and stents [93–95]. These devices, however, are large in comparison to the SPNI. They consist of a device coated in silicone, within the silicone is a small reservoir in which anti-scaring or anti-inflammatory agents are placed. The drugs have mobility through the silicone and slowly diffuse out into the surrounding tissue, applying their beneficial effects. Thus the silicone is applying two methods of increasing the overall biocompatibility of the implant, by coating the implant it is reducing the difference in Young's modulus at the material interface between the implant surface (2.5 GPa for PI and 320-870 kPa for PDMS) and the surrounding tissue (of the order of 1 kPa for soft tissues), and at the same time is secreting drugs that prevent the body reacting adversely to the implants presence.

The reservoir can take several years to deplete, protecting the patient from the negative effects of implants over that time period. In the heart probe example the effects of the steroids used can last up to 10 years [95], after which time the device can be replaced, or a simple surgery preformed to refill the drug reservoir.

Given the limitations on mass fabrication, making the entire device out of silicone is currently impractical. Mass production of silicone based devices may be possible in the long run, but currently most silicone-based devices being researched are one off prototypes that cannot be directly transferred into viable products for the prosthetics industry.

The previous chapter demonstrated how a silicone PDMS layer can be incorporated into the SPNI to improve the electrical isolation from one channel to another. This silicone sheet is much more suitable for manufacturing processes than most other silicone based neural components in the literature (exceptions to this are currently in development in the USA and will be presented in the next chapter). It might be possible therefore to incorporate anti-scaring drugs into this layer and achieve the positive effects of slow drug release over time, directly into the site of the implant. The PDMS layer covers every channel of the device in which nerves can grow. This would give a drug-doped PDMS layer ideal access so that the drug could be delivered directly to the center of the neural activity.

If this were possible then the negative effects of hard neural implants may be mitigated and the nerves may continue to function for longer periods of time.

7.2.1 Drug Delivery

If a high concentration of decorin is incorporated into the center of the device such as the SPNI or in the PDMS insulation layer, there is a concentration gradient between the high concentration of the drug in the PDMS and the edge of the device where the drug diffuses into the body. The rate of drug delivery can then be programmed by altering the concentration gradient or diffusion path. This kind of drug delivery into channels has been shown to be viable in simulations and prototypes [96].

7.3 Decorin as an Anti-Scaring Agent

Decorin is a complex protein that has shown positive effects on nerve growth in the brain and spinal chord [92]. Damaged nerves in the spinal chord find themselves in an environment in which it is very difficult to regenerate. There are many other support cells that, when damaged, prevent proximal nerve reinnervation at a suitable rate, resulting in neural degradation. However, decorin has been shown to dramatically improve the chances of successful reinnervation in such a hostile environment. It is thought therefore that applying decorin to the SPNI may have similar beneficial effects.

Decorin is a steroid which naturally occurs in the body and acts as an anti-fibroma agent, preventing scaring from taking hold of a treated site. Another drug which is commonly used in such investigations is dexamethasone [97], this is an anti-inflammatory agent. However at the University of Birmingham, there are researchers who specialize in the application and effects of decorin, therefore it was decided that in collaboration with the University's medical school a trial would be conducted using decorin as the active agent.

7.4 Decorin Integration

To test if decorin could be successfully integrated into the silicone sheets used in the SPNI, small amounts of the drug were mixed into the PDMS during film fabrication.

To fabricate the PDMS sheet, first a 3 μm layer of PMMA was deposited onto a clean silicon wafer. The silicone precursor was mixed with its cross-linking agent (both parts of Sylgard 184, Dow Corning) for 3 minutes and then left for 5 minutes for the bubbles that form to disperse. 1.5 ml of 5 mg/ml decorin solution was then added (this had been allowed to warm to room temperature before the experiment as it is stored at 3°C), mixed for a further 3 minutes and left to rest again for 5 minutes for the bubbles to disperse.

The decorin silicone mixture was then spun onto the PMMA treated wafter at 500 rpm for 30 seconds and then 1000 rpm for 1 minute. The wafer was then covered with a petri dish and left to set at room temperature for three days. The 20 μm thick silicone layer (as measured with a hand-held thickness monitor) required ambient water vapour to set, therefore the petri dish was raised at one end to allow air to exchange.

Once the silicone had fully cured, the wafer was submerged in isopropyl alcohol. This rapidly released the silicone sheet from the PMMA layer. There was concern over any interaction between the alcohol and the decorin, so it was ensured that the sample was in contact with the alcohol for no longer than 5 minutes total exposure time before gently rinsing with RO water. The PMMA treated wafer could be used again, without further treatment for a subsequent silicone layer.

One centimeter squares were cut out of the silicone sheet and placed into flat bottomed, bijou test tubes with screw tops.

In order to test if the PDMS process had averse effects on the decorin another kind of silicone (3140 RTV Coating, Dow Corning) was used as a carrier for comparison. Decorin treated RTV silicone was cast into a small aluminium ramekin out of which one centimeter squares were cut and also placed in bijous.The RTV silicone could not be spin coated due to its high viscosity. Each of the cast samples were much less than 0.5 mm thick, but it was difficult to measure their exact thickness due to the compliance of the material. A set of PDMS and RTV samples without decorin inclusion were also taken as control samples.

This completed the sample harvesting process and concluded with three samples with a spun decorin-PDMS film, three samples of cast decorin-RTV film, three samples of spun PDMS film without decorin and three samples of cast RTV without decorin.

Each of these samples were submerged in 400 μl of phosphate buffered saline (PBS) which was just enough to cover the samples at the bottom of the bijou test tubes. The PBS was made up by dissolving five off the shelf PBS tablets (Sigma-Aldrich) in 500 ml of RO water and stirring with a magnetic stirrer until the tablets were all dissolved. This would produce a solution containing 343 mmol NaCl, 6.8 mmol KCl and 50 mmol PBS which would give a 7.4 pH at 25 degrees Celsius. PBS is an isotonic salt solution containing disodium hydrogen phosphate and sodium chloride that is commonly used in biology to ensure the pH of a solution is maintained as chemical reactions occur, so that small pH changes do not affect the reaction.

After one hour of submergence the solution in each sample was harvested using a clean pipette tip for each sample. The liquid from each was transferred to an eppendorf tube, labeled and sealed for future testing. Another 400 μl of PBS was added and after another hour the harvesting was repeated. The process was repeated once again after 24 hours with another 400 μl of PBS added. Longer term release trails were not possible due to time constraints.

This process resulted in a set of liquid samples, half of which should have contained small traces of decorin if the leaching process was successful and half of which should contain only PBS as control samples.

7.5 Decorin Measurements

In order to test how much decorin had been released into the liquid samples an Enzyme Linked Immunosorbent Assay (ELISA) was preformed on a subset of the samples. This is a biochemical technique that uses enzymes to detect small amounts of specific chemicals, in this case decorin. The ELISA testing process is outlined below, and concludes with an enzyme reacting with the decorin which produces a coloured compound. The colour can then be quantised by measuring the optical density (at 450 nm wavelength) of the well plate. This can be compared against a standard concentration curve so that the amount of decorin released into the PBS can be measured.

7.5.1 ELISA Process

The ELISA process was carried out using a Human Decorin DuoSet ELISA from R&D Systems along with their recommended components.

First a 96 well plate (DY990, R&D Systems) was used in which the biochemical reactions were carried out. Each of the wells in the plate come with a polymer at its

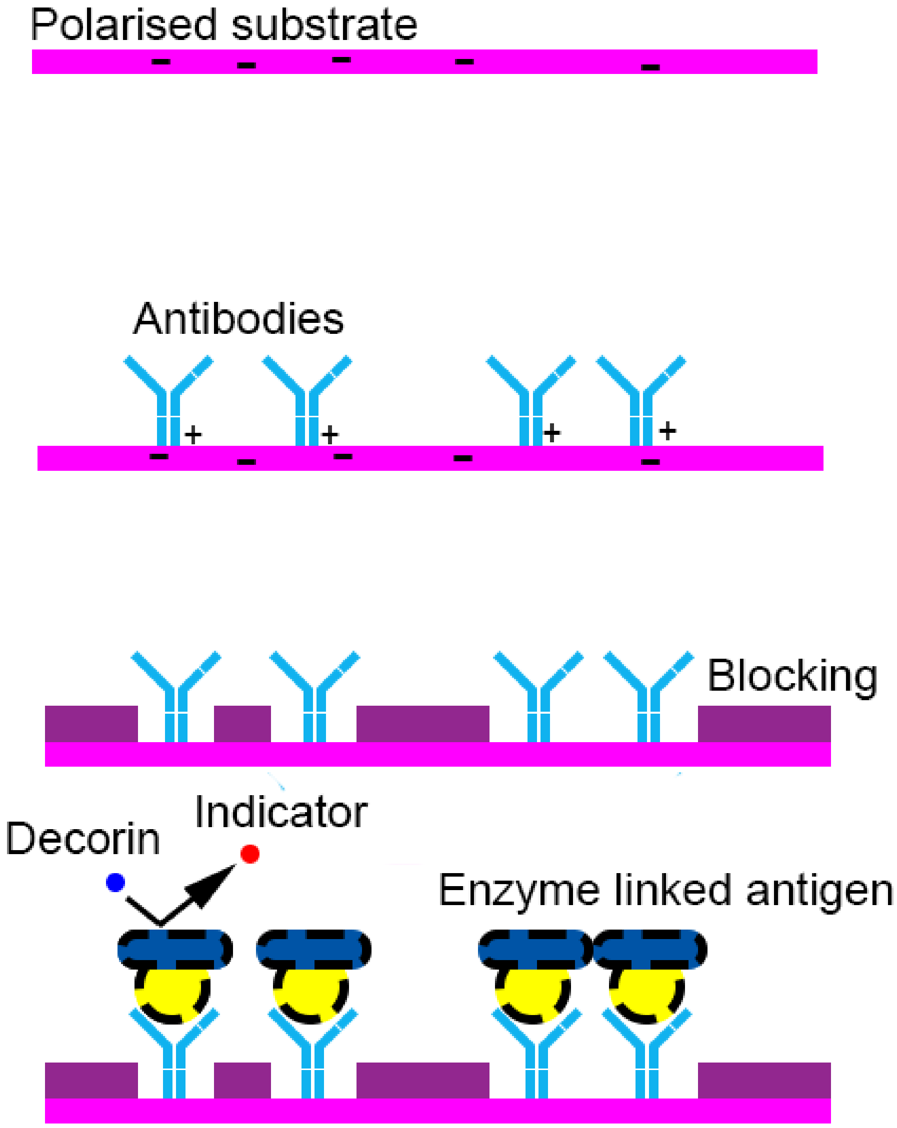

Figure 7.2: The ELISA process, antibodies adhere to a polarised surface, which is then pacified to prevent further involvement in the reaction. An antigen to the antibody that is connected to an enzyme is then linked to the capture antibody. The enzyme will then metabolise a specific molecule, such as decorin, into a indicator molecule that changes the colour of the solution so that the concentration of the decorin will be a function of the optical density of the liquid.

base which is treated so that it retains an electronegative charge. This is an important property for many biochemical reactions as the relative negativity of the well plate base encourages the adhesion of more positive molecules.

The Mouse Anti-Human Decorin Capture Antibody was reconstituted with 1 ml of PBS (which was prepared in the same manor to the PBS used in the previous section). This was then diluted to the working concentration as indicated on the certificate of analysis.

The base of each of the well plates is treated with 100 μl of capture antibody solution. This antibody has an electropositive tail which adheres to the base of the well plate and an antigen specific head that will only bind with one antigen. The well plate was then sealed with para-film and incubated over night at room temperature.

Each well was then aspirated and washed three times with 400 μl 0.05% Tween in PBS Wash Buffer (WA126, R&D Systems), using an autowasher. After the last wash the well plate was inverted and blotted against a clean paper towel to ensure all Wash Buffer was removed.

Each well was then treated with a 300 μl of Reagent Diluent (DY995, R&D Systems), the purpose of which was to deactivate the remaining negative charge on the base, so that it does not play a part in any subsequent reaction. This was incubated at room temperature for a further hour. The well plates were then washed again.

The decorin samples can now be added, either in the form of the release samples taken from the silicones, or the decorin standards that are required to build the calibration curve. The release samples underwent a two-fold serial dilution to produce 1:10 to 1:1280 solutions. This was done because the samples range of decorin concentration was unknown and the serial dilution would bring any high concentrations down into the range of the ELISA. The decorin standards were reconstituted in 0.5 ml Reagent Diluent and a two fold serial dilution adding an extra 0.5 ml to start with was conducted to get concentrations between 2000 pg/ml and 15.6 pg/ml.

100 μl of each sample was then applied to the relevant, preallocated wells (as seen

in table 7.1) and any decorin would have been captured by the antibody. This was left to incubate at room temperature for 2 hours the well plate was then washed again. The antigen is special due to its dual binding sites, allowing for two different antibodies to bind to it. This is helpful for the next step as another antibody that is chemically linked to an enzyme was added. The antibody binds with the antigen and takes the linked enzyme with it.

The Biotinylated Mouse Anti-Human Decorin Detection Antibody was reconstituted with 1 ml of Reagent Diluent and diluted in Reagent Diluent to the working concentration as stated on the certificate of analysis. 100 μl of the Detection Antibody was then added to each well, covered with para-film and left to incubate for 2 hours at room temperature. The well plate was when washed again. Streptavidin-HRP, was diluted in Reagent Diluent to the working concentration as indicated in the certificate of analysis. 100 μl of this was then added to each well and incubated for 20 minutes at room temperature away from any light source. The detection antibody binds with another binding site on the decorin and is attached to an enzyme that can enable the reaction of a certain chromogenic substrate into a coloured product. The well plate was then washed again.

The Substrate Solution was prepared by producing a 1:1 mixture of Color Reagent A (hydrogen peroxide) and Reagent B (tetramethylbenzidine) (DY999, R&D Systems). 100 μl of the mixture was then added to each well and incubated for a further 20 minutes, avoiding direct light exposure. The chromogenic substrate undergoes a reaction, enabled by the enzyme, which produces a coloured compound, the amount of this compound produced is directly proportional to the amount of decorin in the sample, as this dictates how much of the enzyme can be linked to the bottom of the well plate. 50 μl of Stop Solution (Sulphuric Acid, DY994, R&D Systems) was added to each well and the plate gently tapped to ensure good mixing. The Sulphuric Acid would denature the enzymes at this point, stopping the chromic reaction progressing any further and a colour change is observed from blue to yellow.

The optical density of each well was taken, a colour absorption vs concentration cali-

Table 7.1: Showing the contents of each of the wells in the plate at the time of testing. The first two columns are taken up with standard solutions, which are tested along with thin film decorin PDMS and cast decorin RTV after 1h, 2h and 24h immersion time. All of which undergo serial dilutions down the well plate in an attempt to bring the concentrations down into the range of the ELISA.

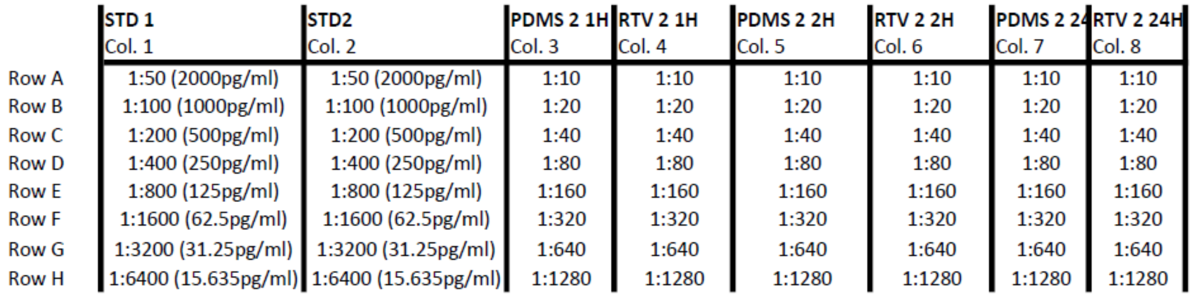

	STD 1 Col. 1	STD2 Col. 2	PDMS 2 1H Col. 3	RTV 2 1H Col. 4	PDMS 2 2H Col. 5	RTV 2 2H Col. 6	PDMS 2 24 Col. 7	RTV 2 24H Col. 8
Row A	1:50 (2000pg/ml)	1:50 (2000pg/ml)	1:10	1:10	1:10	1:10	1:10	1:10
Row B	1:100 (1000pg/ml)	1:100 (1000pg/ml)	1:20	1:20	1:20	1:20	1:20	1:20
Row C	1:200 (500pg/ml)	1:200 (500pg/ml)	1:40	1:40	1:40	1:40	1:40	1:40
Row D	1:400 (250pg/ml)	1:400 (250pg/ml)	1:80	1:80	1:80	1:80	1:80	1:80
Row E	1:800 (125pg/ml)	1:800 (125pg/ml)	1:160	1:160	1:160	1:160	1:160	1:160
Row F	1:1600 (62.5pg/ml)	1:1600 (62.5pg/ml)	1:320	1:320	1:320	1:320	1:320	1:320
Row G	1:3200 (31.25pg/ml)	1:3200 (31.25pg/ml)	1:640	1:640	1:640	1:640	1:640	1:640
Row H	1:6400 (15.635pg/ml)	1:6400 (15.635pg/ml)	1:1280	1:1280	1:1280	1:1280	1:1280	1:1280

bration curve could be generated, as seen in the next section. The optical densities of the unknown samples could then be compared against this graph and the concentrations of each well could be extracted.

7.5.2 ELISA Results Analysis

Following the ELISA protocol the optical densities at a wavelength of 450 nm were taken from each well in the plate. There were 28 empty wells in the well plate, the optical density of these were also measured, due to inefficiencies in the measurement system (mainly due to losses through the well plate) the empty wells still provided small readings. These readings were averaged to get a mean “zero” reading of 0.028. The measurements of the empty wells can be seen in figure 7.3. The mean value was calculated and this was subtracted from all other readings in order to normalise the gathered results.

Two sets of standard solutions were included in the test wells which were made up by taking known quantities of decorin and dissolving it so that the concentration of the solution was accurately known. These standards underwent a serial dilution so that a concentration vs optical density calibration curve could be generated, figure 7.4.

Microsoft Office’s Excel was then used to fit a linear line of best fit to this data, the line was then normalised to intercept the y-axis at the origin, in order to remove the

Figure 7.3: The absorbency readings of the 28 empty well plates.

offset. This gave equation 7.1.

$$C = 625A \tag{7.1}$$

Where C is the concentration of decorin in the well and A is the absorbency of the well after the ELISA.

From this the absorbency readings of the wells can be converted into concentrations, these can be seen in figure 7.5 for the PDMS samples and in figure 7.6 for the RTV samples.

Figures 7.5 and 7.6 show three limits to the measurement ability of the experiment. The Detection Limit is the limit below which there could be systematic noise present (approximately 2 pg/ml), where the measured results may be artifacts arising from absorption of light by a part of the measurement system. The Measurement Limit is the concentration below which an accurate estimation of the decorin present cannot be made,

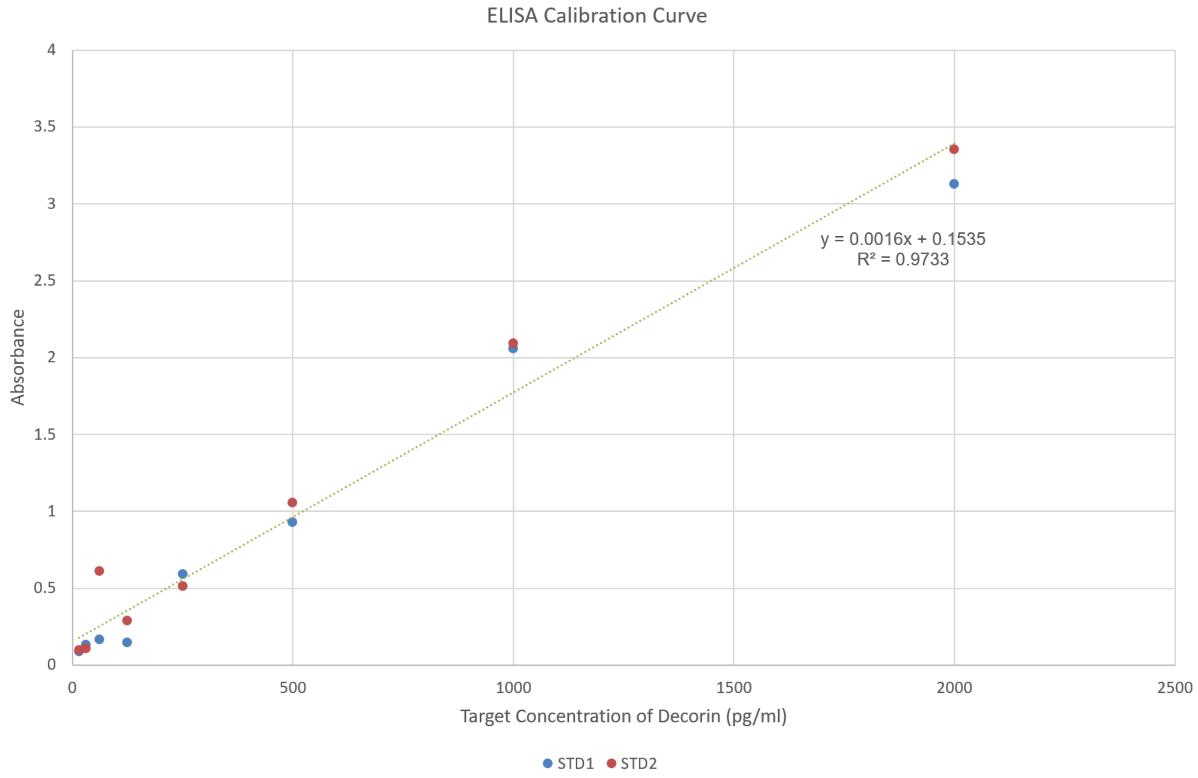

Figure 7.4: Calibration curve generated by the standard solutions absorption results. The equation generated can then be used to calculate the decorin concentrations for the remaining wells.

Figure 7.5: Concentration of decorin leached out of the PDMS sample over the three time points in pg/ml.

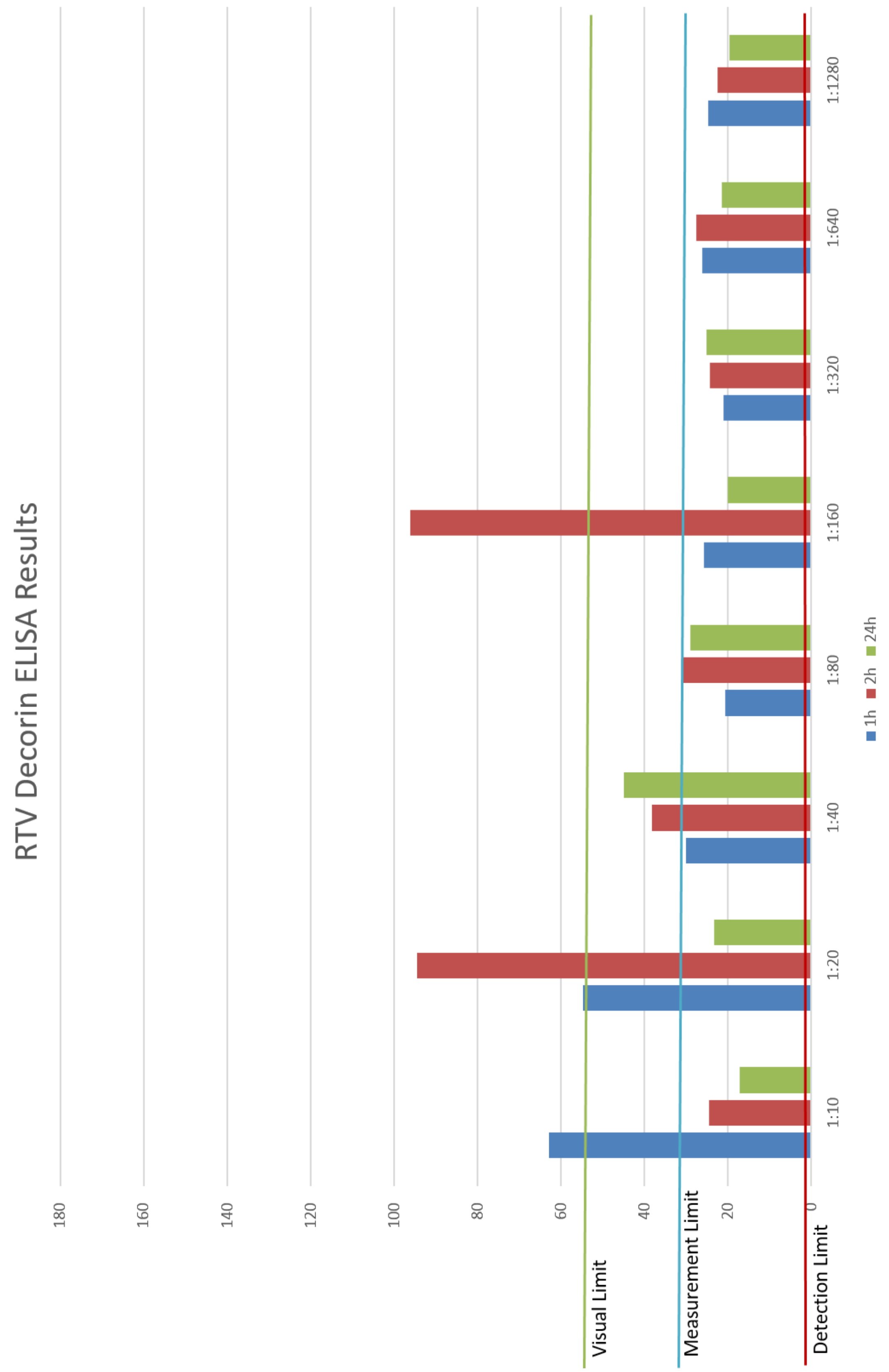

Figure 7.6: Concentration of decorin leached out of the RTV sample over the three time points in pg/ml.

this is a result of the chemical process and is 36 pg/ml. The Visual Limit is the limit above which clear colour changes could be observed with the naked eye which is approximately 55 pg/ml.

Some of the wells demonstrated clear positive results but as can be seen in figure 7.7, the accuracy of the results dramatically reduce with lower concentrations. Due to this the values shown here are insufficient to draw quantitative conclusions, however as an "acid test" the results clearly show that some decorin was released from the silicone. In five of the measurements the reaction was enough to produce results visible with the human eye, providing evidence that the silicone is acting as a medium through which decorin can be applied.

It would be expected that over time the rate of decorin release would reduce, the concentration gradient reduces as more decorin is released. We may expect this because in the first time period, the decorin would release from the surface of the silicone, however, in the second period, the decorin would have to first move from further within the silicone, to its surface and would then release. If the results presented gave a better measurement of the decorin released from the samples, they could be summed to produce a cumulative drug release profile.

The magnitude of the concentrations shown by the ELISA analysis are mostly below the quoted concentration Measurement Limit of the ELISA protocol (31.2 pg/ml). This means that the quantitative analysis of this experiment is inconclusive. However, qualitatively enzymes react only with their specific antigen, and there were small amounts of obvious colour change in the samples. This means that a small amount of decorin must have been released from these samples, but that the concentration of that released was small. Researchers from the Institute of Inflammation and Ageing at the University of Birmingham, advised that even with the small quantities released there may be therapeutic benefits, especially as the aim is to have the decorin release over a long period of time, and that the test time for this experiment was only 24 hours. No controls were tested during this round of experiments due to limited reagent availability.

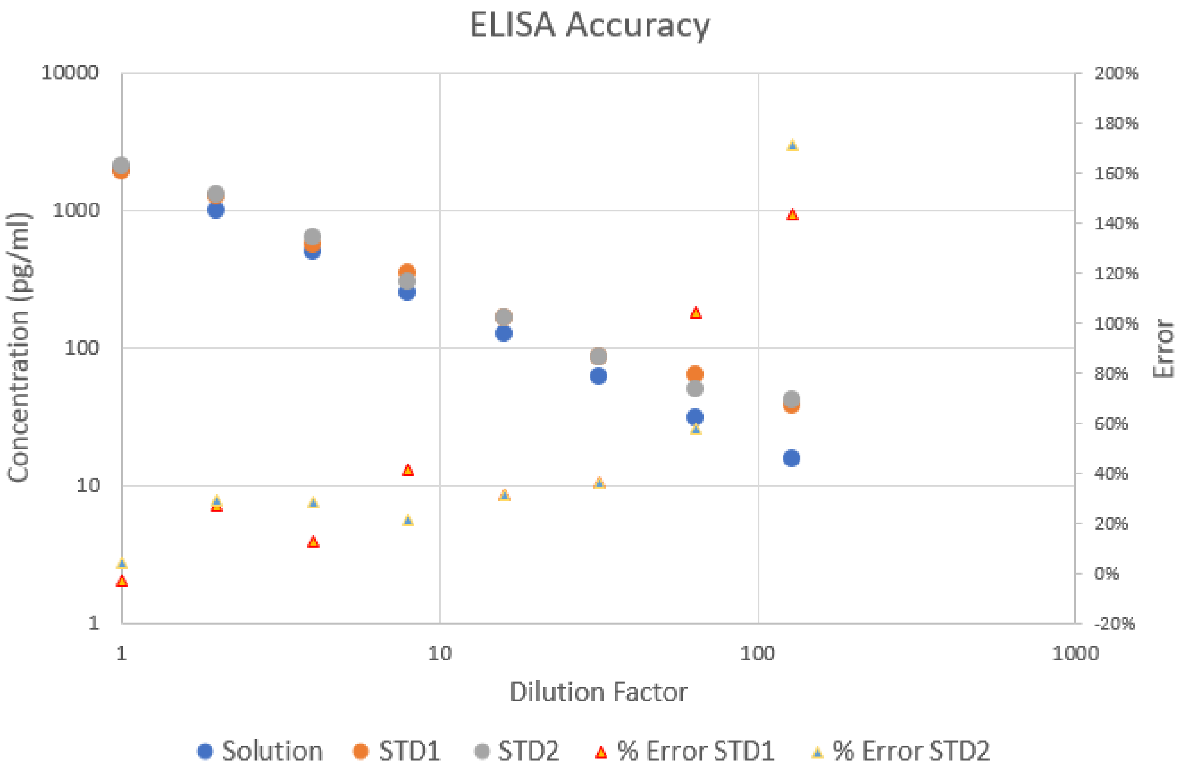

Figure 7.7: Measured (STD1 and STD2) and expected (solution) values from the serial dilution of the standard decorin concentrations shows how the percentage error dramatically increases as decorin concentration decreases.

Contamination of the samples is a possible source of the positive results, however this is extremely unlikely, as the original decorin samples were taken in a completely different lab and new materials were used for each well plate when conducting the ELISA. There is also no evidence of systematic contamination from the standards, which would be evident in the measurements. These results are therefore a fair representation of the decorin that is present in the samples. There were clear visible results that decorin can be released from a silicone based substrate, in both cast and spun silicone films.

7.6 Drug Delivery Potential

Concurrent with the research presented here into the drug delivery potential of decorin infused silicone, a similar study was presented by Fitzgerald (2016). This demonstrated how an anti-inflammatory steroid, dexamethasone, can be incorporated into silicone layers using the same techniques used in the decorin study [96]. In the study, sheets of steroid-loaded silicone were encased in a silicone structure that can be seen in figure 7.8.

Models of the drug elution over time showed that therapeutic doses of the drug were released over a long period of time, as can be seen in figure 7.9.

The infused silicone would leach into the untreated silicone and then on into the 150 μm channels through the concentration gradient. This gives the promise of programmable dose rates if fine tuning the structure to optimize diffusion paths.

The models were then corroborated by an *in vivo* study that showed dramatically reduced scar tissue at three, six and nine months implantation in steroid loaded devices when compared to non-loaded devices.

This study adds significant support to the idea that decorin could be used in the SPNI and that it could be expected to leach into the channels at a clinically relevant rate.

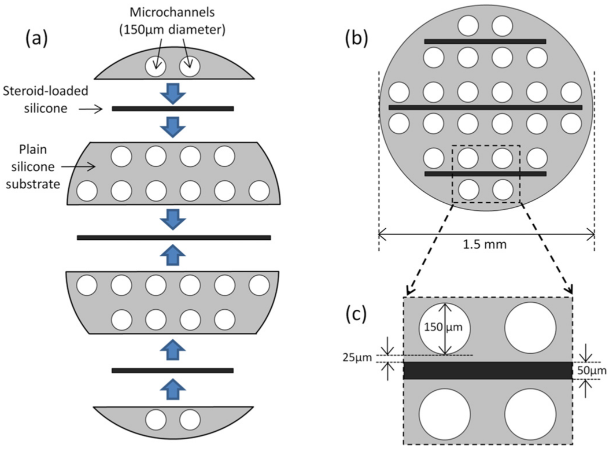

Figure 7.8: Taken from [96], shows the assembly used in the implantation trial, with layers of drugged silicone in between sheets of silicone with channels cast into them. The dexemethosone then leaks from the doped silicone into the channeled silicone, providing a programmable delay before drug administration.

7.7 Conclusions of Drug Delivery in Silicone Augmented Neural Interfaces

The trial successfully incorporated and released decorin into silicone sheets as shown from the antigen specific reaction gained from the ELISA protocol. The accuracy of the results were below the threshold supported by the assay, but gave clear results that decorin had been successfully integrated into the silicone sheet. It is unclear if the small amount measured would have been enough to be therapeutic due to the small sample time for the experiment. However [96] produced similar models along with results demonstrating the viability of the idea. Enough evidence has been generated to suggest that investigation into the effectiveness of decorin as a silicone loaded agent is worth further research in the continuing attempts to improve the chronic viability of peripheral neural interfaces.

This chapter has shown how anti-scarring agents can be released from the PDMS layer, the following chapter will combine all of the findings in this thesis and put them in the wider context of neural interface research.

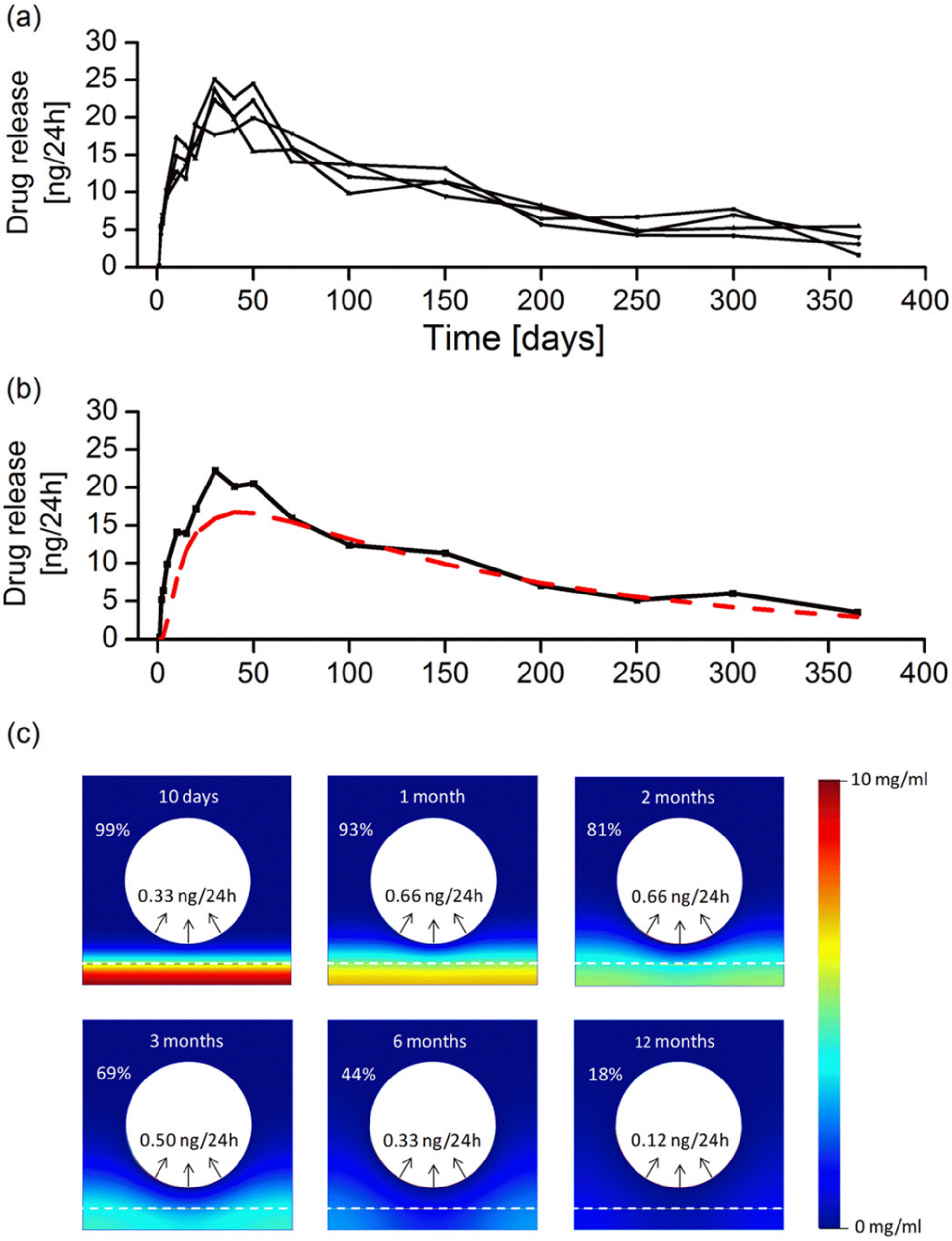

Figure 7.9: Taken from [96] showing how the rate of drug release changes over time.

CHAPTER 8

CONCLUSIONS AND FUTURE RECOMMENDATIONS

This section summaries and concludes the thesis, going on to describe the context of the research outputs herein presented in the wider field. This is followed by a brief discussion on the future directions of neural interface technologies, and then by recommendations for future research with regards to the SPNI.

8.1 Summary of the Thesis and Conclusions

8.1.1 Motivation of Thesis

State-of-the-art prosthetics are sophisticated and capable of complex movements that are comparable to the functionality of biological counterparts. The limiting factor to the acceptance and dissemination of this technology has moved to the human-machine interface used to translate user intent into the bionic limb action. Commonly used myoelectric electrodes do not offer the resolution required for fine control of the prosthetics and have to be reapplied daily to prevent adverse skin reactions. As such the vast majority of powered prostheses issued to patients remain unused.

In order to circumvent these issues neural interface technologies have been subject to intensive research for nearly 40 years and many different styles of interface have been developed. Central neural system penetrating electrodes have been accepted for limited clinical use but have been shown to damage surrounding brain tissue over time, due to their mechanical non-compliance. A potential solution to the brain computer interface for the driving of prosthetics is to recruit PNS nerves that originally serviced the damaged or missing limb.

Peripheral neural interfaces suffer from a selectivity verses invasiveness dichotomy, where more detailed information about user intent can only be acquired by increasing levels of damage to remaining nerves. For the case of amputees, this is less of a concern as damage has already been sustained, and more invasive treatments can yield significantly better functionality.

In order to get the required resolution it is ideal if individual axons are recruited, the most viable high density arrays are regenerative neural interfaces, which take advantage of severed nerves reinnervating their distal stumps. The SPNI is an example of a regenerative neural interface that encloses regenerated axons in insulating channels so as to take advantage of improved SNR facilitated by the increased extracellular resistance.

The SPNI had been tested previous to this work but has demonstrated several performance problems which require solution before the technology can be advanced. These were current leakage within the device causing lower SNR than expected along with ambiguous stimulation of captured neurons. Biocompatiblity was also an issue limiting the channel density of the device, along with reducing the chronic viability of the electrode array [43].

8.1.2 The Fragility of Thin Films

One of the concerns when developing a neural interface is the relative fragility of thin film gold which is used as the electrode material. It is common practice to include the gold in the stress neutral plane of the device to avoid this issue.

This thesis has shown, by way of a bending experiment, that the inclusion of the gold in the stress neutral plane is not a requirement for maintaining the continuity of metallic conductors given that they are laminated by a material of considerably lower Young's Modulus. The lamination effect prevents stress concentration from impurities causing the metal film to fracture, and thus increasing its functional ultimate tensile stress. Due to this phenomenon it was proven that the SPNI could be rolled either way, and that a modification of the structure to include a sealing layer would not result in electrode feed breakages.

8.1.3 Channel Leakage Currents and Biocompatibility

The non-perfect sealing between channels of the SPNI was shown to be responsible for the lower SNR and ambiguous stimulation results. To solve this problem a thin film of PDMS was incorporated into the SPNI to seal the tops of each channel so that current could not leak out of active channels into those adjacent.

Biocompatibility of neural interfaces is an ongoing problem in neural interface research, there are two promising solutions: reduce the difference in Young's modulus between implant and biological materials, and include active drugs into the devices to prevent the foreign body response from affecting interface prognosis. It was shown in this thesis that decorin was successfully included into thin sheets of PDMS, but further research is required to determine the viability of this technique at improving neural implant chronic viability.

8.1.4 Research Outputs

The research outputs of this thesis have shown that:

a) During the design of neural interfaces it is not necessary to place the metallic conductor in the stress neutral region of the device, as the laminated gold can withstand strains that would break a free standing film.

b) Current leakage in channels can be significantly reduced with the use of silicone membranes which will improve the signal to noise ratio of captured neural signals.

c) Anti-scarring drugs can be included in the sealing membrane with a view to reducing the foreign body response and will hopefully improve the chronic viability of neural interfaces in the future.

8.2 The SPNI 2.0

This thesis proposes a new generation of SPNI, one where signal leakage will no longer affect the functional viability of the device, not only this, but it also proposes a method by which the foreign body response can be reduced.

By introducing a new material layer the above have been achieved, figure 8.1. The new SPNI is fabricated using the same methods as previously described in the literature, with the addition of a PDMS layer on top of the channels. This PDMS could be doped with various drugs to help the proliferation of nerve growth along with increasing the chronic performance of the device. In this condition the SPNI is ready for further testing *in vivo* to validate both the performance of the new electrode array along with the effectiveness of various drugs on the SPNI performance.

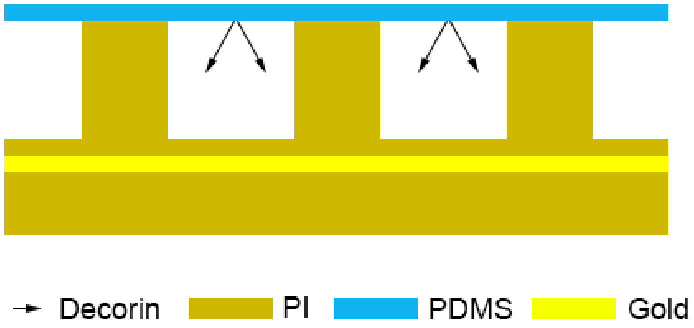

Figure 8.1: The updated SPNI design with a PDMS insulation layer sealing channels to prevent interchannel current leakage and to provide a medium by which bioactive molecules can be presented to neurons.

8.3 The Greater Picture

Regenerative neural interfaces are the most effective method of interfacing to a large number of axons with minimum potential of biological rejection. The competing technologies do not have the required selectivity when considering cuff electrodes, or trigger catastrophic bio-rejection when using multiple penetrating electrodes to gain higher resolutions [98]. The PNS is a more viable target than the CNS due it's inability to regenerate upon implant insertion due to the complex cellular clutter that is prevalent in the CNS. All attempts at CNS implants have yielded results that degrade over time and/or damage surrounding tissues due to the insertion trauma, chronic inflammation and mechanical mismatches causing further injury over time [99].

The major challenge with regenerative peripheral neural interfaces is still long term instability. Chronic functionality of PNS interfaces is limited by factors such as chronic inflammation around the implant site, Wallerian degeneration, neuroma formation and encapsulation of the implant by surrounding tissues. There are in general three methods by which instabilities are being designed out of the neural interfaces: by the redesign of device geometries to guide neural outgrowth such as used by the SPNI, the incorporation of coatings and bioactive molecules to increase viability, adhesion, growth, signal strength, etc., and the introduction of biological hybrids, either utilizing supportive cells within devices to encourage favorable properties or by making arrays of trapped muscle which can then be vascularised and targeted by neurons to act as biological amplifiers [98].

The SPNI as well as providing a possible platform for several of these technologies has paved the way for a new generation of microchannel-based regenerative electrode array [98, 100, 101]. Utilising the passive amplification that increased extracellular resistance provides.

Srinivasan et al (2015), has used the SPNI design with a PDMS/SU8 scaffold which reduces biocompatibility issues to negligible levels, has been shown to produce no neuroma formation and has been shown to provide readings in mobile rodents for over five months [100]. The success of this design is thought to be down to the low Young's modulus of the PDMS. This design also inherently incorporated sealing, and as such further validates the results obtained in this thesis, i.e. that a spiral structure of the same dimensions can be used to record action potentials with integrated electrodes if the leakage currents are mitigated. The device which can be seen in figure 8.2 uses PDMS as a substrate, and as such may benefit from the drug inclusion into silicone as shown in this thesis. If the drug inclusion affect can be recreated with other drugs, this may produce a powerful combination.

Other channelled arrays have also been used to separate out motor and sensory neurons by placing different growth promoters at different places in the device. Splitting motor and sensor neurons is incredibly useful as stimulation and measurement electrodes could be independently designed and finer resolution achieved [102, 103].

The SPNI is a precursor to many key neural interface technologies that will be presented in the future. The work in this thesis has improved the SPNI as a functioning neural interface and has also shown promise to including active molecules into the neural interface structure by the simple means of mixing agents with silicone, rather than the complex surface chemistry often used to include bioactive molecules in other neural devices [104, 105].

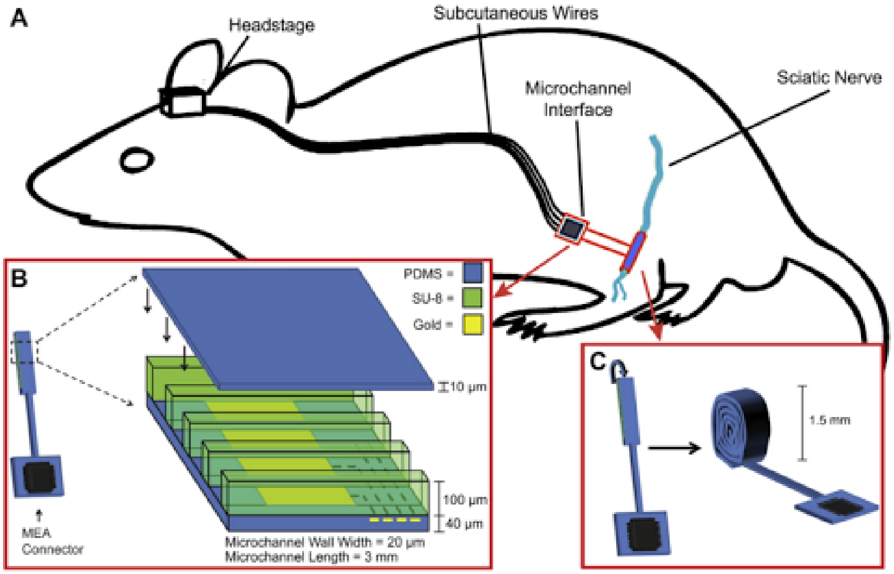

Figure 8.2: Taken from [100], showing a) the experimental procedure where by the sciatic nerve was intersected and a SPNI inspired device implanted, with wires running up to a head stage where data and power was processed, b) shows the fabrication of the device with a PDMS substrate, SU8 channels and a PDMS insulation layer, c) shows how the device was rolled

The SPNI can also act as a scaffold for biohybrid matrices, or drug delivery in the future. Although the work Srinivasan et al (2015) has shown to be more effective when using PDMS/SU8 scaffolds, the SPNI is inherently easier to produce, due to the materials used. However, as Srinivasan et al (2015) has got around the bespoke fabrication limitations previously applied to silicone based device, both this and the SPNI devices are viable candidates for mass fabrication of neural interfaces that will be usable in clinical trials [100].

8.4 The Future of Neural Interface Technology

Brain computer interfaces that use EEG and prosthetic control that utilities TMR and EMG are still areas of intensive ongoing research [106–109]. However, even state-of-the art techniques still require a prohibitively large number of electrodes to gain adequate information to be useful. Commercial BCIs are beginning to emerge [110], however, their functionality is extremely limited due to their small number of electrodes (which is for consumer convenience). Large successes are being found in these areas, with movement intent being accurately mapped in laboratory situations. With targeted muscle reinnervation, it has been observed that brain plasticity can reroute sensations from their new target muscles in the chest and interpret them as being from the missing limb, hence providing a potential route for haptic feedback using conventional EMG electrodes. However, a large number of electrodes are required and are associated with high computational cost (figure 8.3). Using current and foreseeable technology, it is difficult to see these kinds of interfaces being used as a consumer or medical solution in the near future, except within highly controlled environments [106].

Figure 8.3: a) an electrode array for state of the art EEG measurement taken from [109], b) electrodes being used for TMR recording [111].

Devices designed for the PNS are more likely to develop faster than those applied to the CNS due to inherent difficulties of the brain environment, and it is in the PNS that electrode based neural interfaces will prove most viable. The next stage of neural interface development lies in material modification such as the use of conductive polymers and nanomarterials to improve cell adhesion, cell growth, electrode impedance, biocompatibility etc [85, 112–114]. After this the inclusion of bioactive molecules into devices will provide further gains, either via including extracellular matrices laced with active molecules or by active chemical inclusion of molecules onto the surface of the materials [104, 105].

The next level of complexity would be to include biology directly into the interface. This could either take the form of integrating small sections of the host muscle into the interface and encouraging nerves to trigger much larger motor unit action potentials for every AP, as a biological amplifier [115] or by providing a matrix of supportive host cells into the devices to encourage advantageous reactions [116].

Optogenetics has also been producing results in neural stimulation and recording. Whereby the host's DNA is altered to make their neurons light sensitive and bioluminescent, enabling the use of LEDs and photodetectors in the place of electrodes. Although cumbersome for PNS systems, optogenetics may play a major role in future CNS brain-computer interfaces [117] [118].

Over the next few decades treatments of hand transplant patients will dramatically improve, as will the 3D printing and culture of body parts [119–121]. This may in time take the place of neuroprosthetics for rehabilitation use, but there will still be a human need for a fluid human-machine interface.

8.4.1 Biocompatability

In order to get a functioning neural interface that is to be of use for amputees the problem of biocompatability needs to be fully addressed. The solution to this is likely to come from two directions; making neural implants out of conformal electronics that share physical properties with the body, and thus do not trigger an immune response from movement artifacts or Young's modulus incompatibilities. The limiting factor to this kind of technology at the moment is that fabrication of conformal electronics on a mass scale is proving difficult, however many are making advances in this area [100, 122, 123].

From the other direction will come fine tuning of drug application to prevent the foreign body response and a dedicated effort at integrating these drugs into implanted devices. Decorin has shown promise in the regeneration of neural tissue [92, 124], but other drugs and techniques that support the neurons in the long term and enhance their performance are also on the horizon [104]. With the application of both of these techniques it is possible that neural interfaces will be up and running in limited clinical trials within ten years.

Once the foreign body response to the implants have been solved, final solutions toward the required resolution of neural implants will be possible, as the experiments will not be limited by the inflammation and longterm scaring that plagues current long term studies. With the accompaniment of state-of-the-art cybernetics a minimum viable neural resolution can be acquired for different use cases, and as such neural interfaces can be more accurately designed.

This will then open up the neural interface prototypes to industrial development where engineering a suitable package for the neural interfaces will be the priority. With transdermal power and information exchange along with the advent of body area networks will allow the implants to become invisible and maintenance free. After moving to clinical trials and when the benefits to amputees outweigh the risks of neural implantation an increase in uptake and use of neuroprosthetics can then begin.

8.5 Future Suggestions for the SPNI

The SPNI is a good platform on which future neural interfaces can be built. There are several viable research routes that can still be taken using the SPNI, these include confirmation of drug elution potential, a redesign for clinical applications and a long term *in vivo* study.

8.5.1 Confirming Drug Elution Effects on Compatibility

The next stages of SPNI development would be to continue work on the biocompatibility benefits of Decorin inclusion. This would include a more comprehensive study of elution rates of Decorin over time leading to a long term study in mobile rodent models. If including Decorin were to show good therapeutic effects it may also be worth conducting a study demonstrating the ability to elude other drugs such as dexamethosone or neural growth factor. This would provide evidence to whether the silicone film is a robust carrier that can administer different bioactive molecules. Alongside this research, the PDMS process should be refined so that its addition does not require manual manipulation, and can be applied using standard microfabrication techniques.

8.5.2 Design for Mass Production

There is an inherent variability in the way the SPNIs are fabricated due to slight differences in etch and/or deposition rates across the wafer surface during the lab based processes. Along with this, the total yield of the SPNIs is low. Many of the devices fail either before or during the channel baking stage and some of the devices that survive the channels, break upon rolling. Research should go into the development of the technology to increase the overall yield of the SPNI and to remove the inherent variability within the process. This would speed up the progress of subsequent research and give more credence to the SPNI as a mass producible device.

8.5.3 Design for Clinical Use

Once the benefits of the SPNI design have been demonstrated, before its use in awake and mobile models, the SPNI will need to be incorporated into a neural interface platform which can reliably and robustly act as a biological transducer. In order to do this, footprint and form factor are major concerns. Standard electronic measurement on biological systems requires a preamp, in previous experimental paradigms this has been applied outside of the animal model during surgical recording of an unconscious animal. However, in a live model this would not be the case as live recorded data would need to be transmitted from a freely moving animal. Thus, the preamp needs to be included into the neural interface platform. A good candidate for this is the RHA2216 by Intan Technologies [31].

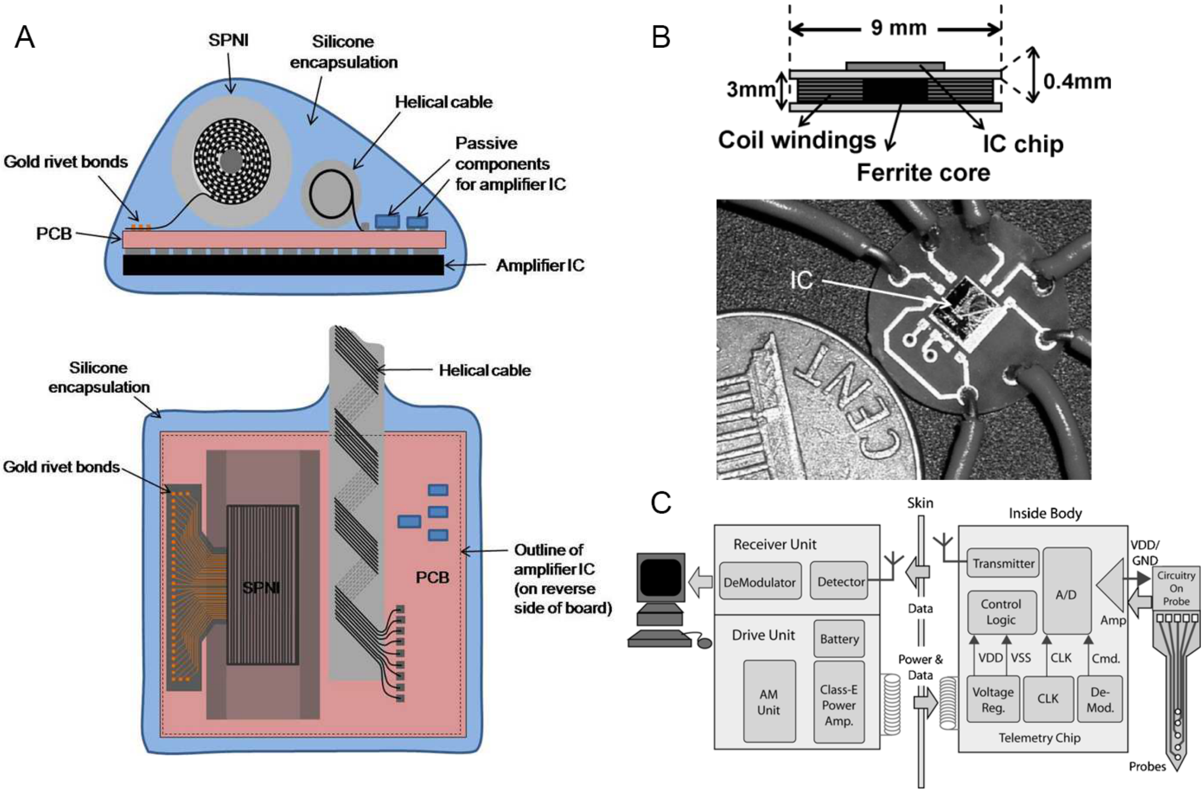

Figure 8.4: The system design of the SPNI platfrom will have to include: a) fully integrated packaging of the SPNI and support electronics, coated in a biocompatible housing [31], b) will have to include wireless power transmission such as that proposed by [125], c) along with wireless communication systems similar to that seen in [126]

This chip would be the limiting factor for the size of the neural interface platform. It would be possible to redesign the connector of the SPNI to occupy less space as seen in figure 8.4. This would have to be utilised in conjunction with wireless communication and power technologies.

This kind of platform could be used to record neural activity in a mobile host over a long period of time.

8.5.4 Long Term *in vivo* Study

Once biocompatability and integration of the SPNI are established another implantation study should be preformed which would take live data from rodent models over a long period such as 12 months. Histology and signal data would show if the SPNI were sufficiently developed to support neural growth and record neural signals in the long term.

Along with this studies that capture accurate information about the gait of a rodent and correlate this with signals gained via the SPNI should be pursued. This could be achieved by implanting the SPNI and running trails that involve rodents making known movements such as on a treadmill or ladder, and corresponding kinematic data with neural activity data to confirm that the SPNI is a good interface that has the required resolution to predict intended movements from neural activity.

This would provide good evidence that materials and protocols in the SPNI fabrication process should be qualified for human use and would point to potential clinical trials with the SPNI.

This chapter concludes the thesis, to follow are appendices and reference lists for the interested reader.

Appendices

APPENDIX A

DETAILED MICROFABRICATION METHODS

A.1 Sacrificial Layers

A.1.1 Deposition of a PMMA sacrificial layer:

- Take a fresh 525 μm thick, single side polished silicon wafer with 250 nm silicon oxide layer. However, any wafer with enough mechanical strength will suffice.
- Clean the wafer by spinning at 1000 rpm and spraying with an excess of acetone, then in conjunction with and followed by isopropanol. Continue to spin until most of the solvent is driven from the wafer.
- Flash bake at 120 °C for 5 minutes followed by 5 minutes cooling.
- Load the wafer into a spin coater and pour approximately 5 ml of PMMA onto the center of the wafer.
- Spin at 400 rpm for 2 seconds, 1100 rpm for 2 seconds and 850 rpm for 12 seconds.
- Place on a preheated 85 °C hotplate for 2 minutes, rising to 130 °C for 10 minutes and finally 180 °C for a further 10 minutes.
- Allow to cool to room temperature.

A.1.2 To release the PMMA layer:

- Fully submerge the wafer in MIBK, allowing for evaporation.
- Leave for between 19 and 24 hours.
- Gently agitate and harvest released samples.

A.1.3 Deposition of aluminum sacrificial layer:

- Load a fresh wafer into a vacuum evaporation chamber with aluminum pellets loaded in an evaporation crucible.
- Increase the current through the crucible until the aluminum can be seen to melt, the exact voltage and current at which this happens will vary depending on the number of times the crucible is used.
- Open shutters and expose the wafer for 30 seconds.
- Ramp down current at a rate of 0.5 V per minute to avoid crucible fracture.
- Remove coated sample from vacuum chamber

Warning: Aluminum will form thick layers on the inside of the vacuum chamber very rapidly.

A.1.4 To release the aluminum layer:

- Dissolve 117 g of NaCl in 500 ml of distilled water.
- Place gold electrode in solution, so that only gold is submerged.
- Place wafer to be released in solution so that it is electrically isolated from the gold electrode.

- Electrically attach the aluminum layer to the gold layer via a clamped wire (ensure wire does not get in solution).
- Wait overnight for samples to release.
- Soak released samples in 50 ° distilled water for 30 minutes to remove any excess salt.

A.2 Spinning of Polyimide Layer

- Load a wafer pre-treated with a suitable release layer in a spin coater (WS-650MZ-23NPP, Laurell).
- Pour approximately 5 ml of either Durimide 7020 (FujiFilm) (for 18 μm thickness) or Durimide 7505 (FujiFilm) for (5 μm thickness) on to the center of the wafer.
- For an 18 μm layer spin at 500 rpm for 10 seconds, 3000 rpm for 20 seconds and then 700 rpm for 10 seconds. For a 5 μm layer spin at 500 rpm for 5 seconds, 3800 rpm for 30 seconds and then 300 rpm for 1 second.
- Remove from spin coater and place on a hotplate (1000-1, Electronic Micro Systems), preset at 20 degrees Celsius.
- Preform soft bake by increasing hot plate temperature to 90 degrees Celsius at a rate of 3 degrees per minute. Keep at 90 degrees Celsius for 8 mins.
- Allow the wafer to cool while covered on the bench top for 20 mins. (Keep hotplate on)
- Load the wafer into an i-line mask aligner (Parallel Light Mask Aligner, PLA-501F, Canon).
- Insert and align mask as appropriate

- Expose for a light integral of 16 seconds for 18 μm or 8 seconds for 5 μm
- Place back on hotplate at 90 degrees Celsius and flash bake for 3 mins allowing 10 mins to cool
- Prepare a petri dish with HTRD2 (FujiFilm), a petri dish with a HTRD2/RER600 mixture (1:1) and a petri disk of RER600 (FujiFilm).
- Prepare two wash bottles, one with HTRD2 and one with RER600
- Dip and agitate in HTRD2, followed by a shorter dip in the mixture, followed by dipping and agitating in RER600.
- Reverse this process and do a complete cycle three times.
- Periodically rinse with the appropriate wash bottle.
- Check samples under a microscope to check they have developed correctly.
- If not then undergo another cycle, if so dry with nitrogen gas.

A.3 The Gold Layer

A.3.1 Metalization

- Outside of a cleanroom, place the wafer to be coated in the vacuum chamber of a thin film deposition chamber (308R Coating System, Cresington). Load enough gold for the evaporation into the crucible.
- Pump down until pressure is less than 2×10^{-6} bar.
- Outgas the crucible by applying voltage in a 1 V per min ramp. Once the current is enough to melt the gold, reduce the applied voltage by 1 V per min. Ensure shutters are in place for this step, so that no deposition onto the sample occurs.

- Apply a weak oxygen plasma to the sample for 30 seconds drawing 40mV (308R Sputter Supply, Cressington).

- Apply a 15 nm chrome layer using a sputter source and head (308R Sputter Supply, Cressington), by applying 80mV for 30 seconds. Allow 30 seconds before removing shutters also, so allow chrome oxide to burn off. Thickness can be monitored with a mtm10 Thickness Monitor from Cressington.

- Apply a 100nm thick gold layer by increasing the voltage applied to the gold crucible (using a 308R Evaporation Supply LT1500, Cressington) by 1 V per min until the gold melts. The remove shutters and measure evaporation thickness with a monitor. If correct current applied and sufficient gold in the boat, this should take around 3 minutes.

A.3.2 Resist

- Load the gold covered wafer with into a spin coater.

- Pour approximately 10 ml of SPR-220-7 (MicroChem) into the center of the wafer.

- Spin at 750 rpm for 10 seconds, 2800 rpm for 18 seconds, then 500 rpm for 1 second.

- Place on a hotplate, preheated to 90 degrees Celsius for 2 minutes and then bake at 160 degrees for a further 6 mins.

- Remove the wafer and cool for 20 mins.

- Load the wafer into an i-line mask aligner.

- Align mask as necessary.

- Expose for 35 seconds, wait for 25 seconds, expose and wait for a further three cycles.

- Remove the wafer from the mask aligner and wait for 5 mins.

- Prepare two petri dishes with MF-26A (Shipley), one large one small. Beware, this chemical is particularly dangerous.
- Submerge and agitate wafer in the larger dish for 2 mins.
- Rinse with MF-26A wash bottle and repeat submersion.
- When the sample is developed rinse throughly with wash bottle, back and front of wafer.
- Place wafer in second petri dish and time for 1 min.
- If MF-26A turns at all pink, development is not complete and process is to be repeated.
- Rinse gently with water and remove water with nitrogen.

A.3.3 Wet Etching

- Prepare four petri dishes, one with Gold Etchant (Chestech), one with Chrome Etchant (Aldrich) and two with RO water.
- Submerge wafer in gold etchant for 40 seconds.
- Put in RO water to clean off any etchant residue. Rinse with RO wash bottle and dry with nitrogen.
- Submerge wafer in chrome etchant for a maximum of 40 seconds.
- Wash and dry in separate RO petri dish.
- Rinse with acetone (away from the etchants) and then IPA to remove resist.
- Dry with nitrogen.
- Check sample under the microscope.
- Clean in a plasma etch and UVO cleaner as appropriate.

A.4 Channel Layer

- Load wafer into spin coater.
- Pour on approximately 10 ml of Durimide 7020.
- Spin at 200 rpm for 60 seconds and then 330 rpm for 60 seconds.
- Place wafer on a hotplate kept at room temperature, increase temperature of hotplate at a rate of 0.5 degrees Celsius per minute up to 90 degrees, where the wafer is to be held for 30 mins.

A.5 Final Steps

- Place final wafer in an oven or furnace and hard bake in a nitrogen atmosphere at 200 degrees Celsius for 30 mins, at a thermal ramp from room temperature of 3.5 degrees per minute.
- Increase temperature to 300 degrees at the same temperature ramp and hold for one hour before cooling at a rate of 1 degree per min.
- Once cooled release devices from wafer as appropriate.
- Undertake quality control on released samples.
- Ball bond successful samples to suitable PCBs.

APPENDIX B

PUBLICATION PLAN

B.1 Publications

- Published: Hadis, M.A., Cooper, P.R., Milward, M.R., Gorecki, P., Tarte, E., Churm, J. and Palin, W.M., 2015, March. The effect of UV-Vis to near-infrared light on the biological response of human dental pulp cells. In SPIE BiOS (pp. 930906-930906). International Society for Optics and Photonics.

- Published: Hadis, M.A., Gorecki, P., Cooper, P.R., Milward, M.R., Tarte, E., Churm, J. and Palin, W.M., 2015, March. Light Penetration Through Dentine For Photobiomodulation of the Dentine-pulp Complex. IADR General Session, Volume: 3319, Boston, Mass., USA

- Published: Hadis, M.A., Cooper, P.R., Milward, M.R., Gorecki, P., Tarte, E., Churm, J. and Palin, W.M., 2017. Development and application of LED arrays for use in phototherapy research. Journal of Biophotonics.

- In Preparation: "Spiral Peripheral Nerve Interface: Improvements in Signal Cross Talk": outlining the change in understanding of the nature of the neutral plane placement along with the inclusion of the PDMS membrane and how this has been shown to decrease signal cross talk.

B.2 Publications Note

Due to the unfortunate state of the decorin release experiments it will not be possible to publish these results without further experimentation.

Three of the publications are in collaboration with the dental school based on engineering work completed external to the scope of this thesis.

LIST OF REFERENCES

[1] M. LeBlanc, “The ln-4 prosthetic hand,” in *”Give Hope - Give a Hand”*, 2008.

[2] K. Ziegler-Graham, E. J. MacKenzie, P. L. Ephraim, T. G. Travison, and R. Brookmeyer, “Estimating the prevalence of limb loss in the united states: 2005 to 2050,” *Archives of Physical Medicine and Rehabilitation*, vol. 89, no. 3, pp. 422 – 429, 2008.

[3] D. S. Childress, “Historical aspects of powered limb prostheses,” *Clinical prosthetics and orthotics*, vol. 9, no. 1, pp. 2–13, 1985.

[4] touchbionics, “http://www.touchbionics.com/.” Online [accessed], 07 2017.

[5] OTTOBOCK, “http://www.ottobock.co.uk/.” Online [accessed], 07 2017.

[6] E. Biddiss and T. T. Chau, “Upper limb prosthesis use and abandonment: a survey of the last 25 years.,” *Prosthetics and orthotics international*, vol. 31, no. 3, pp. 236–257, 2007.

[7] J. L. Collinger, B. Wodlinger, J. E. Downey, W. Wang, E. C. Tyler-Kabara, D. J. Weber, A. J. McMorland, M. Velliste, M. L. Boninger, and A. B. Schwartz, “High-performance neuroprosthetic control by an individual with tetraplegia,” *The Lancet*, vol. 381, no. 9866, pp. 557 – 564, 2013.

[8] J. M. Hahne, M. Markovic, and D. Farina, “User adaptation in myoelectric man-machine interfaces,” *Scientific Reports*, vol. 7, no. 1, p. 4437, 2017.

[9] I. Sando, M. Urbanchek, P. Cederna, and C. Chestek, “Chronic recording of hand prosthesis control signals via a regenerative peripheral nerve interface in a rhesus macaque,” *J. Neural Eng*, vol. 13, no. 046007, p. 046007, 2016.

[10] T. A. Kuiken, L. A. Miller, R. D. Lipschutz, B. A. Lock, K. Stubblefield, P. D. Marasco, P. Zhou, and G. A. Dumanian, “Targeted reinnervation for enhanced

prosthetic arm function in a woman with a proximal amputation: a case study," *The Lancet*, vol. 369, no. 9559, pp. 371–380, 2007.

[11] X. Navarro, T. B. Krueger, N. Lago, S. Micera, T. Stieglitz, and P. Dario, "A critical review of interfaces with the peripheral nervous system for the control of neuroprostheses and hybrid bionic systems," *Journal of the Peripheral Nervous System*, vol. 10, no. 3, pp. 229–258, 2005.

[12] P. F. Pasquina, M. Evangelista, A. J. Carvalho, J. Lockhart, S. Griffin, G. Nanos, P. McKay, M. Hansen, D. Ipsen, J. Vandersea, *et al.*, "First-in-man demonstration of a fully implanted myoelectric sensors system to control an advanced electromechanical prosthetic hand," *Journal of neuroscience methods*, vol. 244, pp. 85–93, 2015.

[13] T. Matsubara, J. Morimoto, M. S. Erden, K. Nazarpour, S. Vijayakumar, S. Stramigioli, H. Rietman, P. Veltink, and S. Misra, "Bilinear modeling of emg signals to extract user-independent features for multiuser myoelectric interface," *IEEE Transactions on Biomedical Engineering*, vol. 60, no. 8, pp. 2205–2213, 2013.

[14] M. Yoshikawa, M. Mikawa, and K. Tanaka, "A myoelectric interface for robotic hand control using support vector machine," in *2007 IEEE/RSJ International Conference on Intelligent Robots and Systems*, pp. 2723–2728, Oct 2007.

[15] D. J. Tyler and D. M. Durand, "Functionally selective peripheral nerve stimulation with a flat interface nerve electrode," *IEEE Transactions on Neural Systems and Rehabilitation Engineering*, vol. 10, no. 4, pp. 294–303, 2002.

[16] C. Veraart, W. M. Grill, and T. Mortimer, "Selective control of muscle activation with a mulitpolar nerve cuff electrode," *IEEE Transactions on Biomedical Engineering*, vol. 40, no. 7, pp. 640–653, 1993.

[17] F. Pothof, S. Anees, J. Leupold, L. Bonini, O. Paul, G. Orban, and P. Ruther, "Fabrication and characterization of a high-resolution neural probe for stereoelectroencephalography and single neuron recording," in *Engineering in Medicine and Biology Society (EMBC), 2014 36th Annual International Conference of the IEEE*, pp. 5244–5247, IEEE, 2014.

[18] D. W. Tan, M. A. Schiefer, M. W. Keith, J. R. Anderson, and D. J. Tyler, "Stability and selectivity of a chronic, multi-contact cuff electrode for sensory stimulation in human amputees," *Journal of neural engineering*, vol. 12, no. 2, p. 026002, 2015.

[19] K. R. Harreby, A. Kundu, K. Yoshida, T. Boretius, T. Stieglitz, and W. Jensen, "Subchronic stimulation performance of transverse intrafascicular multichannel electrodes in the median nerve of the gottingen minipig," *Artificial organs*, vol. 39, no. 2, pp. 36–48, 2015.

[20] C.-W. Chang, Y.-K. Lo, P. Gad, R. Edgerton, and W. Liu, "Design and fabrication of a multi-electrode array for spinal cord epidural stimulation," in *Engineering in Medicine and Biology Society (EMBC), 2014 36th Annual International Conference of the IEEE*, pp. 6834–6837, IEEE, 2014.

[21] Z. Fekete, A. Németh, G. Márton, I. Ulbert, and A. Pongrácz, "Experimental study on the mechanical interaction between silicon neural microprobes and rat dura mater during insertion," *Journal of Materials Science: Materials in Medicine*, vol. 26, no. 2, p. 70, 2015.

[22] P. K. Campbell, K. E. Jones, R. J. Huber, K. W. Horch, and R. a. Normann, "A silicon-based, 3-dimensional neural interface - manufacturing processes for an intracortical electrode array," *IEEE Transactions on Biomedical Engineering*, vol. 38, no. 8, pp. 758–768, 1991.

[23] T. Stieglitz, M. Schuettler, J.-U. Meyer, *et al.*, "Micromachined, polyimide-based devices for flexible neural interfaces," *Biomedical microdevices*, vol. 2, no. 4, pp. 283–294, 2000.

[24] M. F. Zanakis, B. J. Albala, and P. A. Femano, "Method and apparatus for mammalian nerve regeneration," Oct. 4 1988. US Patent 4,774,967.

[25] J. J. FitzGerald, N. Lago, S. Benmerah, J. Serra, C. P. Watling, R. E. Cameron, E. Tarte, S. P. Lacour, S. B. McMahon, and J. W. Fawcett, "A regenerative microchannel neural interface for recording from and stimulating peripheral axons in vivo," *Journal of neural engineering*, vol. 9, no. 1, p. 016010, 2012.

[26] T. Akin, K. Najafi, and R. M. Bradley, "A wireless implantable multichannel digital neural recording system for a micromachined sieve electrode," *IEEE Journal of Solid-State Circuits*, vol. 33, no. 1, pp. 109–118, 1998.

[27] X. Navarro, S. Calvet, F. Rodriguez, T. Stieglitz, C. Blau, M. Buti, E. Valderrama, and J. Meyer, "Stimulation and recording from regenerated peripheral nerves through polyimide sieve electrodes.," *Journal of the peripheral nervous system: JPNS*, vol. 3, no. 2, pp. 91–101, 1998.

[28] F. J. Rodriguez, D. Ceballos, M. Schuttler, A. Valero, E. Valderrama, T. Stieglitz, and X. Navarro, "Polyimide cuff electrodes for peripheral nerve stimulation," *Journal of Neuroscience Methods*, vol. 98, no. 2, pp. 105 – 118, 2000.

[29] K. Horch and G. Dhillon, *Neuroprosthetics : Theory and Practice (Series on Bioengineering and Biomedical Engineering, Vol. 2).* World Scientific, 2004.

[30] K. Krebs, J. Weinberg, and E. Akesson, *Neuroscience.* Lippincott Williams and Wilkins, 2012.

[31] R. Barrett, *Novel Processing Routes for Neural Interfaces.* Ph.d. thesis, School of Electrical, Electronic and Computer Engineering, The University of Birmingham, April 2013.

[32] A. L. Hodgkin and A. F. Huxley, "Propagation of electrical signals along giant nerve fibres," *Proceedings of the Royal Society of London. Series B, Biological Sciences*, vol. 140, no. 899, pp. 177–183, 1952.

[33] A. L. Hodgkin and A. F. Huxley, "The dual effect of membrane potential on sodium conductance in the giant axon of loligo," *The Journal of physiology*, vol. 116, no. 4, pp. 497–506, 1952.

[34] R. B. Stein, D. Charles, L. Davis, J. Jhamandas, A. Mannard, and T. Nichols, "Principles underlying new methods for chronic neural recording," *Canadian Journal of Neurological Sciences*, vol. 2, no. 3, pp. 235–244, 1975.

[35] A. F. Mensinger, D. J. Anderson, C. J. Buchko, M. A. Johnson, D. C. Martin, P. A. Tresco, R. B. Silver, and S. M. Highstein, "Chronic recording of regenerating viiith nerve axons with a sieve electrode," *Journal of Neurophysiology*, vol. 83, no. 1, pp. 611–615, 2000.

[36] R. M. Bradley, R. H. Smoke, T. Akin, and K. Najafi, "Functional regeneration of glossopharyngeal nerve through micromachined sieve electrode arrays," *Brain research*, vol. 594, no. 1, pp. 84–90, 1992.

[37] G. T. Kovacs, C. W. Storment, and J. M. Rosen, "Regeneration microelectrode array for peripheral nerve recording and stimulation," *IEEE Transactions on Biomedical Engineering*, vol. 39, no. 9, pp. 893–902, 1992.

[38] Q. Zhao, J. Drott, T. Laurell, L. Wallman, L. M. Bjursten, G. Lundborg, L. Montelius, N. Danielsen, *et al.*, “Rat sciatic nerve regeneration through a micromachined silicon chip,” *Biomaterials*, vol. 18, no. 1, pp. 75–80, 1997.

[39] D. J. Edell, “A peripheral nerve information transducer for amputees: long-term multichannel recordings from rabbit peripheral nerves,” *IEEE Transactions on Biomedical Engineering*, vol. 33, no. 2, pp. 203–214, 1986.

[40] J. J. FitzGerald, S. P. Lacour, S. B. McMahon, and J. W. Fawcett, “Microchannels as axonal amplifiers,” *IEEE Transactions on Biomedical Engineering*, vol. 55, no. 3, pp. 1136–1146, 2008.

[41] J. J. FitzGerald, S. P. Lacour, S. B. McMahon, and J. W. Fawcett, “Microchannel electrodes for recording and stimulation: in vitro evaluation,” *IEEE Transactions on Biomedical Engineering*, vol. 56, no. 5, pp. 1524–1534, 2009.

[42] S. P. Lacour, J. J. Fitzgerald, N. Lago, E. Tarte, S. McMahon, and J. Fawcett, “Long micro-channel electrode arrays: a novel type of regenerative peripheral nerve interface,” *IEEE transactions on neural systems and rehabilitation engineering*, vol. 17, no. 5, pp. 454–460, 2009.

[43] S. P. Lacour, R. Atta, J. J. FitzGerald, M. Blamire, E. Tarte, and J. Fawcett, “Polyimide micro-channel arrays for peripheral nerve regenerative implants,” *Sensors and Actuators A: Physical*, vol. 147, no. 2, pp. 456–463, 2008.

[44] A. Branner and R. A. Normann, “A multielectrode array for intrafascicular recording and stimulation in sciatic nerve of cats,” *Brain research bulletin*, vol. 51, no. 4, pp. 293–306, 2000.

[45] J. P. Smit, W. L. Rutten, and H. B. Boom, “Endoneural selective stimulating using wire-microelectrode arrays,” *IEEE Transactions on Rehabilitation Engineering*, vol. 7, no. 4, pp. 399–412, 1999.

[46] K. Yoshida, K. Jovanović, and R. B. Stein, “Intrafascicular electrodes for stimulation and recording from mudpuppy spinal roots,” *Journal of neuroscience methods*, vol. 96, no. 1, pp. 47–55, 2000.

[47] C. Watling, N. Lago, S. Benmerah, J. FitzGerald, E. Tarte, S. McMahon, S. Lacour, and R. Cameron, “Novel use of x-ray micro computed tomography to image rat sciatic nerve and integration into scaffold,” *Journal of neuroscience methods*, vol. 188, no. 1, pp. 39–44, 2010.

[48] S. Benmerah, S. P. Lacour, and E. Tarte, “Design and fabrication of neural implant with thick microchannels based on flexible polymeric materials,” in *2009 Annual International Conference of the IEEE Engineering in Medicine and Biology Society*, pp. 6400–6403, Sept 2009.

[49] S. Franssila, *Introduction to Microfabrication (second edition).* John Wiley & Sons, Ltd., 2010.

[50] R. Barrett, S. Benmerah, A. Frommhold, and E. Tarte, “Spiral peripheral nerve interface; updated fabrication process of the regenerative implant,” in *2013 35th Annual International Conference of the IEEE Engineering in Medicine and Biology Society (EMBC)*, pp. 771–774, July 2013.

[51] S. Metz, A. Bertsch, and P. Renaud, “Partial release and detachment of microfabricated metal and polymer structures by anodic metal dissolution,” *Journal of Microelectromechanical Systems*, vol. 14, pp. 383–391, April 2005.

[52] S. F. Cogan, “Neural stimulation and recording electrodes,” *Annu. Rev. Biomed. Eng.*, vol. 10, pp. 275–309, 2008.

[53] R. Emery and G. Povirk, “Tensile behavior of free-standing gold films. part ii. fine-grained films,” *Acta Materialia*, vol. 51, no. 7, pp. 2079 – 2087, 2003.

[54] FujiFilm, “Technical product information durimide 7500,” polyimide datasheet, FujiFilm, October 2015.

[55] H. Huang and F. Spaepen, “Tensile testing of free-standing cu, ag and al thin films and ag/cu multilayers,” *Acta Materialia*, vol. 48, no. 12, pp. 3261 – 3269, 2000.

[56] Z. Suo, E. Y. Ma, H. Gleskova, and S. Wagner, “Mechanics of rollable and foldable film-on-foil electronics,” *Applied Physics Letters*, vol. 74, no. 8, pp. 1177–1179, 1999.

[57] S. Benmerah, *Design and fabrication of novel regenerative implant based on polymeric material.* PhD thesis, School of Electronic, Electrcial and Computer Engineering, 2015.

[58] N. Chou, S. Yoo, and S. Kim, “A largely deformable surface type neural electrode array based on pdms,” *IEEE Transactions on Neural Systems and Rehabilitation Engineering*, vol. 21, pp. 544–553, July 2013.

[59] D. Khodagholy, T. Doublet, M. Gurfinkel, P. Quilichini, E. Ismailova, P. Leleux, T. Herve, S. Sanaur, C. Bernard, and G. G. Malliaras, “Highly conformable conducting polymer electrodes for in vivo recordings,” *Advanced Materials*, vol. 23, no. 36, pp. H268–H272, 2011.

[60] L. Wang and B. Prorok, “The influence of deposition technique on the mechanical properties of freestanding gold films,” tech. rep., Society for Experimental Mechanics, 2007.

[61] C. A. Neugebauer, “Tensile properties of thin, evaporated gold films,” *Journal of Applied Physics*, vol. 31, no. 6, pp. 1096–1101, 1960.

[62] C.-W. Baek, Y.-K. Kim, Y. Ahn, and Y.-H. Kim, “Measurement of the mechanical properties of electroplated gold thin films using micromachined beam structures,” *Sensors and Actuators A: Physical*, vol. 117, no. 1, pp. 17 – 27, 2005.

[63] M. Watanabe, H. Shirai, and T. Hirai, “Wrinkled polypyrrole electrode for electroactive polymer actuators,” *Journal of Applied Physics*, vol. 92, no. 8, pp. 4631–4637, 2002.

[64] A. Romeo, Q. Liu, Z. Suo, and S. P. Lacour, “Elastomeric substrates with embedded stiff platforms for stretchable electronics,” *Applied Physics Letters*, vol. 102, no. 13, p. 131904, 2013.

[65] P. W. Barth, S. L. Bernard, and J. B. Angell, “Flexible circuit and sensor arrays fabricated by monolithic silicon technology,” *IEEE Transactions on Electron Devices*, vol. 32, pp. 1202–1205, Jul 1985.

[66] T. Li, Z. Suo, S. P. Lacour, and S. Wagner, “Compliant thin film patterns of stiff materials as platforms for stretchable electronics,” *Journal of materials research*, vol. 20, no. 12, pp. 3274–3277, 2005.

[67] I. M. Graz, D. P. J. Cotton, A. Robinson, and S. P. Lacour, “Silicone substrate with in situ strain relief for stretchable thin-film transistors,” *Applied Physics Letters*, vol. 98, no. 12, p. 124101, 2011.

[68] L. Jianhui, Y. Bing, W. Xiaoming, R. Tianling, and L. Litian, “Stretchable interconnections for flexible electronic systems,” in *2009 Annual International Conference of the IEEE Engineering in Medicine and Biology Society*, pp. 4124–4127, Sept 2009.

[69] T. Adrega and S. P. Lacour, “Stretchable gold conductors embedded in pdms and patterned by photolithography: fabrication and electromechanical characterization,” *Journal of Micromechanics and Microengineering*, vol. 20, no. 5, p. 055025, 2010.

[70] M. H. Serror, “Analytical study for deformability of laminated sheet metal,” *Journal of Advanced Research*, vol. 4, no. 1, pp. 83 – 92, 2013.

[71] N. Lu, X. Wang, Z. Suo, and J. Vlassak, “Metal films on polymer substrates stretched beyond 50%,” *Applied Physics Letters*, vol. 91, no. 22, p. 221909, 2007.

[72] H. Hocheng and C.-M. Chen, “Design, fabrication and failure analysis of stretchable electrical routings,” *Sensors*, vol. 14, no. 7, pp. 11855–11877, 2014.

[73] T. Yang, X. Li, X. Jiang, S. Lin, J. Lao, J. Shi, Z. Zhen, Z. Li, and H. Zhu, “Structural engineering of gold thin films with channel cracks for ultrasensitive strain sensing,” *Mater. Horiz.*, vol. 3, pp. 248–255, 2016.

[74] H. v. Helmholtz, “Ueber einige gesetze der vertheilung elektrischer ströme in körperlichen leitern mit anwendung auf die thierisch-elektrischen versuche,” *Annalen der Physik*, vol. 165, no. 6, pp. 211–233, 1853.

[75] G. Gouy, “Sur la fonction électrocapillaire,” in *Annales de physique*, vol. 9, pp. 129–184, 1917.

[76] D. L. Chapman, “Li. a contribution to the theory of electrocapillarity,” *The London, Edinburgh, and Dublin philosophical magazine and journal of science*, vol. 25, no. 148, pp. 475–481, 1913.

[77] O. Stern, “The theory of the electrolytic double-layer,” *Z. Elektrochem*, vol. 30, no. 508, pp. 1014–1020, 1924.

[78] D. C. Grahame, “The electrical double layer and the theory of electrocapillarity.,” *Chemical reviews*, vol. 41, no. 3, pp. 441–501, 1947.

[79] G. T. Kovacs, *Enabling Technologies for Cultured Neural Networks*, ch. Seven: Introduction to the Theory, Design, and Modeling of Thin-Film Microelectrodes for Neural Interfaces, pp. 121–165. Academic Press, 1994.

[80] L. Hench, "Biomaterials," *Science*, vol. 208, no. 4446, pp. 826–831, 1980.

[81] L. Hench and J. Wilson, "Surface-active biomaterials," *Science*, vol. 226, no. 4675, pp. 630–636, 1984.

[82] L. L. Hench and J. M. Polak, "Third-generation biomedical materials," *Science*, vol. 295, no. 5557, pp. 1014–1017, 2002.

[83] G. M. Policastro and M. L. Becker, "Osteogenic growth peptide and its use as a bioconjugate in regenerative medicine applications," *Wiley Interdisciplinary Reviews: Nanomedicine and Nanobiotechnology*, vol. 8, no. 3, pp. 449–464, 2015.

[84] E. M. Maynard, C. T. Nordhausen, and R. A. Normann, "The utah intracortical electrode array: a recording structure for potential brain-computer interfaces," *Electroencephalography and clinical neurophysiology*, vol. 102, no. 3, pp. 228–239, 1997.

[85] R. A. Green, N. H. Lovell, G. G. Wallace, and L. A. Poole-Warren, "Conducting polymers for neural interfaces: challenges in developing an effective long-term implant," *Biomaterials*, vol. 29, no. 24, pp. 3393–3399, 2008.

[86] R. Klopfleisch and F. Jung, "The pathology of the foreign body reaction against biomaterials," *Journal of Biomedical Materials Research Part A*, vol. 105, no. 3, pp. 927–940, 2016.

[87] J. Hilborn and L. M. Bjursten, "A new and evolving paradigm for biocompatibility," *Journal of Tissue Engineering and Regenerative Medicine*, vol. 1, no. 2, pp. 110–119, 2007.

[88] J. M. Anderson, A. Rodriguez, and D. T. Chang, "Foreign body reaction to biomaterials," in *Seminars in immunology*, vol. 20, pp. 86–100, Elsevier, 2008.

[89] Y. Choi, S. Park, Y. Chung, R. K. Gore, A. W. English, and R. V. Bellamkonda, "Pdms microchannel scaffolds for neural interfaces with the peripheral nervous system," in *Micro Electro Mechanical Systems (MEMS), 2014 IEEE 27th International Conference on*, pp. 873–876, IEEE, 2014.

[90] M. A. McClain, I. P. Clements, R. H. Shafer, R. V. Bellamkonda, M. C. LaPlaca, and M. G. Allen, "Highly-compliant, microcable neuroelectrodes fabricated from

thin-film gold and pdms," *Biomedical microdevices*, vol. 13, no. 2, pp. 361–373, 2011.

[91] L. Guo, G. S. Guvanasen, X. Liu, C. Tuthill, T. R. Nichols, and S. P. DeWeerth, "A pdms-based integrated stretchable microelectrode array (ismea) for neural and muscular surface interfacing," *IEEE transactions on biomedical circuits and systems*, vol. 7, no. 1, pp. 1–10, 2013.

[92] J. E. Davies, X. Tang, J. W. Denning, S. J. Archibald, and S. J. A. Davies, "Decorin suppresses neurocan, brevican, phosphacan and ng2 expression and promotes axon growth across adult rat spinal cord injuries," *European Journal of Neuroscience*, vol. 19, no. 5, pp. 1226–1242, 2004.

[93] H. G. MOND and K. B. STOKES, "The electrode-tissue interface: The revolutionary role of steroid elution," *Pacing and Clinical Electrophysiology*, vol. 15, no. 1, pp. 95–107, 1992.

[94] H. G. Mond and K. B. Stokes, "The steroid-eluting electrode: A 10-year experience," *Pacing and clinical electrophysiology*, vol. 19, no. 7, pp. 1016–1020, 1996.

[95] H. G. Mond, J. R. Helland, K. Stokes, G. A. Bornzin, and R. McVENES, "The electrode-tissue interface: The revolutionary role of steroid-elution," *Pacing and Clinical Electrophysiology*, vol. 37, no. 9, pp. 1232–1249, 2014.

[96] J. J. FitzGerald, "Suppression of scarring in peripheral nerve implants by drug elution," *Journal of neural engineering*, vol. 13, no. 2, p. 026006, 2016.

[97] Y. Zhong and R. V. Bellamkonda, "Dexamethasone-coated neural probes elicit attenuated inflammatory response and neuronal loss compared to uncoated neural probes," *Brain research*, vol. 1148, pp. 15–27, 2007.

[98] C. H. Thompson, M. J. Zoratti, N. B. Langhals, and E. K. Purcell, "Regenerative electrode interfaces for neural prostheses," *Tissue Eng Part B Rev*, vol. 22, pp. 125–35, April 2016.

[99] V. S. Polikov, P. A. Tresco, and W. M. Reichert, "Response of brain tissue to chronically implanted neural electrodes," *Journal of Neuroscience Methods*, vol. 148, no. 1, pp. 1 – 18, 2005.

[100] A. Srinivasan, M. Tahilramani, J. T. Bentley, R. K. Gore, D. C. Millard, V. J. Mukhatyar, A. Joseph, A. S. Haque, G. B. Stanley, A. W. English, *et al.*, "Microchannel-based regenerative scaffold for chronic peripheral nerve interfacing in amputees," *Biomaterials*, vol. 41, pp. 151–165, 2015.

[101] A. Srinivasan, L. Guo, and R. V. Bellamkonda, "Regenerative microchannel electrode array for peripheral nerve interfacing," in *2011 5th International IEEE/EMBS Conference on Neural Engineering*, pp. 253–256, April 2011.

[102] P. Lotfi, K. Garde, A. K. Chouhan, E. Bengali, and M. I. Romero-Ortega, "Modality-specific axonal regeneration: toward selective regenerative neural interfaces," *Frontiers in neuroengineering*, vol. 4, no. 11, p. 0, 2011.

[103] I. I. Stoyanova, R. J. A. van Wezel, and W. L. C. Rutten, "In vivo testing of a 3d bifurcating microchannel scaffold inducing separation of regenerating axon bundles in peripheral nerves," *Journal of Neural Engineering*, vol. 10, no. 6, p. 066018, 2013.

[104] R. A. Green, N. H. Lovell, and L. A. Poole-Warren, "Impact of co-incorporating laminin peptide dopants and neurotrophic growth factors on conducting polymer properties," *Acta biomaterialia*, vol. 6, no. 1, pp. 63–71, 2010.

[105] R. T. Richardson, B. Thompson, S. Moulton, C. Newbold, M. G. Lum, A. Cameron, G. Wallace, R. Kapsa, G. Clark, and S. OLeary, "The effect of polypyrrole with incorporated neurotrophin-3 on the promotion of neurite outgrowth from auditory neurons," *Biomaterials*, vol. 28, no. 3, pp. 513 – 523, 2007.

[106] I. Vujaklija, S. Muceli, K. Bergmeister, O. C. Aszmann, and D. Farina, "Prospects of neurorehabilitation technologies based on robust decoding of the neural drive to muscles following targeted muscle reinnervation," in *Converging Clinical and Engineering Research on Neurorehabilitation II*, pp. 1359–1363, Springer, 2017.

[107] V. W. Wong and R. J. Redett, "Targeted reinnervation strategies to restore upper limb function," in *Rehabilitative Surgery*, pp. 281–288, Springer, 2017.

[108] P. A. Herman, G. Prasad, and T. M. McGinnity, "Designing an interval type-2 fuzzy logic system for handling uncertainty effects in brain–computer interface classification of motor imagery induced eeg patterns," *IEEE Transactions on Fuzzy Systems*, vol. 25, no. 1, pp. 29–42, 2017.

[109] C. McCrimmon, J. Fu, M. Wang, L. L. Silva, P. Wang, A. Karimi-Bidhendi, C. Liu, P. Heydari, Z. Nenadic, and A. Do, "A portable brain-computer interface platform

for eeg acquisition and decoding.," *IEEE Transactions on Biomedical Engineering*, vol. 64, no. 10, pp. 2313–2320, 2017.

[110] Y. Abdelrahman, M. Hassib, M. G. Marquez, M. Funk, and A. Schmidt, "Implicit engagement detection for interactive museums using brain-computer interfaces," in *Proceedings of the 17th International Conference on Human-Computer Interaction with Mobile Devices and Services Adjunct*, pp. 838–845, ACM, 2015.

[111] H. Huang, P. Zhou, G. Li, and T. A. Kuiken, "An analysis of emg electrode configuration for targeted muscle reinnervation based neural machine interface," *IEEE Transactions on Neural Systems and Rehabilitation Engineering*, vol. 16, no. 1, pp. 37–45, 2008.

[112] K. A. Ludwig, J. D. Uram, J. Yang, D. C. Martin, and D. R. Kipke, "Chronic neural recordings using silicon microelectrode arrays electrochemically deposited with a poly (3, 4-ethylenedioxythiophene)(pedot) film," *Journal of neural engineering*, vol. 3, no. 1, p. 59, 2006.

[113] M. R. Abidian, J. M. Corey, D. R. Kipke, and D. C. Martin, "Conducting-polymer nanotubes improve electrical properties, mechanical adhesion, neural attachment, and neurite outgrowth of neural electrodes," *small*, vol. 6, no. 3, pp. 421–429, 2010.

[114] E. W. Keefer, B. R. Botterman, M. I. Romero, A. F. Rossi, and G. W. Gross, "Carbon nanotube coating improves neuronal recordings," *Nature nanotechnology*, vol. 3, no. 7, pp. 434–439, 2008.

[115] N. B. Langhals, M. G. Urbanchek, A. Ray, and M. J. Brenner, "Update in facial nerve paralysis: Tissue engineering and new technologies," *Current opinion in otolaryngology & head and neck surgery*, vol. 22, pp. 291–299, Aug. 2014.

[116] T. Stieglitz, H. Ruf, M. Gross, M. Schuettler, and J. Meyer, "A biohybrid system to interface peripheral nerves after traumatic lesions: design of a high channel sieve electrode," *Biosensors and Bioelectronics*, vol. 17, no. 8, pp. 685 – 696, 2002.

[117] B. Ji, M. Wang, X. Kang, X. Gu, C. Li, B. Yang, X. Wang, and J. Liu, "Flexible optoelectric neural interface integrated wire-bonding μ leds and microelectrocorticography for optogenetics," *IEEE Transactions on Electron Devices*, vol. 64, pp. 2008–2015, May 2017.

[118] S. B. Goncalves, J. F. Ribeiro, A. F. Silva, R. M. Costa, and J. H. Correia, "Design and manufacturing challenges of optogenetic neural interfaces: a review," *Journal of Neural Engineering*, vol. 14, no. 4, p. 041001, 2017.

[119] W. A. Lee, "Hand transplantation: Evolution of a personal outlook," *The Journal of Hand Surgery*, vol. 42, no. 4, pp. 286–290, 2017.

[120] J. T. Shores, V. Malek, W. A. Lee, and G. Brandacher, "Outcomes after hand and upper extremity transplantation," *Journal of Materials Science: Materials in Medicine*, vol. 28, no. 5, p. 72, 2017.

[121] V. Gupta, M. Sengupta, J. Prakash, and B. C. Tripathy, "Tissue engineering and artificial organ," in *Basic and Applied Aspects of Biotechnology*, pp. 453–474, Springer, 2017.

[122] J. Bloch, S. P. Lacour, and G. Courtine, "Electronic dura mater meddling in the central nervous system," *Jama neurology*, vol. 74, no. 4, pp. 470–475, 2017.

[123] N. Vachicouras, C. M. Tringides, P. B. Campiche, and S. P. Lacour, "Engineering reversible elasticity in ductile and brittle thin films supported by a plastic foil," *Extreme Mechanics Letters*, vol. 15, no. Supplement C, pp. 63–69, 2017.

[124] M. Esmaeili, M. Berry, A. Logan, and Z. Ahmed, "Decorin treatment of spinal cord injury," *Neural Regeneration Research*, vol. 9, pp. 1653–1656, Aug. 2014.

[125] P. Li and R. Bashirullah, "A wireless power interface for rechargeable battery operated medical implants," *IEEE Transactions on Circuits and Systems II: Express Briefs*, vol. 54, no. 10, pp. 912–916, 2007.

[126] K. D. Wise, D. J. Anderson, J. F. Hetke, D. R. Kipke, and K. Najafi, "Wireless implantable microsystems: High-density electronic interfaces to the nervous system," in *Proceedings of the IEEE*, 2004.